

**STUDIES ON THE MECHANICAL PROPERTIES AND
CORROSION BEHAVIOUR OF $\text{Al}_{20}\text{Be}_{20}\text{Fe}_{10}\text{Si}_{15}\text{Ti}_{35}$ HIGH
ENTROPY ALLOY PRODUCED BY MECHANICAL
ALLOYING AND SPS SINTERING**

A dissertation submitted in fulfilment of the requirements for the
degree

Master of Engineering in Metallurgical Engineering

In the

Faculty of Engineering and Technology

By

Omoyemi Temitope, ONAWALE

218249233



**VAAL UNIVERSITY
OF TECHNOLOGY**

Inspiring thought. Shaping talent.

Vaal University of Technology

Private Bag X021, Vanderbijlpark 1900, South Africa.

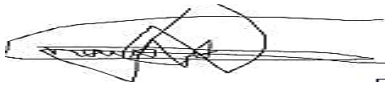
Supervisor: Prof. Wallace Matizamhuka

Co-Supervisor: Prof. Ronald Machaka

Date: 22nd February 2022

DECLARATION

I **Omoyemi Temitope, Onawale** hereby declare that I am the sole author of this dissertation. The content of this dissertation was compiled by me and with the help and support from respected parties mentioned in the acknowledgement. It is submitted for the degree of Masters in Engineering: Metallurgical, to the Department of Chemical and Metallurgical Engineering at the Vaal University of Technology, Vanderbijlpark, South Africa. I declare that no plagiarism was committed in this dissertation or that any part of it or whole submitted in candidature for any degree elsewhere.



Signed (Omoyemi Temitope Onawale)

22nd February 2022

Date

ACKNOWLEDGEMENTS

Firstly, I would like to thank Almighty God for the gift of life and opportunities granted to me.

I would also like to extend my appreciation to the following individuals whom have directly or indirectly contributed academically, socially, morally or financially from the beginning of the research till the completion of this dissertation:

1. Special thanks go to my supervisor Prof. Wallace Matizamhuka and his family for their guidance and support towards successful completion of this research. Their innovative ideas and enthusiasm in research went a long way in encouraging and inspiring me towards the success of my research. I would also like to thank my co-supervisor Prof. Ronald Machaka for his tireless effort and constructive innovation in ensuring the success of this research.
2. My sincere gratitude also goes to VUT laboratory technologists and staff members in the department of Chemical and Metallurgical Engineering and most especially the school administrator; Mrs Retha for her consistent hard work towards order purchases. I will also like to thank TUT Metallurgy Laboratory Technologist Mr Busang and UJ Laboratory Technologist Mr Phadisa Pole and Mr Stephen Wagenaar for assisting in running some experiments in their laboratories.
3. My gratitude is not complete without acknowledging the effort of my colleagues Prince Cobbinah, Rivel Nzeukou and Sibongile Dlamini who always support with their advice towards my research.
4. I am very grateful to my family members; my father (Mr Onawale W.O), my mother; (Mrs Onawale E.I) and my siblings; (Omowumi, Omolola and Abosede with their respective family) for their diligent support they provided throughout my academic journey.
5. Am delighted to thank Titanium Centre of Competence (TiCoC) for providing financial support and Vaal University of Technology (VUT) for granting me the opportunity.

DEDICATION

This thesis dissertation is dedicated to Almighty God, the maker of Heaven and Earth and everything in it, for making all my accomplishment so far possible.

LIST OF PUBLICATION IN ACCREDITED JOURNAL FROM THIS WORK

1. ONAWALE, O. T., COBBINAH, P. V., NZEUKOU, R. A. & MATIZAMHUKA, W. R. 2021. Synthesis Route, Microstructural Evolution, and Mechanical Property Relationship of High-Entropy Alloys (HEAs): A Review. *Materials*, 14, 3065.

ABSTRACT

To meet structural, biomedical, and energy-saving application requirements, weight reduction is of utmost concern especially in the transportation sector because it is the feasible means of reducing fuel consumption as well as greenhouse gas emissions. The fabrication of light weight high entropy alloys (LWHEAs) using traditional design methods such as the addition of refractory elements or casting has proven that it is almost impossible to achieve the required properties in LWHEA. The spark plasma sintering (SPS) method was employed to consolidate wet and dry mechanically alloyed (MA) $\text{Al}_{20}\text{Be}_{20}\text{Fe}_{10}\text{Si}_{15}\text{Ti}_{35}$. This is owing to the possibility of achieving desired mechanical properties and produce high-performance bulk HEAs with homogeneous and finer grains during the processing route, unlike the conventional casting techniques. The EDS, SEM and XRD examination that was conducted on both wet and dry milled alloy powders reveals a decomposition condition took place at temperatures of approx.. 200°C . We suspect that this is associated with a low melting $\text{Fe}_2\text{Be}_{17}$ phase, which becomes unstable with increase in temperature. This is in conformity with literature that highlights that the influence of Al and Fe on the performance of Be will depend upon which phases manifest. It has been established that volatility properties of ethanol and Fe must have aided sublimation tendency of wet milled alloy mix especially. This is in addition to evaporation tendency of Be powder. A thermo-analytical process was also conducted on both dry-milled and wet-milled alloy powder. This confirmed a decomposition leading to thermal expansion in both dry and wet milled alloy powder at a rapid rate from room temperature to $\sim 150^{\circ}\text{C}$. Hence, $\text{Al}_{20}\text{Be}_{20}\text{Fe}_{10}\text{Si}_{15}\text{Ti}_{35}$ milled powder is thermally unstable being the possible cause of premature sublimation that occurred during the sintering process.

TABLE OF CONTENTS

Declaration	ii
Acknowledgements	iii
Dedication	iv
List of publication in accredited journal from this work	v
Abstract	vi
Table of Contents	vii
List of Figures	viii
List of Tables	xi
Symbols and Abbreviations	xii
1.0 INTRODUCTION.....	14
1.1 BACKGROUND INFORMATION.....	14
1.2 MOTIVATION.....	16
1.3 PROBLEM STATEMENT	17
1.4 HYPOTHESIS.....	17
1.5 AIM AND OBJECTIVE:.....	18
1.5.1 SPECIFIC OBJECTIVES	18
1.6 SCOPE OF THE STUDY	18
2.0 LITERATURE REVIEW	19
2.1 BACKGROUND:.....	19
2.2 MECHANICAL ALLOYING TECHNIQUE	19
2.3 MECHANISMS OF SINTERING.....	20
2.3.1 Spark Plasma Sintering (SPS).....	22
2.4 INCEPTION OF HIGH ENTROPY ALLOYS (HEAs)	23
2.5 PROPERTIES OF HIGH ENTROPY ALLOYS (HEAs)	24
2.5.1 High Entropy Effect.....	24
2.5.2 Sluggish Diffusion Effect	26
2.5.3 Lattice Distortion Effect	27
2.5.4 Cocktail Effect.....	28
2.6 SYNTHESIS OF HIGH ENTROPY ALLOYS (HEAs)	30
2.6.1 Melting and Casting Route.....	30
2.6.2 Powder Metallurgy Route.....	31
2.7 SYNTHESIS OF LIGHT-WEIGHT HIGH ENTROPY ALLOYS (LWHEAs)	33
2.8 $Al_{20}Be_{20}Fe_{10}Si_{15}Ti_{35}$, ELEMENTAL COMPOSITION AND ENTROPY ALLOY CLASSIFICATION....	34

2.9	THERMAL ANALYSIS AND STABILITY	40
2.10	DIFFERENTIAL SCANNING CALORIMETRY (DSC)	42
3.0	RESEARCH METHODOLOGY.....	46
3.1	RESEARCH APPROACHES	46
3.2	EXPERIMENTAL PROCEDURE	46
3.2.1	CHARACTERIZATION OF AS-RECEIVED POWDERS.....	46
3.2.2	MILLING OF $Al_{20}Be_{20}Fe_{10}Si_{15}Ti_{35}$ IN WET AND DRY CONDITIONS.....	49
3.2.3	SINTERING OF WET-MILLED AND DRY-MILLED $Al_{20}Be_{20}Fe_{10}Si_{15}Ti_{35}$ ALLOY	54
3.2.4	TGA/DSC ANALYSIS OF DRY AND WET-MILLED $Al_{20}Be_{20}Fe_{10}Si_{15}Ti_{35}$ ALLOY POWDERS .	56
4.0	RESULTS AND DISCUSSION.....	58
4.1	Al, Be, Fe, Si & Ti As-received Particle Size Analysis (PSD) Results	58
4.2	Al, Be, Fe, Si and Ti As-received SEM Micrographs.....	61
4.3	XRD Images of Individual As-received Element	63
4.4	Milled $Al_{20}Be_{20}Fe_{10}Si_{15}Ti_{35}$ Alloy Powder.....	66
4.4.1	SEM Micrographs of Dry-milled $Al_{20}Be_{20}Fe_{10}Si_{15}Ti_{35}$ Alloy Powder.....	66
4.4.2	SEM Micrographs of Wet-milled $Al_{20}Be_{20}Fe_{10}Si_{15}Ti_{35}$ Alloy Powder.....	69
4.5	XRD of Milled $Al_{20}Be_{20}Fe_{10}Si_{15}Ti_{35}$ Alloy Powder.....	72
4.6	Sintering of $Al_{20}Be_{20}Fe_{10}Si_{15}Ti_{35}$ Alloy powder	75
4.6.1	Sintering of Wet-milled $Al_{20}Be_{20}Fe_{10}Si_{15}Ti_{35}$ Alloy powder	75
4.6.2	Sintering of Dry-milled $Al_{20}Be_{20}Fe_{10}Si_{15}Ti_{35}$ Alloy powder	76
4.7	Thermogravimetric Analysis and Differential Scanning Calorimetric (TGA/DSC) of $Al_{20}Be_{20}Fe_{10}Si_{15}Ti_{35}$ Alloy Powder	78
5.0	CONCLUSION AND RECOMMENDATIONS.....	81
5.1	CONCLUSION	81
5.2	RECOMMENDATIONS.....	82
6.0	LIMITATION	83
	Reference.....	84

LIST OF FIGURES

Figure 2.1	Schematic diagram showing the movement of charge during mechanical alloying	20
Figure 2.2	Schematic diagram of SPS process	23
Figure 2.3	Schematic diagram of the (ΔH_{mix}) against (δ) showing solid solutions, intermetallic compounds, and amorphous phases	25
Figure 2.4	Examples of (a) BCC and (b) FCC crystal structures having five principal elements.	28
Figure 2.5	Hardness effect of aluminum addition on the cast CuCoNiCrAl _x Fe alloys. A B and C refer to the hardness while FCC and BCC are lattice constant	30
Figure 2.6	Schematic diagram of the Bridgman solidification process	31
Figure 2.7	Schematic diagram of a typical TG system	41
Figure 2.8	Schematic diagram of a DSC system	43
Figure 2.9	Shows a typical DSC thermogram	44
Figure 3.1	Shows Malvern particle size analyser equipment	46
Figure 3.2	JEOL JSM-IT500 scanning electron microscopy (SEM) machine equipped with EDS	47
Figure 3.3	Shows X-ray diffraction machine PANalytical	48
Figure 3.4	Shows a schematic representation of the milling machine used for the milling process	49
Figure 3.5	Shows the drying process of wet-milled alloy in the rotary vapor drying machine.	52
Figure 3.6	Shows the FCT Systeme GmbH sintering machine used	53
Figure 3.7	Shows TGA/DSC equipment set up (A) STA7200RV TGA/DSC and (B) auto-sampler	56
Figure 4.1	Graph showing the average particle size distribution of Al powder	57
Figure 4.2	Graph showing the average particle size distribution of Be powder	57
Figure 4.3	Graph showing the average particle size distribution of Fe powder	58
Figure 4.4	Graph showing the average particle size distribution of Si powder	58
Figure 4.5	Graph showing the average particle size distribution of Ti powder	59
Figure 4.6	SEM of as-received Al powder (A) x500 and (B) x1000	60
Figure 4.7	SEM of as-received Be powder (C) x100 and (D) x150	60
Figure 4.8	SEM of as-received Fe powder (E) x1500 and (F) x4000	61
Figure 4.9	SEM of as-received Si powder (G) x800 and (H) x1000	62
Figure 4.10	SEM of as-received Ti powder (I) x350 and (J) x500	63
Figure 4.11	Shows XRD of as-received Al powder	62

LIST OF FIGURES CONTINUES

Figure 4.12	Shows XRD of as-received Fe powder	63
Figure 4.13	Shows XRD of as-received Be powder	63
Figure 4.14	Shows XRD of as-received Si powder	64
Figure 4.15	Shows XRD of as-received Ti powder	64
Figure 4.16	Shows the SEM image of dry-milled alloy powder (14hrs) (A) x200 and (B) x900	65
Figure 4.17	Shows the EDS image analysis of the dry-milled alloy powder	65
Figure 4.18	Shows the EDS mapping of the individual element in a dry-milled alloy sample	67
Figure 4.19	Shows the SEM image of wet-milled alloy powder (24hrs) (C) x550 and (D) x900	68
Figure 4.20	Shows the EDS image analysis of the wet-milled alloy powder	68
Figure 4.21	Shows the EDS mapping of the individual element in a wet-milled alloy sample	70
Figure 4.22	Shows XRD of dry-milled alloy powder	71
Figure 4.23	Shows XRD of wet-milled alloy powder	72
Figure 4.24	Change in formation enthalpy with increasing Fe content.	73
Figure 4.25	Depicts wet-milled alloy powder sublimating out of the punch and die during the sintering process	74
Figure 4.26	(A) Depicts the compacted dry-milled $Al_{20}Be_{20}Fe_{10}Si_{15}Ti_{35}$ alloy powder heated up to 250°C, (B) escaped alloy powder from the punch and die during compaction.	75
Figure 4.27	Free energy formation vs temperature for Fe-Be binary intermetallic (Values are normalized per Fe atom.)	76
Figure 4.28	Shows dry-milled alloy (A) TG curve and (B) DSC curve	77
Figure 4.29	Shows wet-milled alloy (C) TG curve and (D) DSC curve	78

LIST OF TABLES

Table 2.1	Different Sintering Mechanisms	21
Table 2.2	HEAs processed via different processing methods, strengthening mechanism used, and the effect on mechanical properties	37
Table 3.1	Shows the summary of the calculation of the volume for each sample to be sintered	49
Table 3.2	Shows a summary in part, of the variables to be considered in calculating the total mass to be weighed	50
Table 3.3	Shows the summary of the rest of the variables to be considered in calculating the total mass to be weighed	51
Table 3.4	shows the conditions and parameters used for the milling process	52
Table 3.5	Shows the summary of the variables needed to calculate the temperature at which sintering of the alloy powder will be carried out.	54
Table 3.6	Shows the parameters used to sinter wet-milled alloy	54
Table 3.7	Shows the parameters used to sinter dry-milled alloy	55
Table 3.8	Shows the parameters used for the TGA/DSC thermal analysis (dry and wet)	56
Table 4.1	Shows starting particle size detail of elemental powders (PSD)	59
Table 4.2	Shows the percentage by mass and atom of the individual component element in the dry-milled alloy powder	66
Table 4.3	Shows the percentage by mass and atom of the individual component element in the wet-milled alloy powder.	69

SYMBOLS AND ABBREVIATIONS

Symbols

K	-- Boltzman's Constant(J/K)
N	-- Element
S	-- Configuration Entropy(J/K)
R	-- Universal Gas Constant(J/K/mol)
c_i	-- Molar content(mol/dm ³)
δ	-- Atomic size(A)
q	-- Heat(J)
t	-- Time(s)
ΔT	-- Change in temperature(K or °C)
C_p	-- Heat Capacity(J/K)
ΔG_{mix}	-- Gibbs free energy of mixing(kJ/mol)
ΔH_{mix}	-- Enthalpy of mixing(kJ/mol)
ΔS_{mix}	-- Entropy of mixing(kJ/K/mol)
ϖ_T	-- Theoretical Mass(g or mol)
ρ_T	-- Theoretical Density(g/cm ³)

Abbreviations

HEAs	-- High Entropy Alloys
LEA	-- Low Entropy Alloy
MEA	-- Medium Entropy Alloy
LWHEAs	-- Light-Weight High Entropy Alloys
MPEAs	-- Multi-Principal Element Alloys
RHEAs	-- Refractory High Entropy Alloys
CCAs	-- Complex Concentrated Alloys
HESAs	-- High Entropy Superalloys
FCC	-- Face-Centered Cubic
BCC	-- Body-Centered Cubic
PM	-- Powder Metallurgy
MA	-- Mechanical Alloy
SPS	-- Spark Plasma Sintering
PCA	-- Process Control Agent

HP	-- Hot Pressing
LM	-- Levitation Melting
AM	-- Arc Melting
ID	-- Inter-Dendritic
PECS	-- Pulsed Electric Current Sintering
LPE	-- Lattice Potential Energy
FAST	-- Fast-assisted Sintering Technology
DC	-- Direct Current
PSD	-- Particle Size Distribution
TiCoC	-- Titanium Centre of Competence
CSIR	-- Centre for Science Institute and Research
SEM	-- Scanning Electron Microscopy
EDS	-- Energy Dispersive X-Ray Spectroscopy
TEM	-- Transmission Electron Microscopy
XRD	-- X-ray Diffraction Microscopy
ADPs	-- Atomic Displacement Parameters
CALPHAD	-- CALculation of Phase Diagrams
TGA	-- Thermogravimetric Analysis
DSC	-- Differential Scanning Calorimetry
w/w	-- Weight per Weight

1.0 INTRODUCTION

1.1 BACKGROUND INFORMATION

There is a constant demand for lightweight materials with improved mechanical properties such as high yield strength, good ductility, good fracture toughness, very good corrosion-resistance, work hardening capacity and at times creep and wear resistance (Li et al., 2019b). Over the past three decades, researchers have continuously made efforts to replace high-density metals and alloys such as steel with aluminum, silicon, titanium, and composite-based materials without compromising on structural properties and avoiding a significant increase in cost. To meet structural, transportation, biomedical, and energy-saving application requirements, weight reduction is of utmost concern especially in the transportation sector because it is the feasible means of reducing fuel consumption as well as greenhouse gas emissions (Kumar and Gupta, 2016).

According to W Cheah (2010), there will be a reduction of approximately 20kg in carbon dioxide emission for every kilogram of weight reduced in a vehicle, this is possible because, for every 10% reduction in total weight of a vehicle, the vehicle will save 7% of its fuel consumption. Development of multicomponent alloys dates as far back as 2004 when two research groups, Prof. B. Cantor of Oxford University and Prof. J.-W. Yeh of National Tsing Hua University began to expand at a rapid rate (MacDonald et al., 2017). Generally, it has been discovered that there will be the formation of simple solid solution phases rather than intermetallic compounds when about five or more principal elements with each concentration ranging from 5% to 35% are mixed in either nominally equiatomic ratio, non-equiatomic, or near-equimolar ratio according to Yeh et al. (2004b). Although, some of them do possess small amounts of intermetallic compounds in addition to a large amount of stable solid solution phases. This stability was owing to significantly the large configuration or high mixing entropy possibility (Kumar and Gupta, 2016) in comparison to traditional alloys in the liquid state or random solid solution state. This class of materials is termed High Entropy Alloys (HEAs).

In general, HEAs which are sometimes called multi-component alloys to encompass a broad class of metallic and ceramic materials. Some research has shown that either amorphous phases or intermetallic compounds or both might form sometimes in the crystal structure besides solid-solution phases in multi-component HEAs (Zheng et al.,

2019), (Gwalani et al., 2018). Hence, in most cases, HEAs have been discovered to form simple solid solutions of face-centered cubic (FCC) and/or body-centered cubic (BCC). Having enthalpy of mixing between -22 & 7 kJ/mol and very small differences in atomic radius, good thermal stability, easily form nano-sized precipitates, high fracture toughness (Gludovatz et al., 2014), excellent corrosion resistance, good fatigue (Tang et al., 2015), work hardening capacity and have a hardness ranging from 100 to 1100 Hv, density of $\sim 3.91\text{gcm}^{-3}$. However, the four major core effects associated with HEAs are sluggish diffusion, high entropy, cocktail effects, and severe lattice distortion (Yeh, 2006b).

Recently, light-weight HEAs (LWHEAs) have gained more attention, especially for structural applications. Apparently, due to Ti and its alloys properties such as low density ($\sim 4.43\text{ g cm}^{-3}$), excellent corrosion resistance in seawater and acidic environment, good high-temperature strength and creep resistance up to 325°C . The alloy Ti-6Al-4V has been well utilized in the submarine, chemical industries, aviation, and biomedical devices. However, Ti and its alloys cannot be utilized where resistance to wear, creep and oxidation is required at high temperatures. Hence, alloys with a lower density, high hardness, high oxidation resistance, resistance to fracture toughness, and corrosion resistance will be more suitable for structural applications where Ti-based alloys have failed.

Tseng et al. (2018) synthesized $\text{Al}_{20}\text{Be}_{20}\text{Fe}_{10}\text{Si}_{15}\text{Ti}_{35}$ alloy through the casting method and discovered that the as-cast microstructure is composed of one major phase and two minor phases. It has been discovered and proven that it is almost impossible to achieve the required properties in LWHEA alloys through the traditional design methods such as the addition of refractory elements or casting (Kumar and Gupta, 2016). However, the addition of Ti carrying the largest atomic size will improve the alloys' mechanical and anti-corrosion properties (Han et al., 2017) while the addition of Al and Si will provide oxidation resistance and reduce the density of the alloy. Beryllium alloys are widely used for light-weight structural components in aerospace and defence industries, its alloys is also used for food packaging. Beryllium will also reduce density while the inclusion of Si & Fe is expected to improve solid solution strengthening. The spark plasma sintering (SPS) method will be employed to consolidate mechanically alloyed (MA) HEA powders to fabricate $\text{Al}_{20}\text{Be}_{20}\text{Fe}_{10}\text{Si}_{15}\text{Ti}_{35}$ alloy. Owing to the possibility of achieving desired mechanical properties and producing high-performance bulk HEAs (Fu et al., 2013) with homogeneous and finer

grains during the processing route, unlike the conventional casting techniques. The powder metallurgy processing route is chosen to fabricate this alloy because of the possibility of achieving better quality and homogeneous samples as recorded in the literature (Kang et al., 2018). This will ensure less bias in the measured mechanical and corrosion properties which may be caused by inhomogeneity as in the case of cast samples. Therefore, much work is required to successfully synthesize lightweight HEAs ($\text{Al}_{20}\text{Be}_{20}\text{Fe}_{10}\text{Si}_{15}\text{Ti}_{35}$) with stable microstructure and properties as per variable application conditions. This can be done by proper alloy designing and carefully selecting the processing routes/parameters for the synthesis of $\text{Al}_{20}\text{Be}_{20}\text{Fe}_{10}\text{Si}_{15}\text{Ti}_{35}$ alloy.

1.2 MOTIVATION

Reports have proven that climate change will be irreversible if the temperature rises by a margin of 2°C beyond that of pre-industrial times which is pointing to the degree of damage done by global warming to our ecosystem. Apart from the burning of fossil fuels that release greenhouse gases such as carbon dioxide by the energy sector, the transportation sector has largely contributed to a major cause of global warming due to greenhouse gases emitted by automobiles. Research shows that one of the effective methods to reduce and arrest emissions is to reduce the weight of automobiles. There is a need to replace high-density automobile part materials with lightweight materials and this calls for designing an ideal cost-effective processing route to synthesize light weight alloys such as, $\text{Al}_{20}\text{Be}_{20}\text{Fe}_{10}\text{Si}_{15}\text{Ti}_{35}$ a potential LWHEA for such applications as well as for food packaging purposes.

$\text{Al}_{20}\text{Be}_{20}\text{Fe}_{10}\text{Si}_{15}\text{Ti}_{35}$ is a titanium-based LWHEA, perhaps Ti is known for its fascinating mechanical properties such as strength to density ratio and corrosion resistance. South Africa currently has the fourth-largest titanium mineral reserves in the world and the second-largest producer of titanium mineral concentrate across the globe. Perhaps, little or no value is added to this mineral before exporting it because South Africa still lacks the capacity to add value to titanium and its alloys into finished products.

This has led to the establishment of the Titanium Centre of Competence (TiCoC), under CSIR which is funded by the Department of Science and Innovation in South Africa. This research aims to increase the knowledge base of titanium-based alloy

focusing on various methods of processing Ti-based LWHEA to make this alloy viable economically and save our ecosystem. This will lead to the establishment and sustainability of a viable value chain for Ti processing in the near future.

1.3 PROBLEM STATEMENT

There has been an increase in demand for lightweight HEAs in the aerospace industry and ever since the transportation sector has been found as a major cause of global warming due to the emission of carbon dioxide from automobiles and greenhouse gas. Still, there are major complications in designing lightweight HEAs such as $\text{Al}_{20}\text{Be}_{20}\text{Fe}_{10}\text{Si}_{15}\text{Ti}_{35}$, to meet relatively high temperature structural and transportation requirements, especially when exposed to corrosive environments.

This is owing to lower density, poor corrosion, low melting point, lower strength, and lower hardness nature of some elemental components of the alloy. Apparently, most of these elements are immiscible with transition group elements due to varying atomic radii and high positive enthalpy that mostly result in the formation of intermetallic phases rather than a solid solution. However, achieving desired mechanical and corrosion-resistant properties in a material depends on carefully selecting the processing routes/parameters for the synthesis of the alloy. $\text{Al}_{20}\text{Be}_{20}\text{Fe}_{10}\text{Si}_{15}\text{Ti}_{35}$ HEA will be synthesized through MA and SPS while its mechanical and corrosion properties will be examined for transportation and energy-saving applications.

1.4 HYPOTHESIS

It is hypothesized that:

- synthesizing $\text{Al}_{20}\text{Be}_{20}\text{Fe}_{10}\text{Si}_{15}\text{Ti}_{35}$ HEA through powder metallurgy route (MA + SPS) will result in desired mechanical and corrosion properties suitable for transportation and energy-saving applications.
- carefully examine the microstructure, phase changes and thermal stability, will give clear understanding on challenges associated with synthesizing $\text{Al}_{20}\text{Be}_{20}\text{Fe}_{10}\text{Si}_{15}\text{Ti}_{35}$ LWHEAs alloy using MA and SPS.

1.5 AIM AND OBJECTIVE:

Aim: The aim of this work is to synthesize $\text{Al}_{20}\text{Be}_{20}\text{Fe}_{10}\text{Si}_{15}\text{Ti}_{35}$ LWHEA through powder metallurgy route (MA + SPS) and investigate its mechanical and corrosion behavior for transportation and energy-saving applications.

1.5.1 SPECIFIC OBJECTIVES

The specific objectives of the study are to:

1. To mechanically mill the alloy mixed powders using ball milling machine according to stated parameters;
2. To optimize the sintering parameters required to obtain a fully sintered alloy for further characterization;
3. To carefully examine the microstructure, phase changes, thermal stability, hardness, and corrosion behavior (exposed to different environments) of the resultant LWHEA;

1.6 SCOPE OF THE STUDY

This study focuses on synthesizing $\text{Al}_{20}\text{Be}_{20}\text{Fe}_{10}\text{Si}_{15}\text{Ti}_{35}$ LWHEA using powder metallurgy processing route (MA + SPS) and will investigate its mechanical properties as well as how the synthesized alloy will behave when subjected to different corrosive environments mainly for transportation and energy-saving applications.

2.0 LITERATURE REVIEW

2.1 BACKGROUND:

Previous research has shown that obtaining dense bulk materials is a necessity to achieve desired properties in some engineering applications such as structural, and energy sectors. One of the possible and easy procedures to follow in achieving this is through powder metallurgy (PM) fabrication approach, specifically, mechanical alloying (MA) of pure elemental powders and subsequent powder densification by spark plasma sintering (SPS) (Moravcik et al., 2017). The advantages of using this processing technique include but are not limited to ease of advanced composite preparation (Moravcik et al., 2016), generation of nano-grained materials (Chen et al., 2013), and avoidance of segregation issue. Although, the properties of PM synthesized HEA bulk materials may be less ductile but it is not an overstatement to conclude that limitations encountered in casting routes can be overcome.

2.2 MECHANICAL ALLOYING TECHNIQUE

Mechanical alloying (MA) was developed by John Benjamin and his colleagues in 1966 at the International Nickel Company (INCO). S. Benjamin and E. Volin (1974) define it as a solid-state process that allows dispersion of insoluble phases and the addition of reactive alloying elements to produce composite metal powders with controlled microstructures. In this process, a high-energy stirred ball mill or shaker mill is used to subject blended powders of known particle size to a compressive force to agglomerate the powders. S. Benjamin and E. Volin (1974) divided the mechanical alloying process into five different stages namely: The initial stage, the period of welding, the equiaxed particle formation period, the start of random welding orientation, and steady-state processing. Hence, these periods can be explained in terms of a) distribution of the powder and shape, b) how hard the material is on ball surface, c) microstructure of the powder and material on ball surface, d) material division between ball surfaces and free powders.

Research conducted by S. Benjamin and E. Volin (1974) shows that composite particles are formed and refinement of structure occurs as a result of welding and fracturing of free powder particles. They further reported that the mechanical energy input as well as rate of work hardening of the material will influence the rate of structural refinement. However, formation of homogenous composite particles is mostly a logarithmic function of time and powder properties.

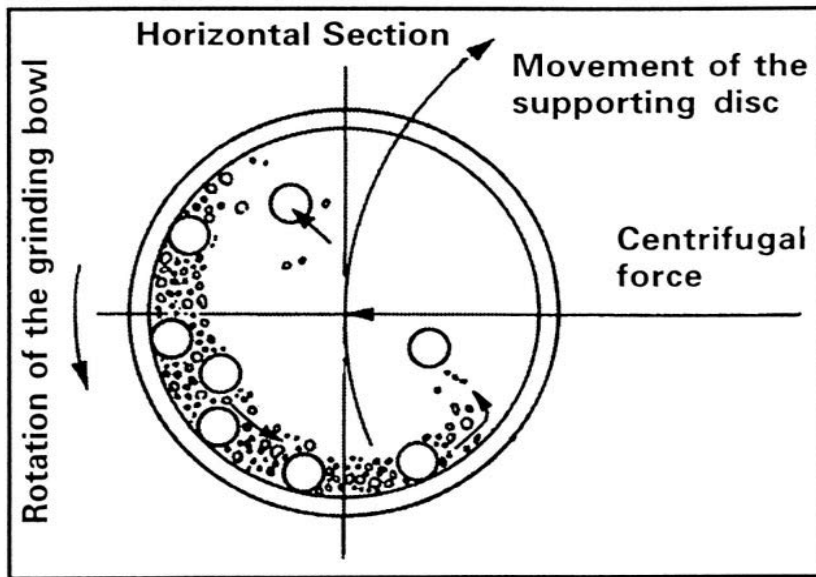


Fig. 2.1: Schematic diagram showing the movement of charge during mechanical alloying. (Suryanarayana, 2001)

2.3 MECHANISMS OF SINTERING

Sintering is the process of subjecting a solid mass of material or metal powders to heat or pressure through compaction by transforming them into coherent solid at temperatures below their melting point. Good mechanical properties can be achieved through sintering due to the possibility of manipulating the processing parameters (Riquet et al., 2019). This could be achieved while powder particles are bonded together by diffusion. Sintering duration, temperature, geometric structure of powder particles, the chemical composition of the powder mix, size and shape of the powder, the density of the powder compact as well as the composition of the sintering furnace atmosphere play significant roles in determining the mechanical properties of a sintered material (Riquet et al., 2019). The sintering method is widely used in fabricating alloys, ceramics, and metal matrix composites at elevated temperatures to produce microstructure with the required properties.

For complete densification to take place, the grain boundary area is expected to be half the original particle surface area (Li et al., 2019a). However, powder compacts are densified at temperatures at which voids or pores are filled by mass transport. Mass transport is driven by the excess free energy associated with the surface area of the powder (Riquet et al., 2019). According to Li et al. (2019a), the configuration of grain boundaries relative to the pores is affected by grain growth during the sintering

process. Hence, a decrease in grain size will increase shrinkage rate if pores are evenly distributed.

Polycrystalline and amorphous materials have different sintering mechanisms. For instance, polycrystalline materials undergo sintering through diffusing matter whereas the amorphous material is by viscous flow (Chawake et al., 2016).

Sintering processes can be categorized as follows: a) vapor-phase sintering – the material is transported from the surface of the particle at high vapor pressure, b) solid-state sintering (Hötzer et al., 2019) – material transport through atomic diffusion and contain only solid phase, c) liquid-phase sintering (Santos and Ribeiro, 2018) - the presence of viscous liquid and capillary pressure aids densification to generate a small amount of liquid phase, and d) reactive-liquid sintering (Sullivan et al., 2012) similar to liquid-phase but liquid disappears while particles react with each other to form new product phases. The table below summarises various transport mechanisms for different types of sintering processes;

Table 2.1: Different Sintering Mechanisms

Types of Sintering	Material Transport Mechanism	Driving energy
Vapor - phase	Evaporation – Condensation	The difference in vapor pressure
Solid-state	Diffusion	The difference in free energy or chemical potential
Liquid - phase	Viscous - Diffusion	Capillary pressure, surface tension
Reactive - liquid	Viscous flow, Solution precipitation	Capillary pressure, surface tension.

The sintering process can be divided into three sequential stages based on physical changes that occur as the material undergo atomic bonding by eradicating pores. The first stage is the “initial stage” where adjacent particles rotate or move to increase the number of points of contact resulting in bonding (L. Coble, 1961). Initial neck formation

occurs at this point resulting in shrinkage with no grain growth (L. Coble, 1961). The second stage is the “intermediate stage” where grain growth begins, and porosity decreases as the centre of each particle merge to another leading to movement of grain boundaries. Most of the shrinkage during sintering happens in this stage, hence, isolating the pores as a continuous network is formed by grain boundaries (L. Coble, 1961). The third stage is called the “final stage” where vacancy diffusion along the grain boundaries as well as grain growth will finally remove porosity. However, grain growth which is driven by surface energy must be adequately controlled to achieve maximum removal of porosity.

Over the years, innovation has been brought into sintering techniques, such as a conventional heating method in a box furnace, hot pressing (HP) (Obadele et al., 2017), hybrid multimode microwave sintering, spark plasma sintering (SPS), or pulsed electric current sintering (PECS) or field-assisted sintering technology (FAST) (Pereira da Silva et al., 2019). However, SPS sintering will be discussed in this project.

2.3.1 Spark Plasma Sintering (SPS)

The spark plasma sintering (SPS) technique gained much usage in the late 1990s for the production of bulk alloys from powders, although it was first discovered in 1960. SPS uses direct current (DC) pulse voltage and current during compaction of as milled alloy powders to produce bulk alloy in solid-state. Spark plasma and spark impact pressure are used to generate high temperatures between the particles causing melting of the surface of the particles during the sintering process (Shongwe et al., 2017). Densification is achieved for both conductive and non-conductive powder in a short time due to the fast heating rate (Shongwe et al., 2017). Eventually, necks are developed at contact areas between the particles which gradually grow during sintering, hence, forming a bulk compact of over 98% density (Saheb et al., 2012). The high-speed movement of atoms will result in high-speed diffusion between the particles within a short period of time. Chakraborty et al. (2016) classify the mechanism of sintering of a bulk alloy using SPS into four stages namely, generation of plasma, heating, vaporization and melting, sputtering of the molten particles, neck growth. Literally, the as-milled powder is directly charged into a graphite die through which current and uniaxial force or pressure are applied simultaneously, resulting in a fully dense material with outstanding mechanical properties (Saheb et al., 2012). The SPS method is widely used especially to synthesis nanocrystalline microstructures,

advanced ceramics, and composite materials, owing to its advantages over conventional sintering techniques (Matizamhuka, 2016). Advantages of SPS include but are not limited to high rate of sintering over a short period of time (Matizamhuka, 2016), flexible sintering temperature, the possibility of eliminating fabrication defects like grain growth and porosity, the possibility of synthesizing nanocrystalline microstructure, easy control of sintering parameters and energy-efficient process. The figure below shows a schematic diagram of the SPS process;

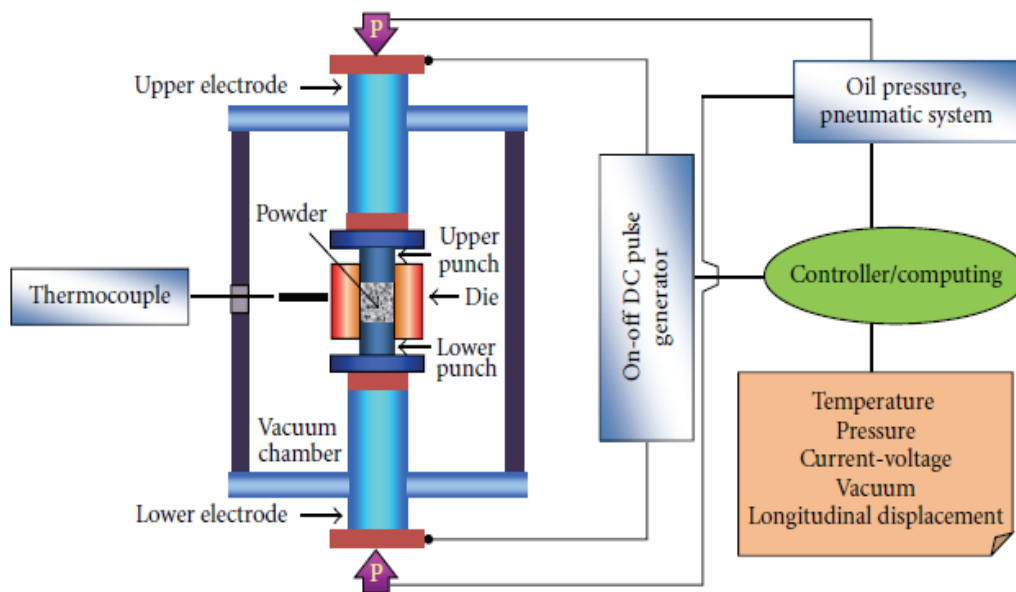


Fig. 2.2: Schematic diagram of SPS process (Saheb et al., 2012)

2.4 INCEPTION OF HIGH ENTROPY ALLOYS (HEAs)

The late 1970s mark the inception of the concept that leads to the discovery of “high entropy alloys”. The thesis of an undergraduate student in the said year was adapted into another project in 1998 (MacDonald et al., 2017). Hence, Professor Brian Cantor of Oxford University and Prof. J.-W. Yeh of National Tsing Hua University independently researched synthesizing crystalline multicomponent alloys. Several journal articles were published in 2004 by Yeh and Cantor describing the synthesis of five or more elements in equiatomic and near-equiatomic concentration to form a metallic alloy. The development and invention of HEAs through Cantor’s work was owing to the undergraduate thesis as mentioned earlier (Murty et al., 2019). Many of these alloys were reported to undergo solid solutions similar to the discovery of arsenical bronzes of third-millennium BCE. However, some compositions were said to

contain a single crystalline structure where a given lattice site was able to be occupied by each constituent element (Murty et al., 2019).

2.5 PROPERTIES OF HIGH ENTROPY ALLOYS (HEAs)

The microstructure and outstanding properties of HEAs could be better explained as a result of four core effects. These effects are high entropy, sluggish diffusion, severe lattice distortion, and cocktail effect. Hence, these effects will be explained in this section.

2.5.1 High Entropy Effect

The high-entropy hypothesis proposes that high configurational entropy in equimolar or near-equimolar alloys with five or more elements may significantly favor single-phase solid solution microstructures (Miracle, 2017). Boltzmann equation 2.1 is used to model the configurational entropy, S , of an ideal solution of N elements, at each equimolar concentration.

$$S = k \ln(N) \quad (2.1)$$

k is the Boltzmann's constant which is equivalent to 1.38×10^{-23} J/K.

Every alloy system is expected to be in an equilibrium state according to thermodynamics when its Gibbs free energy of mixing (ΔG_{mix} Eq 2.2) is at a minimum.

$$\Delta G_{mix} = \Delta H_{mix} - T \Delta S_{mix} \quad (2.2)$$

Eq. 2.2 shows that enthalpy of mixing (ΔH_{mix}) and entropy of mixing (ΔS_{mix}) will determine the minimization of ΔG_{mix} . For HEAs, ΔS_{mix} becomes large which will possibly reduce ΔG_{mix} resulting in more negativity for the system to be more stable.

Thus, for a random alloy system with N number of elements, ΔS_{mix} is given by Eq. 2.3

$$\Delta S_{mix} = -R \sum_i c_i \ln c_i \quad (2.3)$$

R (8.31 J/K mol) is the universal gas constant while c_i is the molar content of i^{th} element. It can be inferred that configurational entropies play a vital role in stabilizing an alloy system that contains N elements in a random solid solution (Yeh et al., 2004a). Configurational entropy of mixing becomes maximum for equiatomic compositions and is given by Eq. 2.4

$$\Delta S_{mix} = R \ln N \quad (2.4)$$

In summary, both entropy and enthalpy must be considered because they both play a more relevant role and also depend on alloy constitution. However, an increase in N will lead to an increase in entropy and will increase the possibility of forming intermetallic compounds (Miracle, 2017). Researchers so far have tried to analyse the effects these parameters could have on the phase formation, leading to different empirical rules being proposed: the formation of intermetallic or solid solution chiefly depends on the entropy of mixing (ΔS_{mix}), the enthalpy of mixing (ΔH_{mix}) as well as the atomic size (δ) (Zhang et al., 2008), (Tian et al., 2015). These parameters must be controlled to achieve a simple phase and not intermetallic: both positive ΔH_{mix} and negative ΔH_{mix} must not be too large to avoid phase separation and generation of intermetallic phases respectively (Tian et al., 2015). Excess strain energy could be generated which could destabilize the simple structure if the δ value is not kept small. Figure 2.3 below shows an individual region where solid solutions, intermetallic compounds, and amorphous phases were formed.

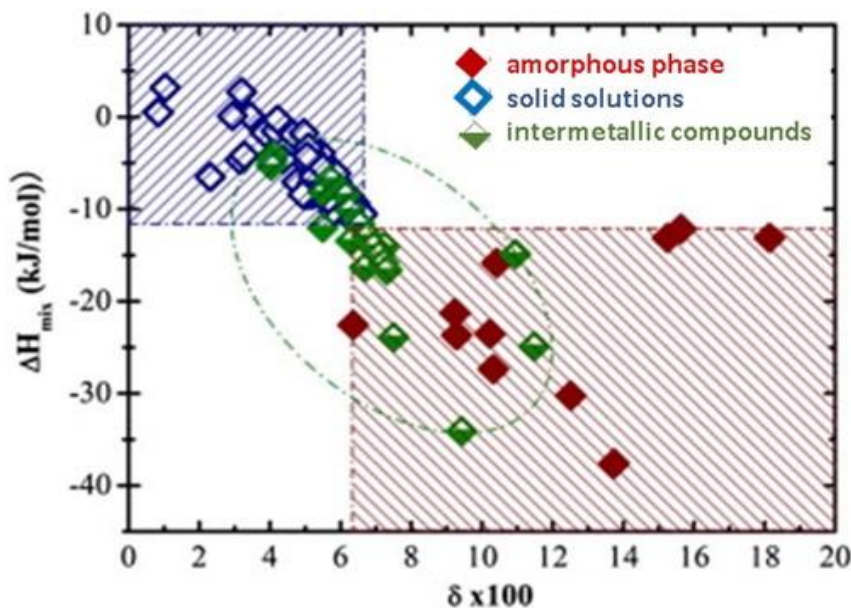


Fig. 2.3: Schematic diagram of the (ΔH_{mix}) against (δ) showing solid solutions, intermetallic compounds, and amorphous phases (Torralba et al., 2019)

There is no doubt that “high entropy” alone cannot be a determining factor for HEA formation. It is also important to note that how frequent elements are used as well as crystal structures of the elements used will influence the resulting phase(s) in the alloy category.

2.5.2 Sluggish Diffusion Effect

The formation of a new phase in an alloy system requires the diffusion of different kinds of atoms for partitioning of composition to take place. Hence, this process is termed diffusion kinetics. Sluggish diffusion not only helps in maintaining structural stability in HEAs at high temperatures but also aids the formation of nanostructure which provides HEAs with remarkable high-temperature strength (Tsai et al., 2013). Due to slower diffusion kinetics in HEAs than in conventional metals and pure metals, this effect makes HEAs highly competitive in applications needing slow diffusion kinetics (Kucza et al., 2018). Sluggish diffusion was hypothesized from closely observing the presence of nanocrystals in as-cast material, noticing how nanocrystals or amorphous materials are being formed in sputter-deposited thin films as well as the elevated recrystallization temperatures (Yeh, 2006a). Tsai et al seminar work in 2013 assumed that inter-diffusion was equal to tracer diffusion. His analysis remains valid as other researchers continue to reference his result and reconfirm his analysis.

Although, it is quite challenging to measure diffusion in alloys with three or more elements, Darken-manning analysis with genetic algorithm optimization methods was used by Dąbrowa et al. (2016). New diffusion data were generated in Al-Co-Cr-Fe-Ni alloys in the process of re-analysing the data from Tsai et al. Both analyses give activation enthalpies for Cr diffusion and identical D_0 . Data shows that Co, Cr, Fe and Ni tracer diffusion from Al-Co-Cr-Fe-Ni and CoCrFeMn_{0.5} alloys are in the same order of magnitude. However, significant differences lie within D_0 and activation enthalpies for Co and Ni.

Cross-diffusion is expected to occur when the chemical composition of elements is affected by the presence of another element in the alloy system (Shewmon, 2016). Dayananda-Sohn analysis has proved effective in extracting the $(N - 1)^2$ inter-diffusion coefficients. The order of magnitude in quasi-binary inter-diffusion coefficients reported by Tsai et al. in CoCrFeMn_{0.5}Ni was found to be the same as the main inter-diffusion coefficients in CoCrFeNi. Hence, Kulkarni and Chauhan (2015) show that inter-diffusion cross-terms cannot be neglected because it's important while Tsai et al. suggest cross-terms should be neglected to facilitate analysis.

The details show that there is no consensus yet on the validity of the sluggish diffusion hypothesis. Miracle (2017) shows that the sluggish diffusion hypothesis holds only when HEA diffusion is compared against a reduced number of elements and simpler alloy. Some reports have shown that an increase in the number of constituents in an

alloy will drag diffusion and may also lower the inverse homologous temperature relative to the constituent elements. Hence, these effects are inseparable. According to Miracle (2017), the rate of diffusion seems to be faster in HEAs than in their constituent elements and simpler alloy when the comparison is not normalized by inverse homologous temperature due to the lower inverse homologous temperature having a stronger influence. It has been suggested that abundant low lattice potential energy (LPE) sites serve as a trap which hinder atomic diffusion and is accounted for slowing down the diffusion rate. It has been suggested that relatively higher negative heat of mixing causes atoms to jump towards another while higher positive heat of mixing will make the atoms to do otherwise in HEAs. In conclusion, fine precipitate and controlled grain structure is usually formed as a result of sluggish diffusion effect which will eventually strengthen HEAs.

2.5.3 Lattice Distortion Effect

Yeh (2006a) postulated that the 'increased strength' property of high entropy material as a result of severe lattice distortion is owing to the random arrangement of different sizes of atoms distributed in a crystal lattice and the slower kinetic process. *Figure 2.4* shows typical examples of BCC and FCC crystal structures of five (5) principal elements. Toda-Caraballo and Rivera-Díaz-del-Castillo (2016) describe lattice distortion using two parameters; (1) the inter-atomic distance mismatch or unit cell parameter which is similar in behavior to that shown by atomic size mismatch; (2) bulk modulus variation of their constituent element exhibit high possibility of identifying crystal structure of the HEAs alloys in the database (Toda-Caraballo and Rivera-Díaz-del-Castillo, 2016). The above parameters can be used to identify solid-solution displayed composition in the database (Toda-Caraballo and Rivera-Díaz-del-Castillo, 2016).

High lattice strain and stress are generated in a multi-elemental solid solution of HEAs as a result of different atomic radii associated with the individual element (MacDonald et al., 2017). It is noteworthy to know that most HEAs have no differentiation between solute elements and solvent elements. Hence, displacement from the perfect crystal lattice site is expected to occur in every lattice site (MacDonald et al., 2017). However, it is difficult to measure the local atomic displacements or the local lattice strains. Zou et al. (2014) use lattice fringes traced on fast Fourier transform images from high-resolution TEM images to display local distortions and measure lattice strains. Single-

crystal diffraction can be used to obtain atomic displacement parameters (ADPs) but the interpretation of the atoms as well as consequences of distortion remains unclear at this stage (Zou et al., 2014). Total scattering measurements with neutron radiation were adopted by Owen et al. (2017) to study the severity of the distortion. Owen et al. (2017) obtained the pair distribution function of CrMnFeCoNi and discovered the presence of a considerably higher amount of lattice strain in HEAs compared to less complex compositions within the alloy system. This indicates that the pair distribution function is directly related to the distribution of the interatomic spacing on a local atomic level. This observation could be used to discuss the mechanical behavior of HEAs when analyzing their properties.

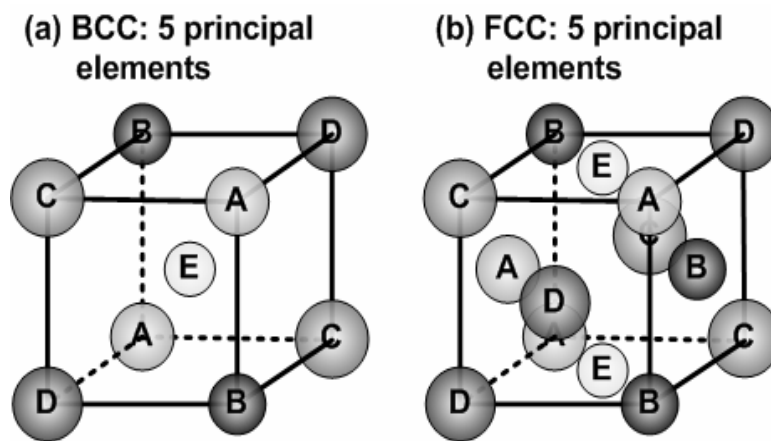


Fig. 2.4: Examples of (a) BCC and (b) FCC crystal structures having five principal elements (Xiao et al., 2020)

2.5.4 Cocktail Effect

Under this effect, it was suggested that there is a possibility of achieving unexpected properties in a HEA system from mixing different elements in a chosen proportion. Hence, resulting properties from this HEA are supposed to surpass the individual elements that make up the system. HEAs' properties are known to be a result of the overall contribution of the constituent phases influenced by phase shape, phase distribution, and boundaries as well as properties of each phase (Yeh, 2013). The 'cocktail' effect does range from atomic-scale, multi-element composite effect to microscale and multiphase composite effect (Yeh, 2013). This effect along with high mixing entropy, therefore, provides researchers with flexible results (Miracle and Senkov, 2017). It can be assumed that HEA properties can be manipulated by

adjusting the number and mixing ratio of the individual elements. An instance of this design approach is the inclusion of Al and Si in a certain proportion in HEA to improve oxidation resistance and reduce its density. This approach is applicable throughout conventional alloy design but not particular to only HEAs (MacDonald et al., 2017). Research has proven that the addition of a single element like Cu could play an important role in stabilizing the FCC phase in $Al_xCoCrCuFeNi$ and $CoCrFeNiAl_x$ alloy systems (Tong et al., 2005b), (Kao et al., 2009). The microstructure and properties of the system can as well be influenced as a function of a single element such as Al content in an alloy like $CoCrFeNiAl_x$ HEAs (Zhang and Wang, 2012). For instance, if a BCC phase is formed as a result of adding Al to the matrix of elements such as Cr, Cu, Co, Fe, and Ni, a substantial increase in strength will take place. *Figure 2.5* shows an increase in hardness on $CuCoNiCrAl_xFe$ due to aluminum addition.

A positive cocktail effect was realized by Zhang et al. (2013) to achieve high magnetization, low coercivity, good plasticity, high strength, and high electrical resistance in $FeCoNi(AlSi)_{0.2}$. Zhang et al. (2013) researched $FeCoNi(AlSi)_{0-0.8}$ alloys to find the best composition that could yield an optimum combination of magnetic, electrical, and mechanical properties. Alloy $FeCoNi(AlSi)_{0.2}$ stood out to be the best, having saturation magnetization (1.15 T), yield strength (342 MPa), coercivity (1,400 A/m), electrical resistivity ($69.5 \mu\Omega cm$), and strain without fracture (50%) (Zhang et al., 2013). All these properties prove the alloy to be an excellent, soft magnetic material alternative for many potential applications. There is no doubt that selection of equimolar ferromagnetic elements (Fe, Co, and Ni) was observed when designing this alloy because of the formation of ductile FCC phase with higher atomic packing density than BCC. Zhang et al. (2013) also observed that suitable addition of nonmagnetic elements (Al and Si having a little bit of anti-parallel magnetic coupling with Fe, Co, and Ni) to increase lattice distortion.

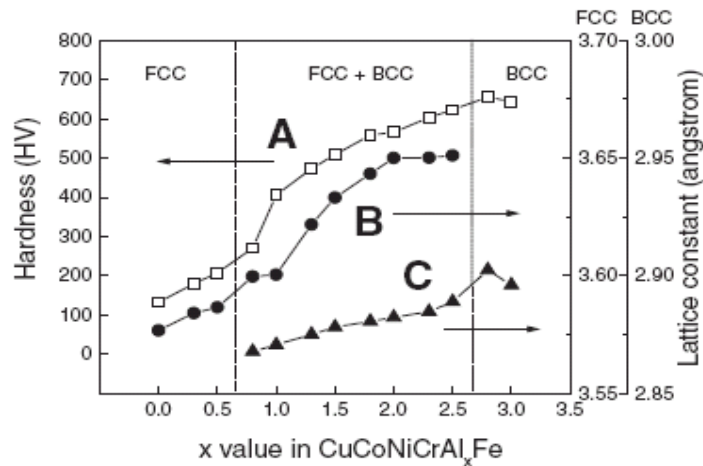


Fig. 2.5: Hardness effect of aluminum addition on the cast $\text{CuCoNiCrAl}_x\text{Fe}$ alloys. A, B and C refer to the hardness while FCC and BCC are lattice constant (Lee, 2020)

2.6 SYNTHESIS OF HIGH ENTROPY ALLOYS (HEAs)

Various processing methods have been adopted so far for the synthesis of HEAs over the years, such as the melting and casting route, powder metallurgy route, coating, and spraying. These methods have shown various simple solid solutions and solid solutions plus intermetallic microstructures. Hence, these methods will be discussed in detail in this section.

2.6.1 Melting and Casting Route

This processing technique has been widely adopted for synthesizing conventional alloys due to its economical advantage, reduced synthesis time, and energy saving when compared with other techniques (Otto et al., 2013). For this reason, a large percentage of HEAs reported so far have been synthesized by this route using the arc melting method. Although, there is a possibility of melting most of the elements in the periodic table due to the ability to attain high temperatures ($\sim 3000^\circ\text{C}$) with arc melting (Tong et al., 2005a). Unfortunately, elements with a very low melting point like Mg, Mn, and Zn could evaporate at a high temperature which could result in changes in the stoichiometry of the alloy during synthesis. However, elemental segregation causes the formation of dendritic and inter-dendritic microstructures at a low cooling rate when synthesizing HEAs using the melting and casting route (Tong et al., 2005a). Singh et al. (2011) discovered the presence of both inter-dendritic as well as a dendritic region in a multi-component decomposed AlCoCrCuFeNi HEA. Melt spinning, suction casting, injection casting, drop-casting, and splat quenching are some of the rapid cooling techniques adopted in HEAs. In the case of HEAs synthesized by melting and

casting route, the kinetics of cooling has more effect on stabilizing the solid solution microstructure than thermodynamics of the system (Li et al., 2009).

Bridgman solidification is another processing method that involves melting and casting. Polycrystalline material is heated above its melting point and subjected to a slow cooling from the end where a seed crystal is located. This results in the growth of a single crystal with the same crystallographic orientation as the seed, this is eventually formed along the length of the container. Below is the schematic diagram of the Bridgman solidification;

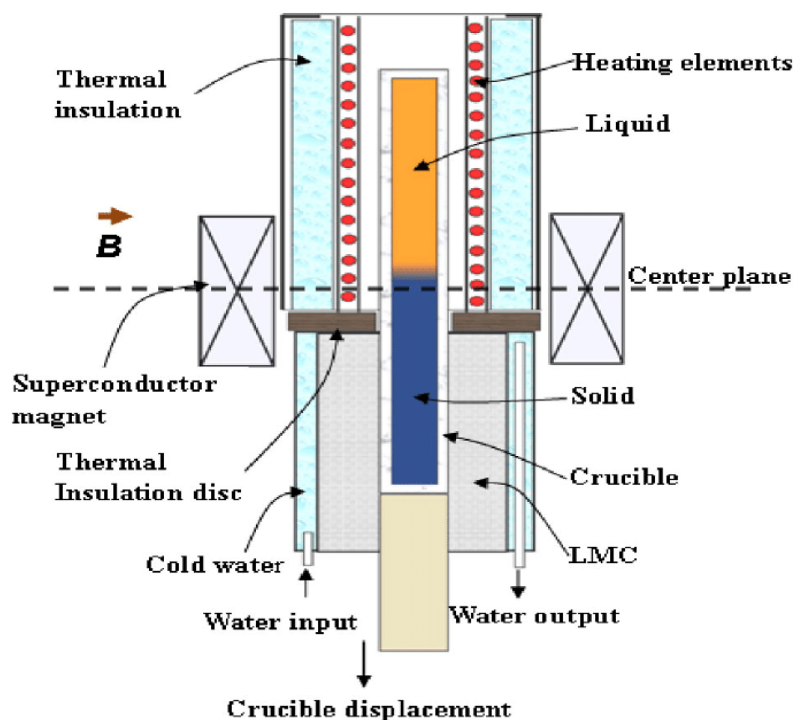


Fig. 2.6: Schematic diagram of the Bridgman solidification process (Li et al., 2014)

2.6.2 Powder Metallurgy Route

This is a mechanical way of synthesizing both miscible and immiscible elemental powder blends in a solid state to form an alloy. A high-energy ball mill is used in this process to enhance plastic deformation which also reduces time. Mechanical alloying (MA) has been given more preference recently compared to conventional methods like melting and casting. Hence, it has proven to be a more convenient and cost-effective way of synthesizing nanocrystalline materials with uniform microstructure. This processing route has resulted in the improvement in properties such as high strength/hardness, resistance to oxidation, wear, and corrosion in HEAs (Ji et al., 2015).

Ji et al. (2015) synthesized an equiatomic high entropy alloy of CoCrFeNiMn by mechanical alloying (MA) and spark plasma sintering (SPS). The milling time was 60h at 250rpm in argon atmosphere, the ball to powder mass ratio used was 15:1, PCA used was N-heptane, milled powder was sintered at 800⁰C for 10min under a pressure of 50 MPa. A solid solution with a refined microstructure of 10nm consisting of both FCC and BCC phases was noticed during MA, while the FCC phase only was detected after SPS consolidation. Massive compressive strength of 1987 MPa was achieved by the HEA through this processing route and the novel magnetic transition was discovered. This is associated with structure coarsening and phase transformation (Ji et al., 2015).

A non-equiatomic Ni_{1.5}Co_{1.5}CrFeTi_{0.5} HEA was synthesized using a combination of MA and SPS by Moravcik et al. (2016). The ball-to-powder ratio used was 10:1, dry milled at speed of 250 rpm for 30h, additional 2h of wet milling in toluene was carried out. SPS was performed in vacuum at a pressure of 30MPa, the heating rate used was 100K/min with 15min dwell time at a temperature of 823K. The heating rate was later reduced to 50K/min at 1273K to 1373K and later to 20K/min at a temperature of 1373 to 1423K. FCC single-phase solid solution with extremely fine-twinned grains was formed in the microstructure. Moravcik et al. (2016) reported that 2593 MPa was achieved on Ni_{1.5}Co_{1.5}CrFeTi_{0.5} HEA when subjected to bend strength test, the elastic modulus of 216 GPa, the tensile strength of 1384 MPa, elongation to fracture of 4.01% and microhardness of 442 HV0.3 was achieved on the HEA. The excellent properties reported on the alloy were associated with the processing route in contrast to cast materials.

The microstructure and properties of an inequi-atomic nanocrystalline Co_{0.5}FeNiCrTi_{0.5} HEA were investigated through MA and SPS by Fu et al. (2013). Dry milling was performed on the alloy for 45h followed by wet ball milling for another 4h in ethanol at 300rpm. The ball-to-powder ratio used was 10:1 under argon atmosphere, SPS was conducted at 1273K for 8min with a pressure of 30MPa. Results show that both BCC and FCC phases were observed after MA while only FCC crystal structure remained with additional sigma phase after SPS. In addition, several other phases were found in the alloy after SPS was performed. The alloy exhibited a yield strength of 2.65GPa, compressive strength of 2.69GPa, micro-hardness of 846HV, and compression ratio of 10.0% according to Chen et al. (2013). The excellent mechanical properties were attributed to the synthesis route.

According to research conducted on a light-weight refractory $\text{Al}_{0.1}\text{CrNbVMo}$ HEA fabricated mechanically through a powder metallurgical process by Kang et al. (2018). Milling was conducted for 12h at a speed of 200rpm with a ball-to-powder ratio of 10:1 with no process control agent (PCA). It was ensured that 0.5g of powders were constantly removed periodically at intervals of milling to determine the milling behavior of the ball mill powders. Kang et al. (2018) reported that the milled powders were heated to 600°C within 1min and further heated to 1200°C afterward at a heating rate of $100^{\circ}\text{C}/\text{min}$ at 50 MPa during sintering. It was held at 1200°C for 5min while the alloy was heat treated inside a tube furnace for grain growth at temperatures 1250 and 1450°C for 16h under argon and later furnace cooled. The alloy exhibited a BCC phase with a little inclusion of aluminum according to Kang et al. (2018). The density of 7.96 g/cm^3 , compressive strength of 2863 MPa at room temperature and 1405 MPa at 1000°C as well as the yield strength of 176 MPa cm^3/g at 1000°C were recorded for the alloy.

2.7 SYNTHESIS OF LIGHT-WEIGHT HIGH ENTROPY ALLOYS (LWHEAs)

Light-Weight High Entropy Alloys (LWHEAs) have gained the attention of researchers recently due to the possibility of energy-saving applications like automobile and aerospace. This has prompted the researchers to successfully develop various processing routes, and the need to examine the effects on the alloys is very important. The effect of the fabrication route on alloys, especially LWHEAs can never be underestimated because of the possibility of manoeuvring its properties along the process route (Joseph et al., 2018). Optimizing the processing parameters is an important factor in achieving the desired microstructure that determines the properties of LWHEAs. Low-density HEAs were generally synthesized using elements such as Al, Li, and Mg.

Sanchez et al. (2019) designed some low-density, multi-principal component alloys (MCAs) using high-entropy alloys mixing, guided by (CALculation of Phase Diagrams) CALPHAD. $\text{Al}_{40}\text{Cu}_{15}\text{Cr}_{15}\text{Fe}_{15}\text{Si}_{15}$, $\text{Al}_{65}\text{Cu}_5\text{Cr}_5\text{Si}_{15}\text{Mn}_5\text{Ti}_5$, and $\text{Al}_{60}\text{Cu}_{10}\text{Fe}_{10}\text{Cr}_5\text{Mn}_5\text{Ni}_5\text{Mg}_5$ were melted under a high-purity argon atmosphere and cast through large scale vacuum die casting. The microstructure of the alloys was complex multiphase containing both fractions of disordered solutions and intermetallic compounds when characterized. Densities of the alloys range from 3.7 g/cm^3 to 4.6 g/cm^3 while microhardness varies from 743 Hv to 916 Hv. Pioneering LWHEA

(Al₂₀Li₂₀Mg₁₀Sc₂₀Ti₃₀) was also nanocrystalline and a low density of 2.7 g/cm³ was recorded while the hardness of 591Hv was achieved in the alloy.

Qiu et al. (2017) fabricated an equiatomic AlTiVCr alloy through a non-flammable and non-hazardous conventional arc melting system under an argon atmosphere on a water-cooled copper hearth. A simple single-phase consisting of the B2 phase and disordered BCC phase were realized, and the B2 phase is said to be more stable than the disordered BCC phase over a wide range of temperatures (Qiu et al., 2017). Although the disordered BCC phase was stable at a higher temperature. Empirical relationships show that this four-element AlTiVCr light-weight HEA is seen as a uniform single-phase compositional complex alloy of the B2 phase. Exceptionally high hardness of about 500 HV was achieved in the alloy due to the B2 structure with a density of 5.06 gcm⁻³.

A light-weight AlCoCrFeNi HEA with different initial microstructures was synthesized by utilizing the cooling rate effect via levitation melting (LM) and arc-melting (AM) system. According to Tian et al. (2019), dendrite solidification (Al & Ni) surrounded by inter-dendritic (ID) regions (Fe & Cr) were formed in a body-centered cubic (BCC) AlCoCrFeNi HEAs samples. It was reported that the cooling rate might have caused samples fabricated by arc melting to have higher volume fractions of dendrite regions than the samples formed by levitation melting. The yield strength decreased from 1631 MPa for the LM sample to 1209 MPa for AM sample while micro-hardness was also decreased from 519 ± 21 HV for the LM sample to 493 ± 15 HV for AM sample. This shows that levitation melting formed samples exhibited higher hardness and compressive yield strength than the arc-melting formed sample. Hence, AM sample has better plasticity, although at the expense of yield strength.

2.8 Al₂₀Be₂₀Fe₁₀Si₁₅Ti₃₅, ELEMENTAL COMPOSITION AND ENTROPY ALLOY CLASSIFICATION

The discovery and application of alloying and composite technology have led to the achievement of a wide range of properties being realized from various categories of materials. This has led to the formation of one or two principal elements forming solid and/ or intermetallic compounds coined “low entropy alloy” (LEA)($\Delta S_{\text{conf}} \leq 1.0R$) (Gupta, 2017). “Medium entropy alloy” (MEA) having two to four principal elements were also formed ($1.0R \leq \Delta S_{\text{conf}} \leq 1.5R$). “High entropy alloys” (HEAs) ($\Delta S_{\text{conf}} \geq 1.5R$) have at least five principal elements usually forming single-phase solid solutions in a

disordered manner (Gupta, 2017). It has been established that a specific class of HEAs was suitable for a particular set of engineering applications due to their limited material properties. Hence HEAs are categorized based on elemental composition and configurational entropy backing up Yeh's research, according to Miracle and Senkov (2017).

Some of the categories of HEAs are "ceramic HEAs", it was discovered when covalently and ionically bonded materials were formed due to a mixture of metal cations with oxygen, boron, and some anions to form metal diborides, oxides, and perovskite structures (Li et al., 2019b). "Lanthanides HEAs" have also been reported, formed from at least four of lanthanides (4f) elements Gd, Lu, Tb, Dy, and Tm with the element Y as well as bronzes and brasses with some precious metals (Au, Ag, Co, Cr, Cu Pt, Rh, and Ni) (Li et al., 2019b). These alloys mostly use the equiatomic system, hence, a single-phase hcp has been reported especially from MoPdRhRu alloy with a significant amount of strength (Li et al., 2019b). On the other hand, Miracle and Senkov (2017) emphasize the need to categorize alloys containing other unknown phases as well as alloys whose microstructural stability does not align with Boltzmann mixing entropy. The proposed given names are "multi-principal element alloys (MPEAs) and "complex concentrated alloys (CCAs).

High-temperature alloys or high entropy superalloys (HESAs) are otherwise known as refractory high entropy alloys (RHEAs). These are transition-metal-based classes of HEAs, basically, mostly formed from 38 transition metals, such as NbMoTaWVTi, NiAlCoCrFeTi, and CrMnFeCoNi developed for exceptionally high-temperature applications up to 1400°C (Senkov et al., 2016).

However, due to the shortcoming of the strength-to-density ratio as well as oxidation resistance of RHEAs. Some material scientists designed another alloy using low-density non-transition elements such as Li, Mg, Al, and Si and this resulted in a low density below 4 g/cm³ in the alloy. This system provided a solution to the problem of a high density of RHEAs and the term "light-weight high entropy alloys" (LWHEAs) was coined. The inclusion of Li and Mg in synthesizing LWHEAs is discouraging owing to their low melting point and Li highly reactive nature. Al and Si will be included due to their oxidation-resistant properties, Fe is readily available and less expensive while Ti is preferred to improve mechanical and corrosion properties. Beryllium is expected to reduce density since the aerospace industry uses it for lightweight structural components. Hence, Al₂₀Be₂₀Fe₁₀Si₁₅Ti₃₅ LWHEA will be synthesized through MA and

SPS and its mechanical and corrosion behaviour will be examined. The table 2.2 below summarizes some HEAs processed via different processing methods, strengthening mechanisms used, and the effect on mechanical properties.

Table 2.2: HEAs processed via different processing methods, strengthening mechanism used, and the effect on mechanical properties (Onawale et al., 2021)

HEA Composition	Observed Phase(s) through Different Processing Route(s)			Strengthening Mechanism in Respective Processing Route(s)			Effects on Mechanical Properties		
	Melting and Casting	MA + SPS	AM	Melting and Casting	MA + SPS	AM	Melting and Casting	MA + SPS	AM
CoCrFeNiMn	FCC	FCC	FCC + BCC		Solid solution strengthening	Grain boundary strengthening		Compressive strength of 1987 MPa Hardness of 646 HV	Tensile strength of 601 MPa
CoCrFeNiAl _{0.3}	FCC	FCC + BCC	FCC	Grain boundary strengthening	Solid solution strengthening	Dislocation hardening	UTS of 528 MPa YTS of 275 MPa	Compressive strength of 1907 MPa Hardness of 625 HV	YS of 730 MPa UTS of 896 MPa
CoCrFeNi		FCC + Cr ₇ C ₃	FCC		Grain boundary strengthening (470 HV), precipitation strengthening			Hardness of 580 HV	
AlCoCrCuFeNi	FCC + BCC	FCC + BCC	BCC	Solid solution strengthening	Grain boundary strengthening, solid solution strengthening		Hardness of 515.5 HV (5.056 GPa) Compressive strength of 1.82 GPa	Hardness of 8.13 GPa Elastic modulus of 172 GPa	
TiZrNbMo _{0.3} V _{0.3}	BCC		FCC + BCC	Solid solution strengthening			Yield strength of 1312 MPa and 50% increase in plastic strain YS of 896 MPa	Hardness of 442 HV0.3	
Ni _{1.5} Co _{1.5} CrFeTi _{0.5}	FCC	FCC		Solid solution hardening	Grain boundary strengthening		Compressive strength of 1502 MPa Hardness of 515 HV	Tensile strength of 1384 MPa Elastic modulus of 216 GPa	

$Al_{0.7}FeCoCrNi_{1.3}$	FCC + BCC		Precipitation strengthening by the B2 NiAl phase in an Fe-Cr-Ni matrix	A good compromise between hardness (280 HV) and strength
			Grain boundary precipitation of the Ni-Al-rich phase	
$(FeCoNiCr)_{94}Ti_2Al_4$	FCC	Precipitation hardening (327.7MPa), dislocation hardening (274.5 MPa), grain boundary hardening (122.6 MPa)		Accumulated yield strength of 645 MPa
$CuCr_2Fe_2NiMn$	FCC	Precipitation hardening of the ρ phase		Hardness of 450 HV
$FeCrNiCoMn$	FCC	Grain boundary strengthening		Increase in yield strength from 200 to 350 MPa
$Al_{0.3}CrFe_{1.5}MnNi_{0.5}$	FCC + BCC	Precipitation hardening		Hardness of 800 HV
$Ni_2CoCrFeNb_{0.15}$	FCC	Precipitation strengthening (670 MPa), solid solution hardening (41.7 MPa)		Total yield strength of (954 MPa) Ductility (27%) Excellent yield strength–ductility combination
$Al_{0.5}CrFeNiCo_{0.3}C_{0.2}$	FCC + BCC		Solid solution strengthening	Compressive strength of 2131 MPa

				Hardness of 617 ± 25 HV
CoCrFeNiMo _{0.3}	FCC	Precipitation hardening	Tensile strength of 1.2 GPa and good ductility of ~19%	
			Grain boundary strengthening (61.3%),	Yield strength of 1652 MPa
			precipitation strengthening (20.6%),	
			dislocation strengthening (15.0%)	Hardness of 461 HV
			Grain boundary strengthening,	Compressive yield strength of 1795 MPa
			dislocation strengthening	Hardness of 454 HV

2.9 THERMAL ANALYSIS AND STABILITY

Thermal analysis (TA) is the process of analysing the effect of temperature changes on sample properties (Feist, 2015). Properties such as mass, dimensions, dielectric permittivity, thermal diffusivity, mechanical rigidity, optical properties, and thermal stability fall under this context. In other words, thermal analysis refers to the application of various techniques in determining changes in material properties when subjected to heat, cooled, or maintained at a constant temperature. It also provides a useful overview of the properties of materials. These techniques are distinguished engineering tools for developing new materials based on their properties.

Thermal stability can be explained as the ability of an alloy or a material to retain its properties, such as strength, toughness, or elasticity after being subjected to high temperatures (Bousahla et al., 2016). Thermal stability is an important design characteristic of engineering alloys that find applications at elevated temperatures. Microstructural components such as phase composition, phase morphology, and solute in the matrix are expected to evolve during heating (Bousahla et al., 2016). Thereby resulting in fluctuation within an alloy microstructure due to diffusion of alloying element. Differential scanning calorimetry (DSC) or thermogravimetric (TG) analysis could be used to evaluate the thermal stability of alloy materials.

Thermogravimetric analysis (TGA) is a thermoanalytical analysis technique where thermobalance (an electronic balance with a furnace and temperature controller) measures changes in the mass of a sample. This technique is used to analyse a loss of alloy weight due to decomposition, oxidation, or evaporation of volatiles in a specific temperature range, yielding typically a plot of temperature (or time) versus mass (or mass percentage). Thermal stability, oxidative stability, life expectancy, and decomposition profile can also be determined by TGAs (Polini and Yang, 2017). The substance under study is either heated or cooled at a controlled rate and the weight of the substance is recorded as a function of time and temperature. If the temperature varies during the study, then the weight is plotted as a function of temperature, hence the weight is plotted as a function of time if the temperature is kept constant. The weight change is used for

quantitative analysis and the temperature at which the change in weight takes place can be used for qualitative analysis.

TG is composed of a sample pan and a precision balance. During the experiment, the sample pan in the TG equipment is heated or cooled in a furnace and mass measurements are taken using thermobalance. The experiment could be carried out in a controlled atmosphere such as inert gas through the method of dynamic TGA, static TGA, or quasistatic TGA. During dynamic TGA, the temperature increases over time as the mass is recorded, hence, it is possible to simultaneously identify how much gas is removed and at what temperature. Mass is being measured at a constant temperature during the static TGA method. In quasistatic TGA, the sample is heated in multiple temperature intervals and held at those temperatures for some time, often until the mass stabilizes. This method is ideal for analyzing materials that could decompose in different ways and at different temperatures (Laye, 2002). The figure below shows the schematic representation of a TG system.

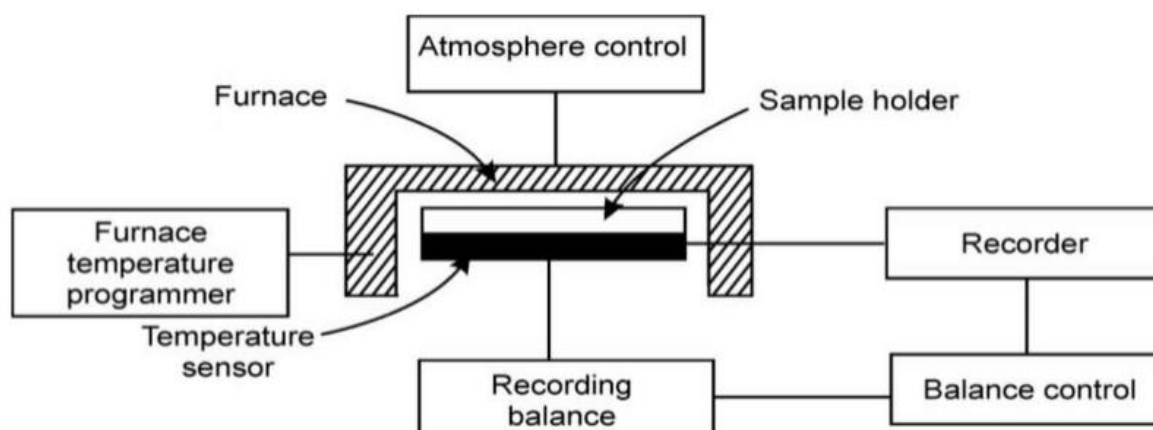


Fig. 2.7: Schematic diagram of a typical TG system

2.10 DIFFERENTIAL SCANNING CALORIMETRY (DSC)

Thermal analysis by differential scanning calorimetry (DSC) involves the measurement of heat flow into and out of a material sample as a function of temperature under a controlled temperature environment (Akash and Rehman, 2020). Therefore, DSC is a thermoanalytical technique for studying the thermal effect. This technique can be used to evaluate specifications such as glass transition temperatures, crystallization, melting points, oxidation behavior, specific heat capacities, and thermal stability (Laye, 2002, Akash and Rehman, 2020). DSC measures the rate of heat flow and compares it with known reference materials to determine whether it differs from the test sample (Akash and Rehman, 2020). Materials vary in their compositions, crystallinities, and oxidation degrees depending on the difference. DSC analysis can be performed on a wide range of materials, including polymers, powders, composites, laminates, plastics, adhesives, pharmaceuticals, food, coatings, organic materials, rubber, explosives, petroleum, chemicals, and biological samples (Wielgosz and Kargul, 2015, Knopp et al., 2016, Müller and Michell, 2016). It is an essential tool for examining the phase changes taking place in an amorphous material as a function of temperature (Wielgosz and Kargul, 2015).

The glass transition is one of the fundamental phase changes that occur in amorphous materials when subjected to heat (Müller, 2015, Alves et al., 2002). The amorphous material changes from relatively hard state to a rubbery state through changes in its structure during glass transition. Hence, this gives more insight into the stability of glassy or amorphous materials. Crystallization is another phase changes that occur in amorphous materials when subjected to heat (Din et al., 2020, Uskoković et al., 2018). This is an irreversible phase change that comprises the nucleation and growth of a disordered structure, hence, resulting in a crystalline structure. Amorphous materials being subjected to heat could also experience melting, this is a phase change that occurs when a crystalline lattice breaks into disorder (solid to liquid transition, "fusion"). Although crystallization is a two-step exothermic process (nucleation and growth), fusion is a single-step endothermic process (Din et al., 2020).

There are two known types of DSC namely; power compensated DSC and heat-flux DSC (Gaisford et al., 2019). According to Toda (2016), each consists of different components as well as different working principles. For instance, the furnace of a power compensated DSC contains separate blocks for heating samples and reference points, while a heat flux DSC has a single block for heating samples and references. As a result, power compensated DSC maintains the temperature difference between a sample and reference constant while the differential thermal power measures the amount of heat to be distributed. On the other hand, the heat flux DSC method allows for the measurement of the temperature difference between the sample and the reference. This is used to determine the amount of heat flow. Although power compensated DSC can elucidate more thermal changes taking place while the sample is being heated than the heat flux DSC but heat flux DSC is more sensitive to thermal changes (Gaisford et al., 2019). Below shows a schematic representation of a generalized DSC system.

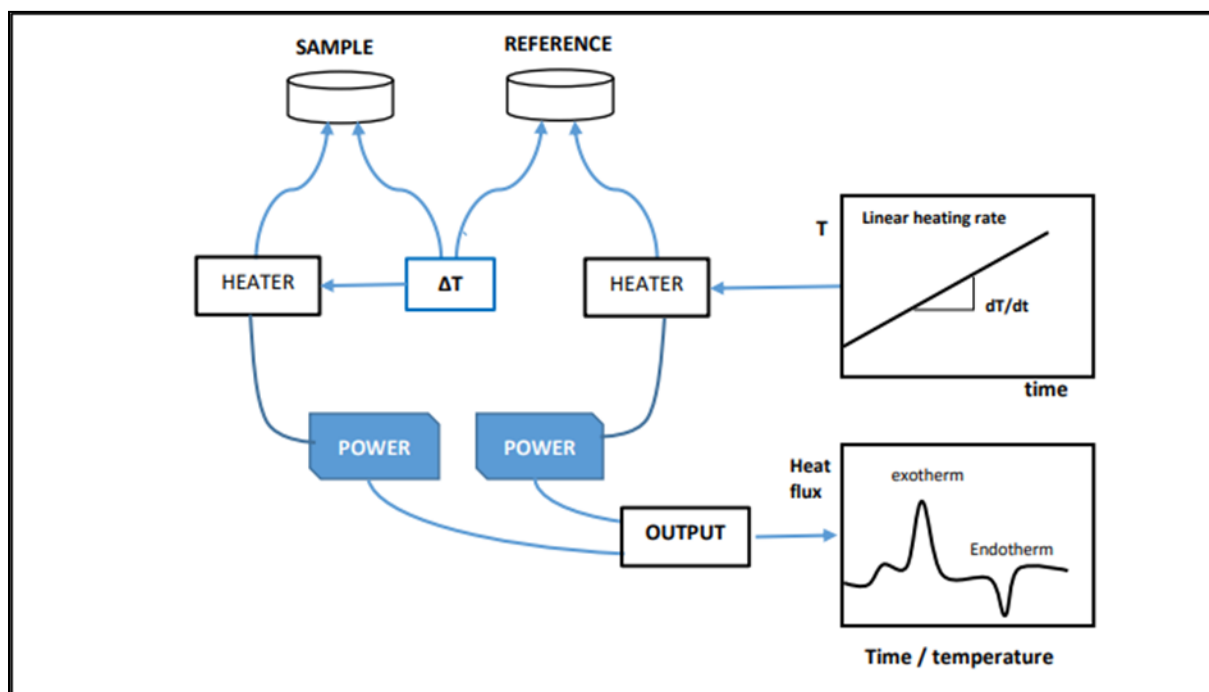


Fig. 2.8: schematic diagram of a DSC system (Brown, 2001)

The sample tends to release or absorb heat during heating due to phase transitions occurring within it (Sun et al., 2018). To maintain the same temperature for both sample and reference, heat should be supplied to the sample undergoing phase transitions. Exothermic or endothermic reactions in the sample are determined by the amount of heat provided or withdrawn (Dołęga et al., 2021). Monitoring the amount of heat transferred to the sample is displayed through a computer that generates a thermogram displaying exothermic and endothermic peaks. Different conventions are used to represent exothermic and endothermic processes. Positive and negative reactions are shown in opposite directions depending on how the instrument is designed and its conventions. In addition, DSC detects any shift in the flow of heat through a sample. The detection extends beyond glass transitions and melting. Solid-state transformations such as eutectic points, melting, recrystallization, and dissolution of crystalline phases, curing exotherms, degradation, loss of solvents, and chemical reactions can be observed (Fernandes et al., 2014, Dołęga et al., 2021).

Thermogram gives information on characteristics of the material under consideration, such as heat capacity, temperature, and enthalpies of phases like glass transition, crystallization, or melting.

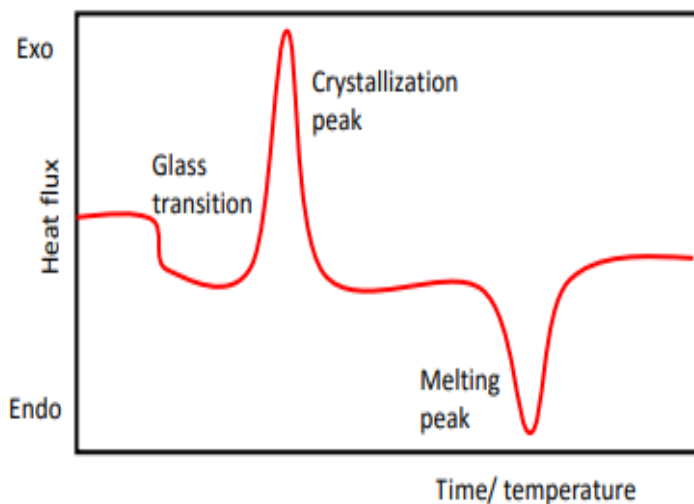


Fig. 2.9: A typical DSC thermogram (Brown, 2001)

A material's heat capacity is determined by the amount of heat it needs to raise its temperature by 10°C. It's calculated by dividing the amount of flow of heat by the rate of heating. In other words, heat flow equals heat flowing per unit time. Mathematically, heat-flow = heat/time = q / t , and the heating rate is the temperature change rate over time, so $\Delta T / t$, where t and T represent time and temperature, respectively. Hence, heat capacity can be represented by the equation below (Sarge et al., 1997, Ferrer et al., 2017);

$$C_p = \frac{q/t}{\Delta T/t} = \frac{q}{\Delta T} \quad (2.5)$$

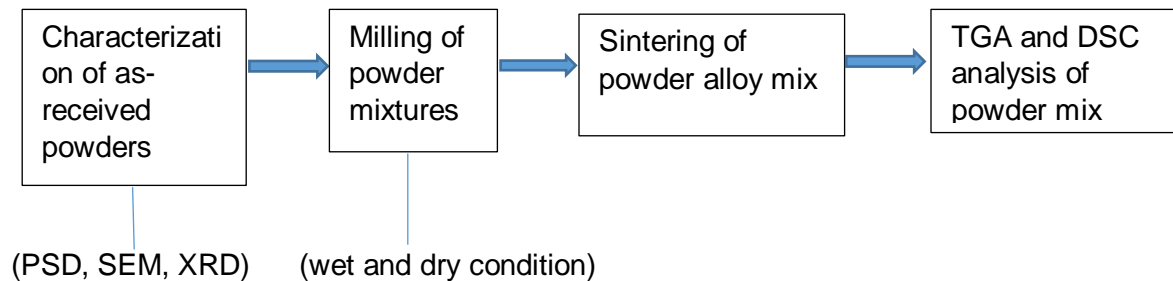
Thus, the slope of heat supplied versus increase in temperature gives the value of heat capacity of that sample.

3.0 RESEARCH METHODOLOGY

3.1 RESEARCH APPROACHES

Literature survey: Further studies on published works related to mechanical properties and corrosion behavior of $\text{Al}_{20}\text{Be}_{20}\text{Fe}_{10}\text{Si}_{15}\text{Ti}_{35}$ HEAs and similar LWHEAs were carried out. Apparently, previous research on synthesizing this alloy using MA and SPS is so limited. Hence a full study on the challenges associated with synthesizing $\text{Al}_{20}\text{Be}_{20}\text{Fe}_{10}\text{Si}_{15}\text{Ti}_{35}$ HEAs alloy using MA and SPS has been properly harnessed for better understanding and analysis.

3.2 EXPERIMENTAL PROCEDURE



3.2.1 CHARACTERIZATION OF AS-RECEIVED POWDERS

Al, Be, Fe, Si, and Ti powder were purchased in powder form from afrox gas, afrox.

3.2.1.1 Particle Size Analysis (PSD)

Starting particle size of Al, Be, Si, Fe and Ti element were determined by Malvern particle size analyzer instrument as shown in figure 3.1 below;



Fig. 3.1: Malvern particle size analyser equipment

3.2.1.2 Scanning Electron Microscopy (SEM)

Each as-received powder was viewed under JEOL JSM-IT500 scanning electron microscopy (SEM) machine equipped with EDS in figure 3.2 below and images were taken at specific magnifications.



Fig. 3.2: JEOL JSM-IT500 scanning electron microscopy (SEM) machine equipped with EDS

3.2.1.3 X-Ray Diffractometry of Individual Elements of As-received Powder

The as-received powders were later characterized using XRD PANalytical machine shown in figure 3.3 below, to analyze and identify the phase(s) present in each element.

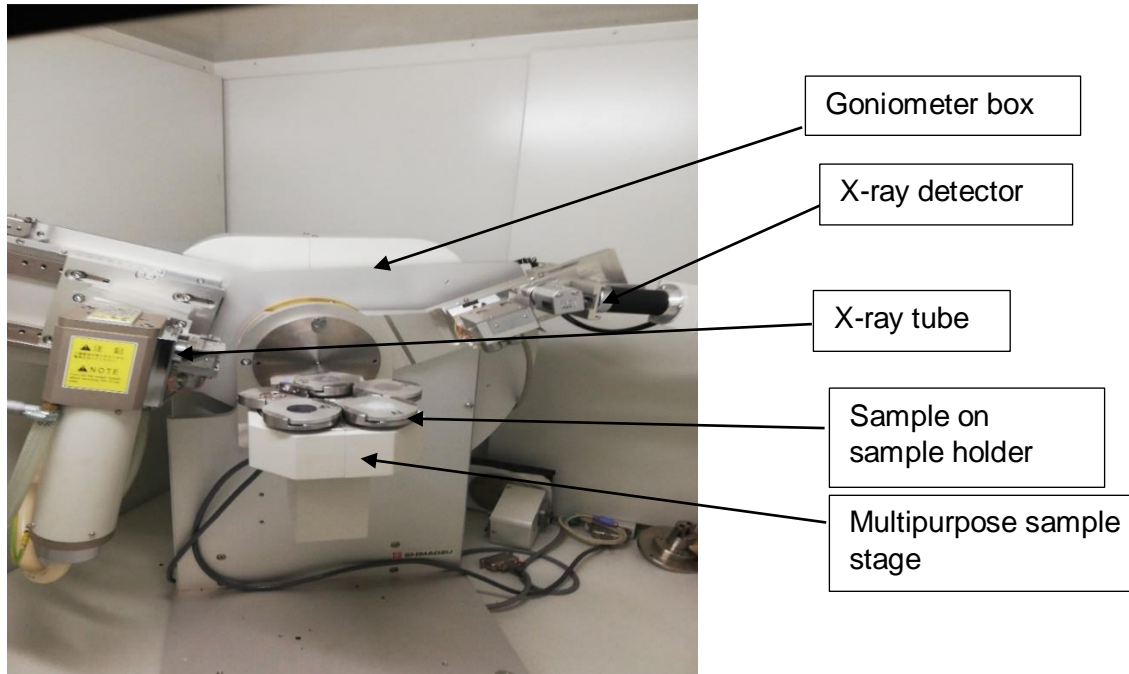


Fig. 3.3 X-ray diffraction machine PANalytical

3.2.2 MILLING OF $\text{Al}_{20}\text{Be}_{20}\text{Fe}_{10}\text{Si}_{15}\text{Ti}_{35}$ IN WET AND DRY CONDITIONS

Al 20% by wt, Be 20% by wt, Fe 10% by wt, Si 15% by wt, and Ti 35% by wt elemental powders with high purity ($\geq 99.9\%$) were weighed according to their weight percent. High energy planetary ball mill containing stainless steel balls was used to mill the weighed powders in a high purified argon-protected environment to avoid excess oxidation. This was carried out in the milling machine as depicted in figure 3.4 below in wet and dry conditions.

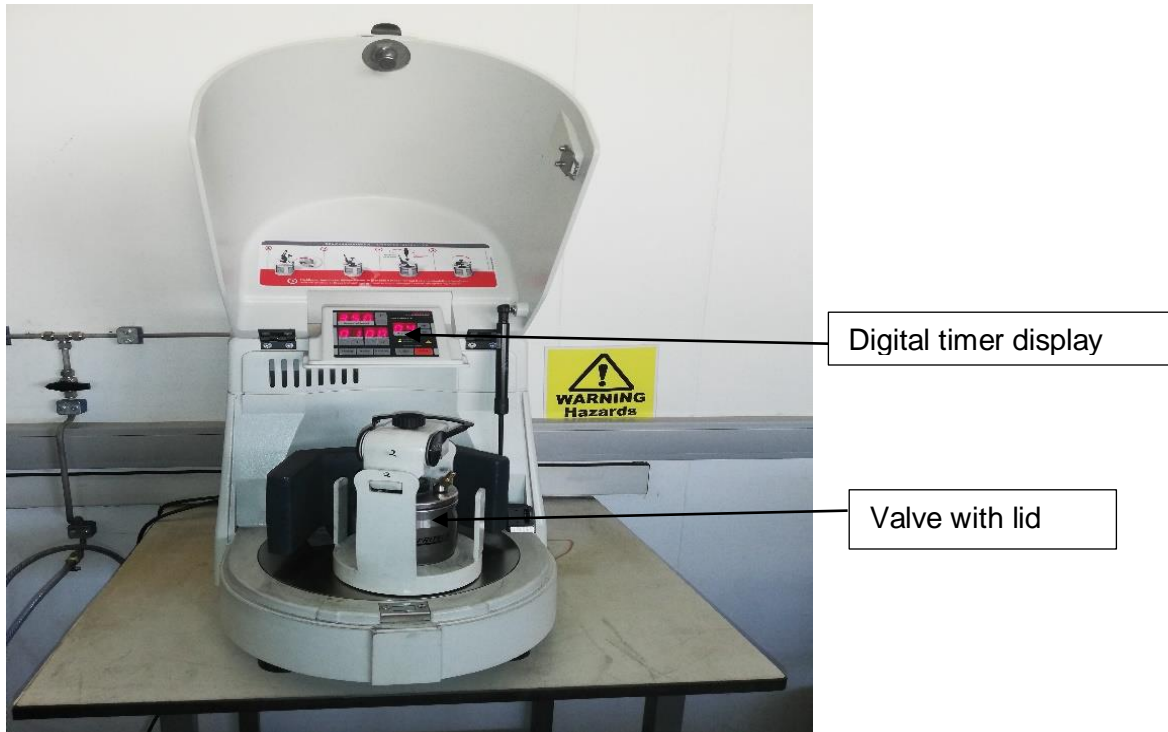


Fig. 3.4 A schematic representation of the milling machine used for the milling process

To calculate the volume of each sample to be sintered, the diameter, radius, height and the total number of samples to be sintered needed to be decided at this point. Four (4) samples with dimensions stated in table 3.1 were intended to be used for sintering, hence this needed to be incorporated during alloy mixture calculation for milling.

Table 3.1 summary of the calculation of the volume for each sample to be sintered

Volume (cm)	$\pi r^2 h$
Diameter	3
Radius	1.5
Height	0.5
π	3.142857143
Volume(cm³)	3.536

Table 3.2 the summary in part, of the variables to be considered in calculating the total mass to be weighed.

Element	Molecular weight	Atomic percent (%)	P Value	wt%/100
Al	26.982	20	539.640	0.160
Be	9.012	20	180.240	0.053
Fe	55.845	10	558.450	0.165
Si	28.086	15	421.290	0.125
Ti	47.867	35	1675.345	0.496
Total		100	3374.965	1

$P \text{ Value} = \text{Molecular weight} \times \text{Atomic percent}$

$$\text{wt\%/100} = \frac{P \text{ Value}}{P \text{ Value total}}$$

Table 3.3 the summary of the rest of the variables to be considered in calculating the total mass to be weighed.

Element	Density (g/cm ³)	wt%/density	Individual mass (g)	Individual mass + 10% Loss (g)	Mass to be weighed (g)
Al	2.700	0.059	2.070	2.277	9.109
Be	1.850	0.028	0.691	0.760	3.042
Fe	7.870	0.021	2.142	2.357	9.426
Si	2.320	0.053	1.616	1.778	7.111
Ti	4.506	0.110	6.427	7.069	28.279
Total		0.271	12.946	14.241	56.967

$$\text{Wt\%/density} = \left[\frac{\text{wt\%}}{100} \div \text{Density} \right]$$

$$\text{Individual mass (g)} = [\text{wt\%/100}] \times [\text{theoretical mass 'm}\tau'12.946]$$

$$\text{Mass to be weighed} = [\text{Individual mass} + 10\% \text{Loss (g)}] \times [\text{four(4)samples}]$$

$$* \text{Losses} = [\text{theoretical mass 'm}\tau'12.946] \times [10\%] = 1.294$$

Table 3.4 the summary of conditions and parameters used for the milling process.

CONDITION	PCA	BPR	MILLING DURATION	MILLING SPEED
Wet milling	Ethanol	3 : 1	24 hrs	300 rpm
Dry milling	Stearic acid	3 : 1	14 hrs	300 rpm

3.2.2.1 Dry-milling of $\text{Al}_{20}\text{Be}_{20}\text{Fe}_{10}\text{Si}_{15}\text{Ti}_{35}$ Alloy

Six weight percent (6wt%) stearic acid was used as PCA during the dry milling process, and this is calculated using the formula below:

Where ' $\rho\tau$ ' means theoretical density, ' ρ ' is $\frac{1}{\text{sum of (wt\%/density)}}$ = $1/0.273083336 = 3.66188$, ' ρ stearic acid' means density of stearic acid which is 0.9408 g/cm^3

$$\rho\tau = \frac{1}{(94\text{wt\%}/\rho) + (6\text{wt\%Stearic acid}/\rho\text{Stearic acid})}$$

$$\rho = \frac{1}{(0.94/3.66188) + (0.06/0.9408)}$$

$$\rho = 3.12037$$

$$' \rho\tau ' \times ' \text{proposed volume of disc} ' = 3.120375 \times 3.535714$$

$$= 11.03277$$

$$94\% = \frac{98}{100} \times 11.03277 = 10.3708038g$$

6wt% of stearic acid is $11.03277 - 10.3708038 = 0.662g$ of stearic acid was added to the alloy powder mix.

The calculated quantity of stearic acid was added to the total 'mass to be weighed' from table 3.4, as PCA before milling was done.

3.2.2.2 Wet-milling of $Al_{20}Be_{20}Fe_{10}Si_{15}Ti_{35}$ Alloy

Methanol was added to the total 'mass to be weighed' on table three before milling. The wet-milled alloy powder was dried in a rotary vapor machine at 40°C as shown below;

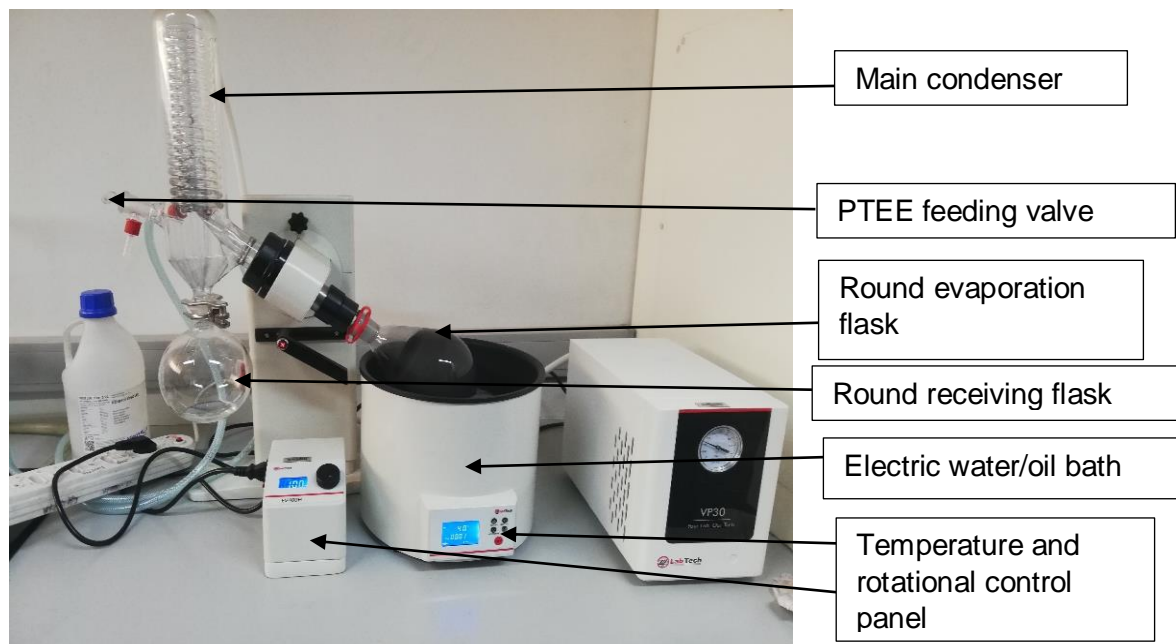


Fig. 3.5 the drying process of wet-milled alloy in the rotary vapor drying machine.

3.2.3 SINTERING OF WET-MILLED AND DRY-MILLED $\text{Al}_{20}\text{Be}_{20}\text{Fe}_{10}\text{Si}_{15}\text{Ti}_{35}$ ALLOY

Both dry-milled and wet-milled alloy powder was subjected to sintering process using FCT Systeme GmbH sintering machine shown below;

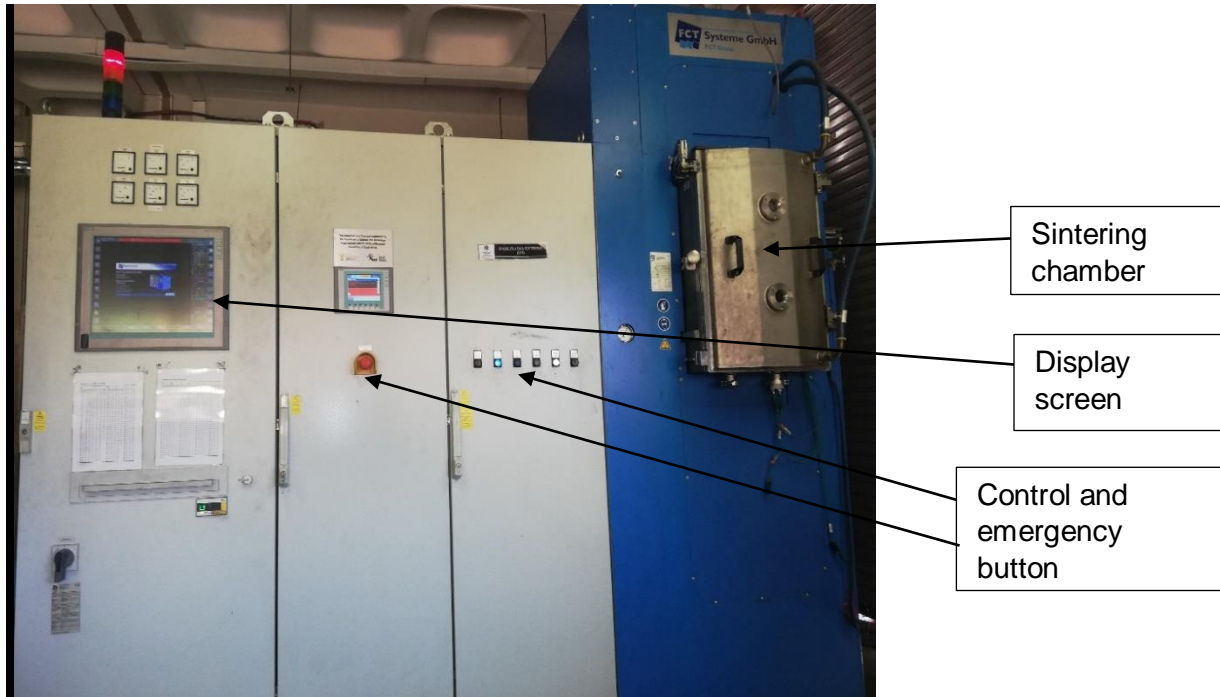


Fig. 3.6 FCT Systeme GmbH sintering machine used

3.2.3.1 Sintering Temperature Calculation

Table five below summarizes the variables needed to calculate the temperature at which sintering of the alloy powder will be carried out.

$$T_m = \sum_{i=1}^n C_i (T_m)_i$$

Table 3.5 summary of the variables needed to calculate the temperature at which sintering of the alloy powder will be carried out.

Element	Mole fraction	%	T_m	
Al	0.20		660.3	132.06

Be	0.20	1287.0	257.40
Fe	0.10	1538.0	153.80
Si	0.15	1414.0	212.10
Ti	0.35	1668.0	583.80
			1339.16

$$0.7T_m = 937,41^{\circ}\text{C}$$

$$0.8T_m = 1071.328^{\circ}\text{C}$$

3.2.3.2 Sintering of Wet-milled $\text{Al}_{20}\text{Be}_{20}\text{Fe}_{10}\text{Si}_{15}\text{Ti}_{35}$ Alloy

Table 3.6 below summarizes the parameters attempted in conducting the sintering process on wet-milled $\text{Al}_{20}\text{Be}_{20}\text{Fe}_{10}\text{Si}_{15}\text{Ti}_{35}$ alloy but the alloy powder was sublimating out of the punch and die due to reasons yet to be known.

Table 3.6 parameters used to sinter wet-milled alloy

	Parameter	Parameter	Parameter	Cold compaction
	1 st attempt	2 nd attempt	3 rd attempt	4 th attempt
Heating rate	100°C/min	100°C/min	100°C/min	Nil
Sintering Temperature	1071.328°C	937,41°C	500°C	0°C
Pressure	30 MPa	30 MPa	30 MPa	10 MPa
Holding time	4 min	10 min	Nil	Nil

3.2.3.3 Sintering of Dry-milled $Al_{20}Be_{20}Fe_{10}Si_{15}Ti_{35}$ Alloy

Table 3.7 below summarizes the parameters attempted in conducting the sintering process on dry-milled $Al_{20}Be_{20}Fe_{10}Si_{15}Ti_{35}$ alloy. Although some of the powder sublimated out of the die just like the wet-milled alloy powder did hence, the alloy powder was not able to be compacted. The powder was able to be heated up to $\sim 200^{\circ}C$ before some alloy powder sublimate was found out of the punch and die due to reasons yet to be known while the sintering equipment tripped off.

Table 3.7 parameters used to sinter dry-milled alloy

	Parameter
	1 st trial
Heating rate	100°C/min
Sintering Temperature	500°C
Pressure	30 MPa
Holding time	4 min

3.2.4 TGA/DSC ANALYSIS OF DRY AND WET-MILLED $Al_{20}Be_{20}Fe_{10}Si_{15}Ti_{35}$ ALLOY POWDERS

To understand what may be responsible for premature sublimation of alloy powders out of punch and die during the sintering process, a thermo-analytical process was conducted on both dry-milled and wet-milled powder. This is necessary because it will help to understand and study the alloy thermal expansion and thermal stability behavior at a temperature around $250^{\circ}C$. About 10.089 mg of each dry and wet milled $Al_{20}Be_{20}Fe_{10}Si_{15}Ti_{35}$ alloy powder was examined using STA7200RV TGA/DSC thermal analysis equipment, under the condition of nitrogen gas. Table 3.8 below summarizes the parameters used in carrying out the TGA/DSC analysis on both dry and wet-milled alloy samples.

Table 3.8 parameters used for the TGA/DSC thermal analysis(dry and wet)

Start (°C)	Limit (°C)	Rate (°C/min)	Hold (min)	Sampling (s)
25	150	5	30	0.5
150	200	5	30	0.5
200	250	5	30	0.5
250	300	5	30	0.5
300	900	10	1	0.5

Dry and wet-milled samples were weighed each using a weighing scale in the ceramic pan and were loaded into the TGA/DSC instrument auto-sampler as shown in figure 3.7(B) below. The analysis was conducted under nitrogen inert gas conditions to avoid the sample reacting with oxygen from the air. This was carried out at a temperature ranging from 25°C to 900°C for 4 hours, the analysis was held at a temperature of 150°C, 200°C, 250°C, and 300°C each for 30 minutes increased at 5°C/min on each interval. The alloy powder samples were held at the above-mentioned temperatures because the alloy powders were suspected to have reacted negatively and sublimated out of the die during the sintering process around those temperatures. From 300°C, the temperature was increased rapidly to 900°C at 10°C/min and the result was recorded.



Fig. 3.7 shows TGA/DSC equipment set up (A) STA7200RV TGA/DSC and (B) auto-sampler.

4.0 RESULTS AND DISCUSSION

4.1 Al, Be, Fe, Si & Ti As-received Particle Size Analysis (PSD) Results

The graphs below show the average particle size distribution analysis for the individual elemental components.

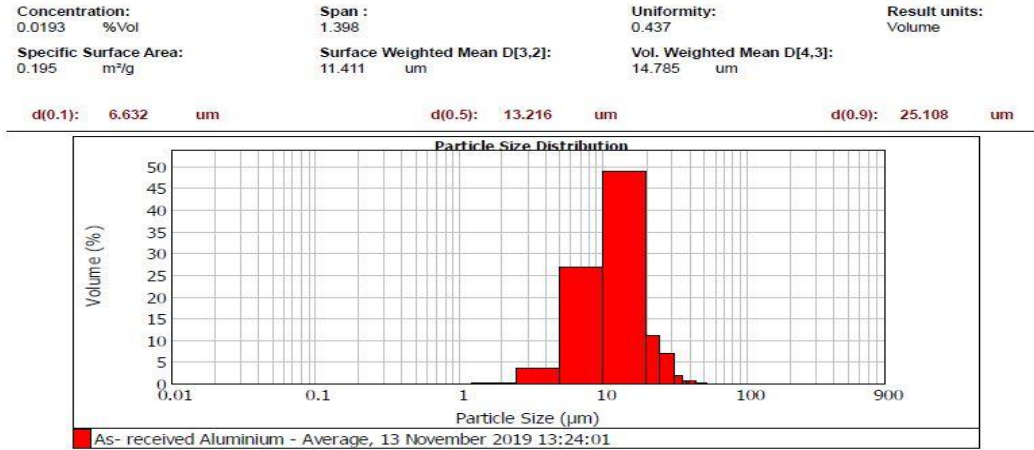


Fig. 4.1: Graph of the average particle size distribution of Al powder

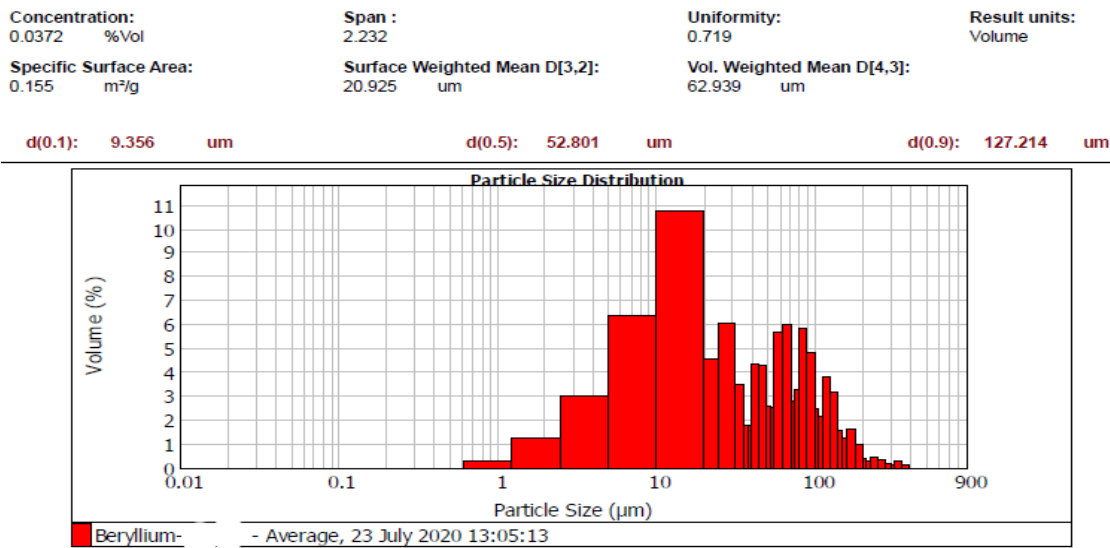


Fig. 4.2: Graph of the average particle size distribution of Be powder

Concentration: 0.0192 %Vol	Span : 2.168	Uniformity: 0.694	Result units: Volume
Specific Surface Area: 0.113 m ² /g	Surface Weighted Mean D[3,2]: 6.747 um	Vol. Weighted Mean D[4,3]: 11.279 um	
d(0.1): 3.618 um	d(0.5): 8.546 um	d(0.9): 22.147 um	

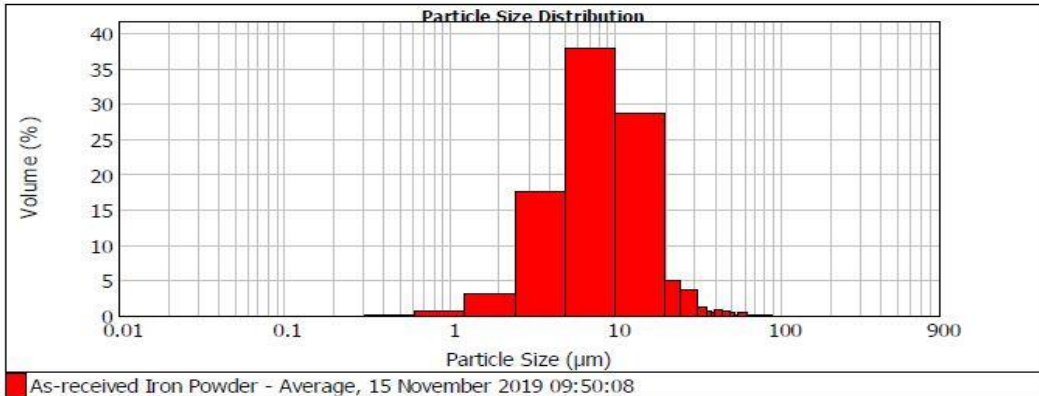


Fig. 4.3: Graph of the average particle size distribution of Fe powder

Concentration: 0.0038 %Vol	Span : 3.024	Uniformity: 0.957	Result units: Volume
Specific Surface Area: 1.99 m ² /g	Surface Weighted Mean D[3,2]: 3.019 um	Vol. Weighted Mean D[4,3]: 7.964 um	
d(0.1): 1.330 um	d(0.5): 5.457 um	d(0.9): 17.834 um	

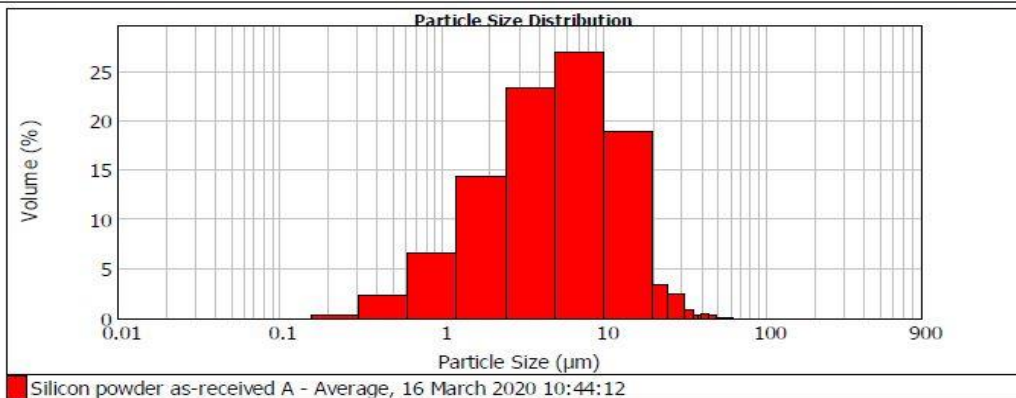


Fig. 4.4: Graph of the average particle size distribution of Si powder

Concentration: 0.0449 %Vol
 Span : 1.529
 Uniformity: 0.473
 Result units: Volume
 Specific Surface Area: 0.0456 m²/g
 Surface Weighted Mean D[3,2]: 29.159 um
 Vol. Weighted Mean D[4,3]: 43.257 um
 d(0.1): 16.334 um
 d(0.5): 39.186 um
 d(0.9): 76.257 um

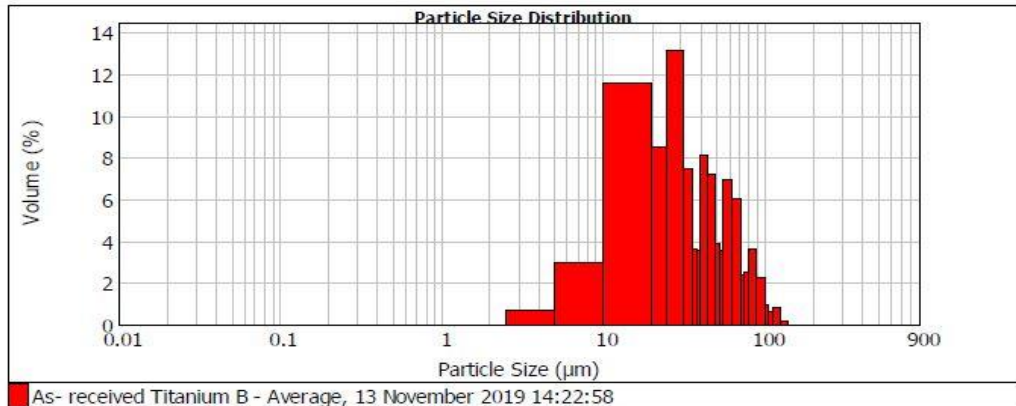


Fig. 4.5: Graph of the average particle size distribution of Ti powder

The table below shows the summary of the starting particle size of the individual element.

Table 4.1 starting particle size distribution of elemental powders (PSD)

	Al	Be	Fe	Si	Ti
d(0.1)	6.63µm	9.35µm	3.61µm	1.33µm	16.33µm
d(0.5)	13.21µm	52.80µm	8.54µm	5.45µm	39.18µm

According to the starting particle size history summarized in table 4.1 above, the as-received powder particle reveals that Si has the finest starting particle size ranging between 1.33µm and 5.45µm. Fifty percent of Be as-received powder was from 52.80µm and below, while only ten percent falls below 9.35µm. Although, Be powder has one of the most coarse starting particle size among other elemental powders. Ti is also known for its hard, granular, and coarse nature, hence fifty percent of its particles are from 39.18µm and below. This shows that both Be and Ti have the most coarse starting particle size before milling.

4.2 Al, Be, Fe, Si and Ti As-received SEM Micrographs

The microstructure of each element was examined in as-received form after PSD analysis.

The SEM images of as-received individual powders were taken at specific magnification as shown in the figures below;

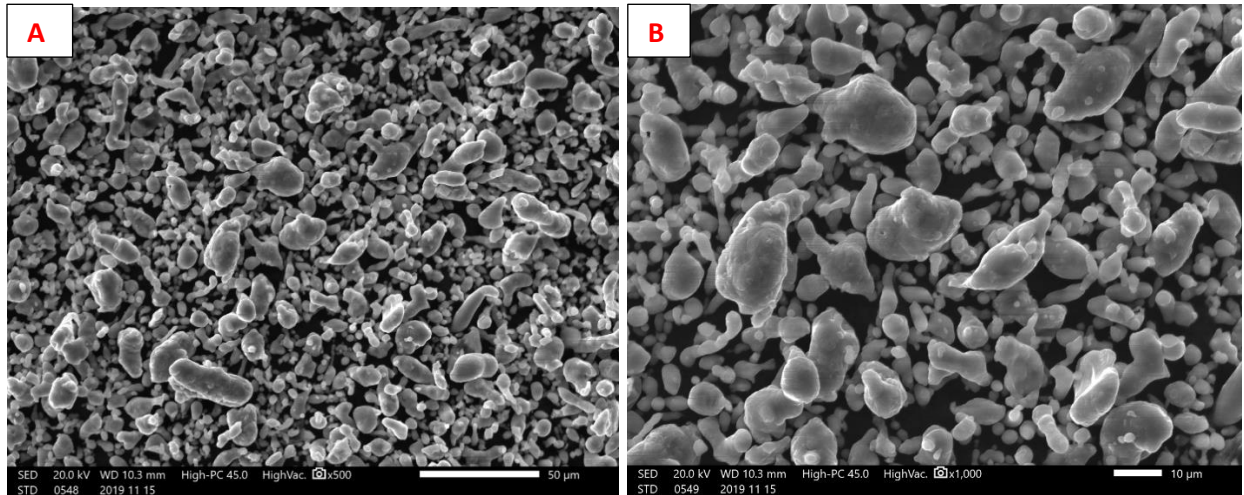


Fig. 4.6: SEM of as-received Al powder (A) x500 and (B) x1000

As-received Al powder has a flake-shape and some round disk shape particles with many large grains having an average grain size of (6-13.5 µm) as displayed by SEM images in Fig. 4.6 (A & B) above.

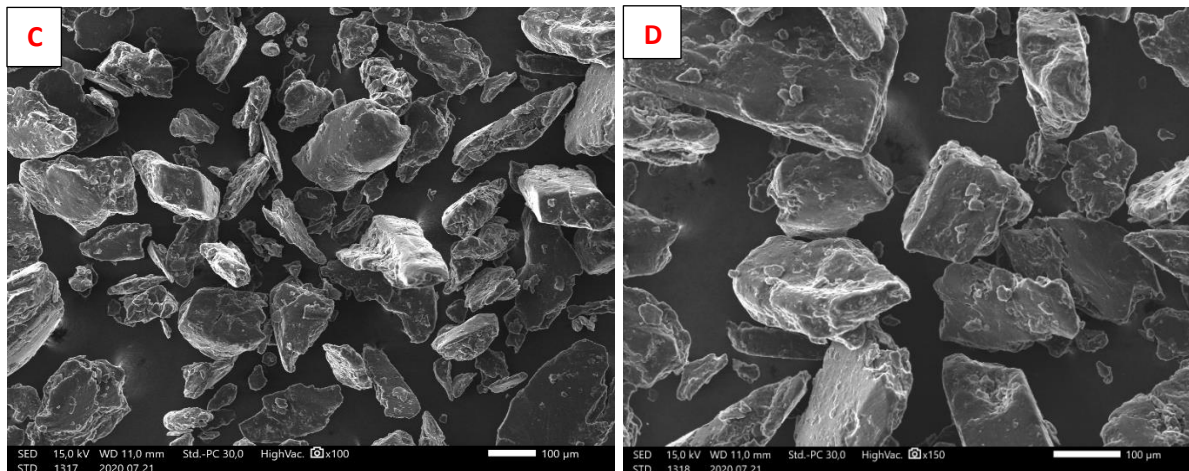


Fig. 4.7: SEM of as-received Be powder (C) x100 and (D) x150

As-received Be powder consisted of compact particles of irregular block shape with an average grain size of 52.80 μm as displayed in Fig. 4.7 (C & D) above.

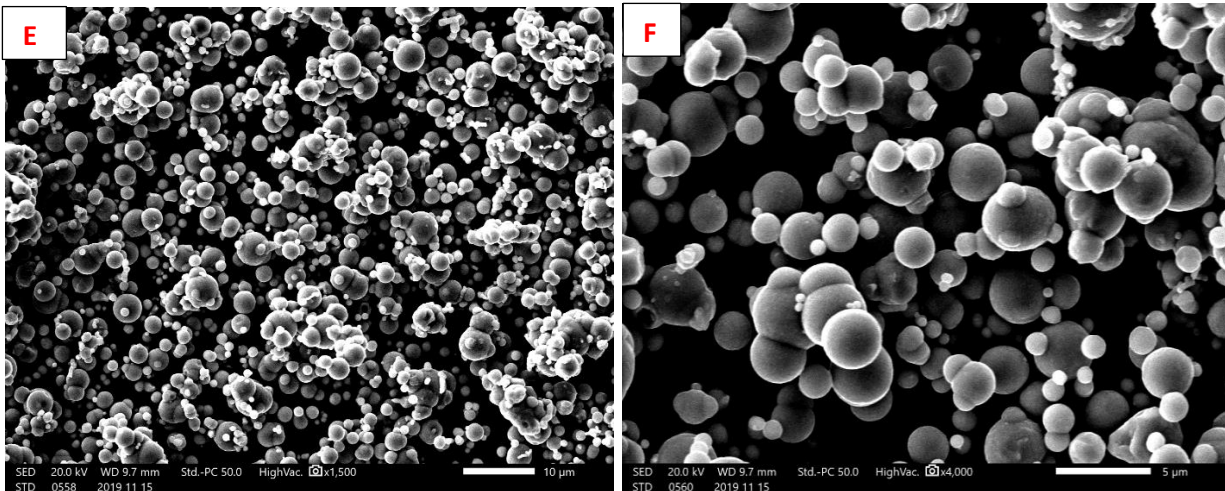


Fig. 4.8 SEM of as-received Fe powder (E) x1500 and (F) x4000

As-received iron powder consisted of spherical shape particles with grain size between 3.61 μm to 8.54 μm forming agglomerate as displayed in Fig. 4.8 (E & F) above.

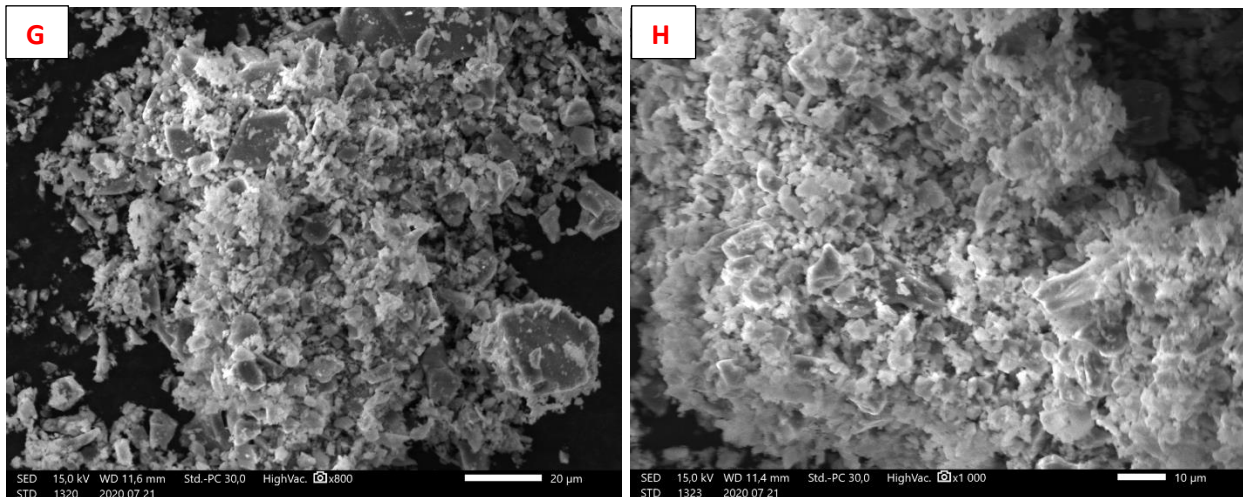


Fig. 4.9 SEM of as-received Si powder (G) x800 and (H) x1000

As-received silicon powder consisted of both octahedral shape and twinned spinel shape with an average grain size of 5.45 μm forming clusters as displayed in Fig. 4.9(G & H) above.

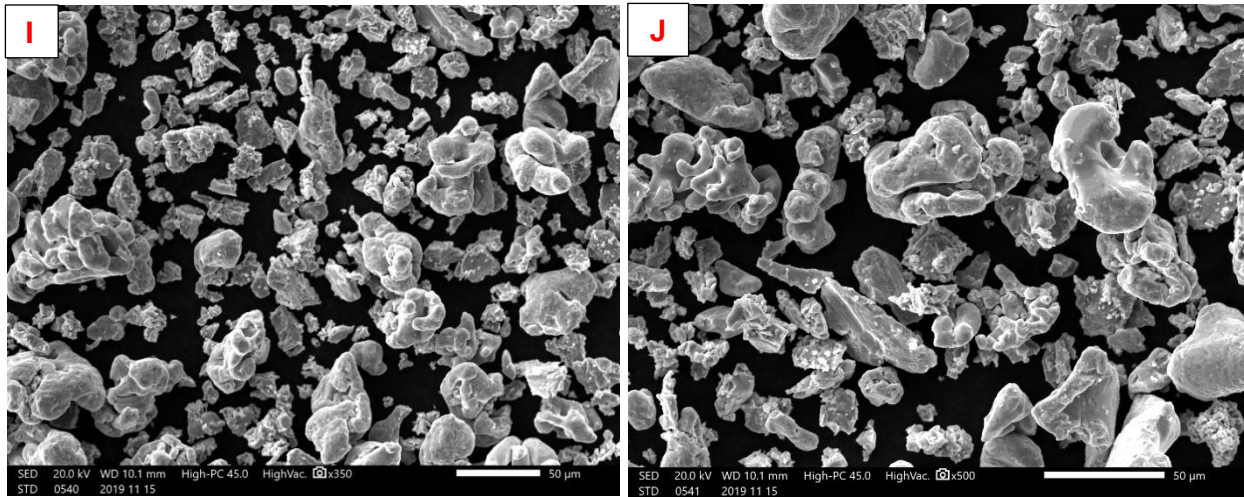


Fig. 4.10 SEM of as-received Ti powder (I) x350 and (J) x500

As-received titanium particles consisted of nearly-spherical morphology possibly composed of alpha phase with closed packed hexagonal structure. The average size of grain was in the range of 16.33 - 39.18 μm .

4.3 XRD Images of Individual As-received Element

Below are the XRD images showing phases present in individual element

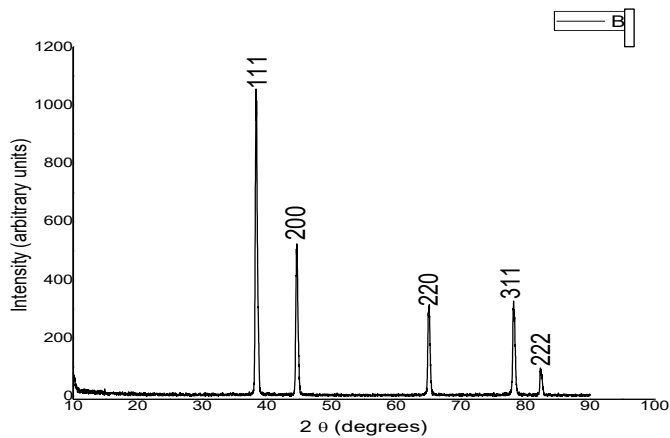


Fig. 4.11 XRD of as-received Al powder

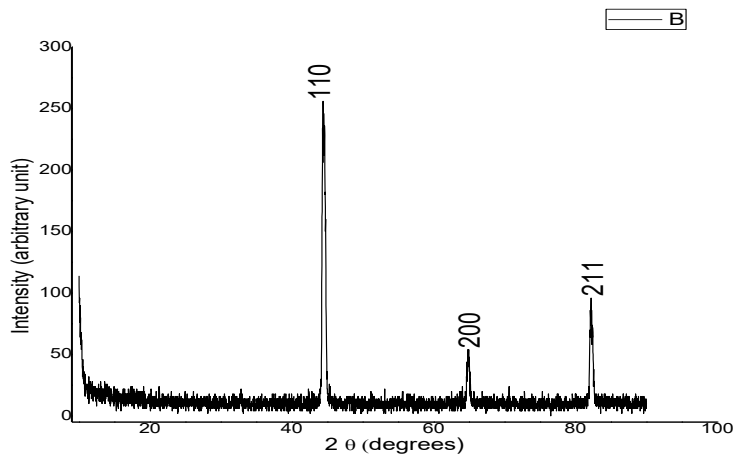


Fig. 4.12 XRD of as-received Fe powder

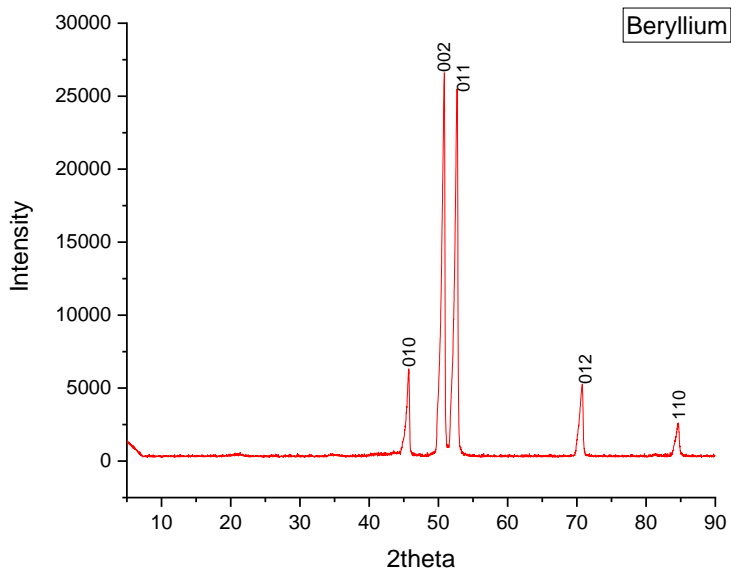


Fig. 4.13 XRD of as-received Be powder

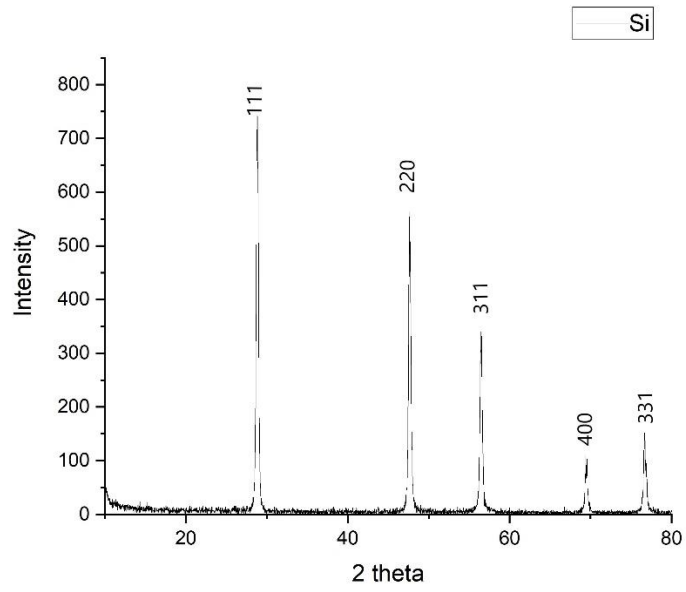


Fig. 4.14 XRD of as-received Si powder

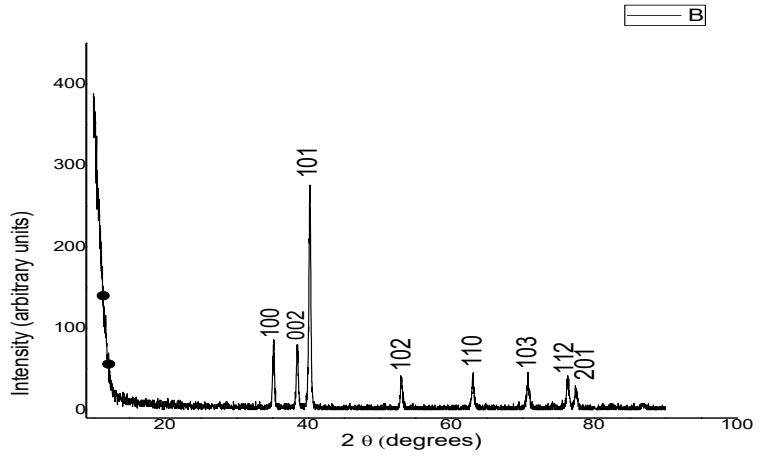


Fig. 4.15 XRD of as-received Ti powder

4.4 Milled $\text{Al}_{20}\text{Be}_{20}\text{Fe}_{10}\text{Si}_{15}\text{Ti}_{35}$ Alloy Powder

4.4.1 SEM Micrographs of Dry-milled $\text{Al}_{20}\text{Be}_{20}\text{Fe}_{10}\text{Si}_{15}\text{Ti}_{35}$ Alloy Powder

Below is the SEM image of the dry-milled alloy powder;

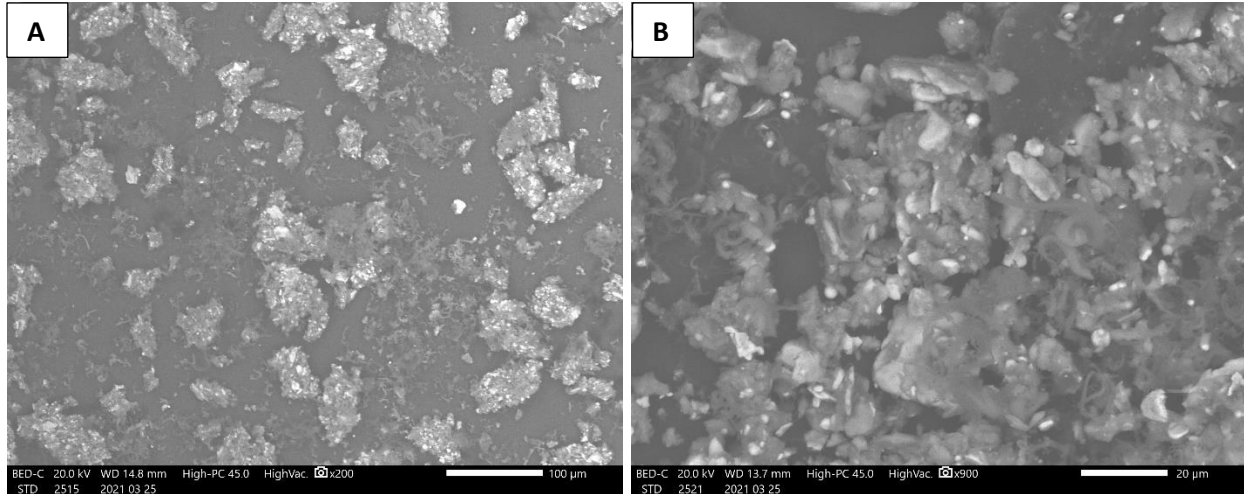


Fig. 4.16 SEM image of dry-milled alloy powder (14hrs) (A) x200 and (B) x900

The dry-milled $\text{Al}_{20}\text{Be}_{20}\text{Fe}_{10}\text{Si}_{15}\text{Ti}_{35}$ alloy sample revealed irregular shapes of microns.

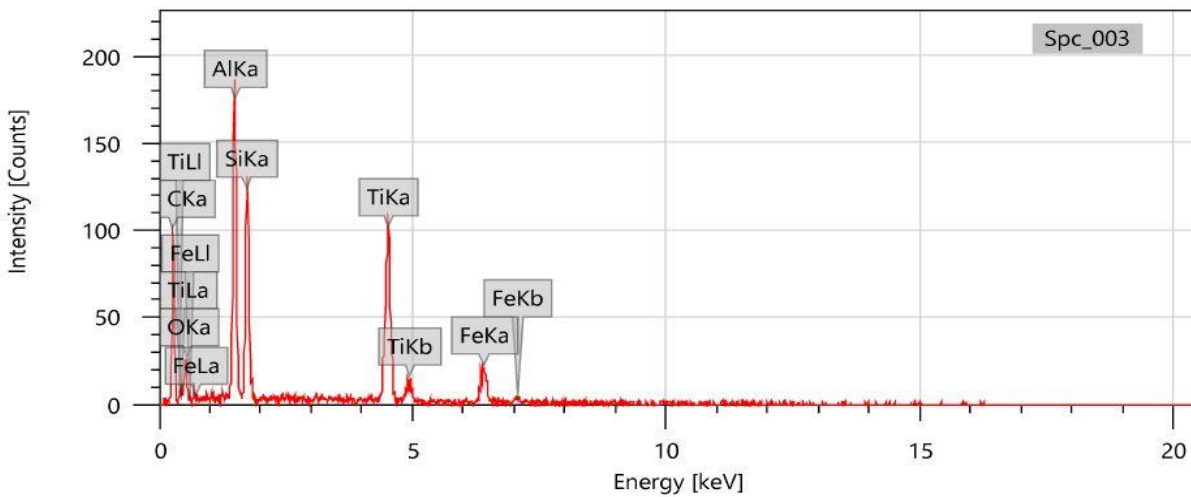


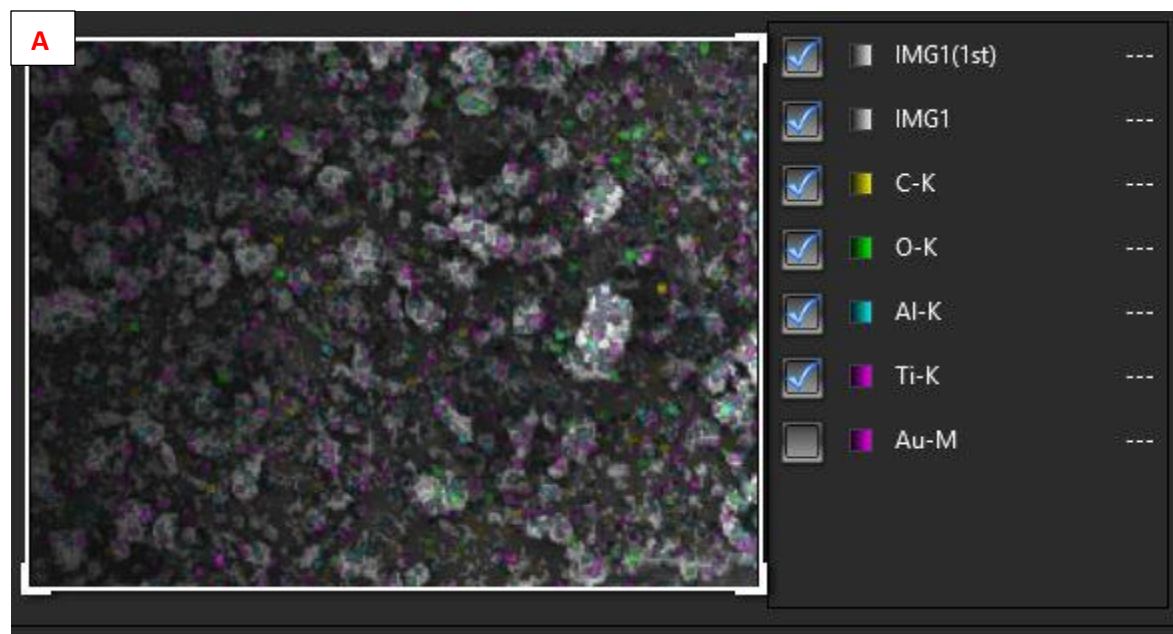
Fig. 4.17 EDS image analysis of the dry-milled alloy powder

The table below shows the analysis of the element composition present in the dry-milled alloy powder according to the above EDS image analysis.

Table 4.2 percentage by mass and atom of the individual component element in the dry-milled alloy powder

Element	Line	Mass%	Atom%
C	K	43.04±0.78	63.46±1.15
O	K	14.49±0.96	16.04±1.07
Al	K	10.64±0.35	6.99±0.23
Si	K	8.16±0.32	5.15±0.20
Ti	K	16.46±0.51	6.08±0.19
Fe	K	7.21±0.45	2.29±0.14
Total		100.00	100.00
Spc_003			Fitting ratio 0.1061

C and O content seems to be high in the dry-milled alloy, possibly due to contamination. Be is totally absent in the alloy mix while the atomic percentage and mass percentage shows little or no presence of Fe according to the result. EDS mapping of the individual element was carried out on the dry-milled sample which also confirmed little or no presence of Be, Fe, and also Si as shown in the figure below.



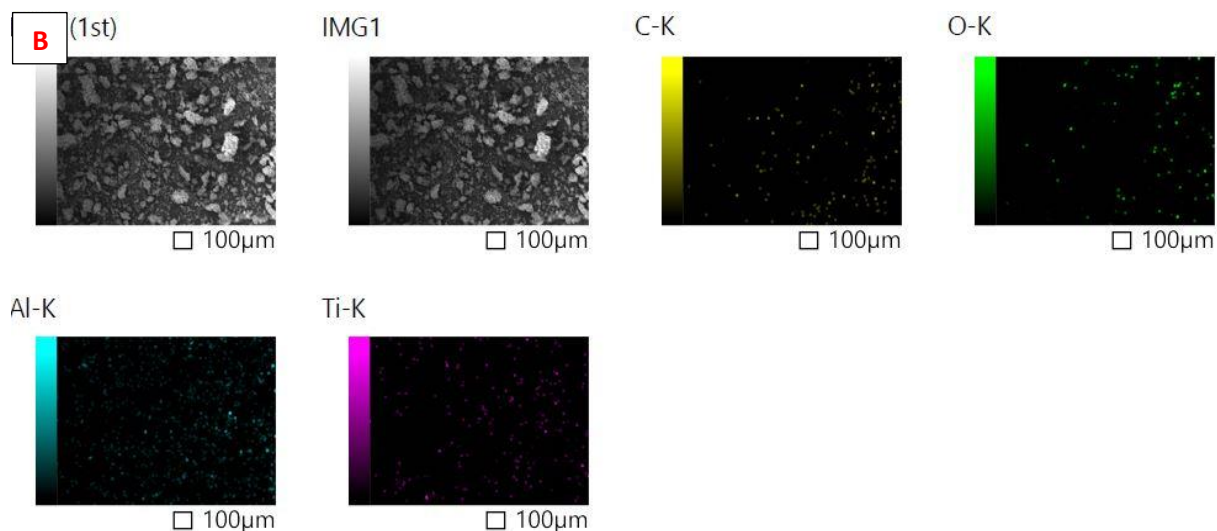


Fig. 4.18 (A) and (B) are the EDS mapping of the individual element in a dry-milled alloy sample

High C and O content present in the EDS and EDS mapping results as shown in table 4.2 and Fig. 4.18 above respectively could be as a result of contamination. O might have found its way into the alloy mixture when handling the alloy powders and during processing line which is almost impossible to avoid. However, Be is totally absent in both EDS's while atomic percentage and mass percentage of Fe (especially) is very low as revealed by the EDS which is also in line with the EDS mapping result.

Different reasons could be speculated as reasons for absence of Be and Fe in relation to high O content at this point until further characterization such as XRD is carried out to establish the chemistry behind this. Be is expected to react with O from stearic acid (C & O) during milling at low temperature to form BeO (during dry milling) because Be is one of the few elements that are more reactive to oxygen than Mg. The higher the weight percent of Be added to Al base alloy, the more BeO forms (Houska, 1988). The presence of Al₂O₃ or O must have helped to increase the solubility of Be to form BeO (Burr et al., 2016). Also, Be might be too light to be picked up during EDS, hence, a high percentage of O as shown by the EDS could account for the quantitative loss in Be which might have formed BeO appearing as O. From another angle, absence of Be, Fe and Si in the EDS's results were suspected to have been as a result of formation of atomic pairs formed

among these missing elements. This is assumed because Be, Al, Si and Fe have strong bonding with Ti to form pairs according to Tseng et al. (2018), hence the XRD results will give more clarification on this assumption in the later stage.

4.4.2 SEM Micrographs of Wet-milled $\text{Al}_{20}\text{Be}_{20}\text{Fe}_{10}\text{Si}_{15}\text{Ti}_{35}$ Alloy Powder

Below is the SEM image of the wet-milled alloy powder after drying in a rotary vapour dryer.

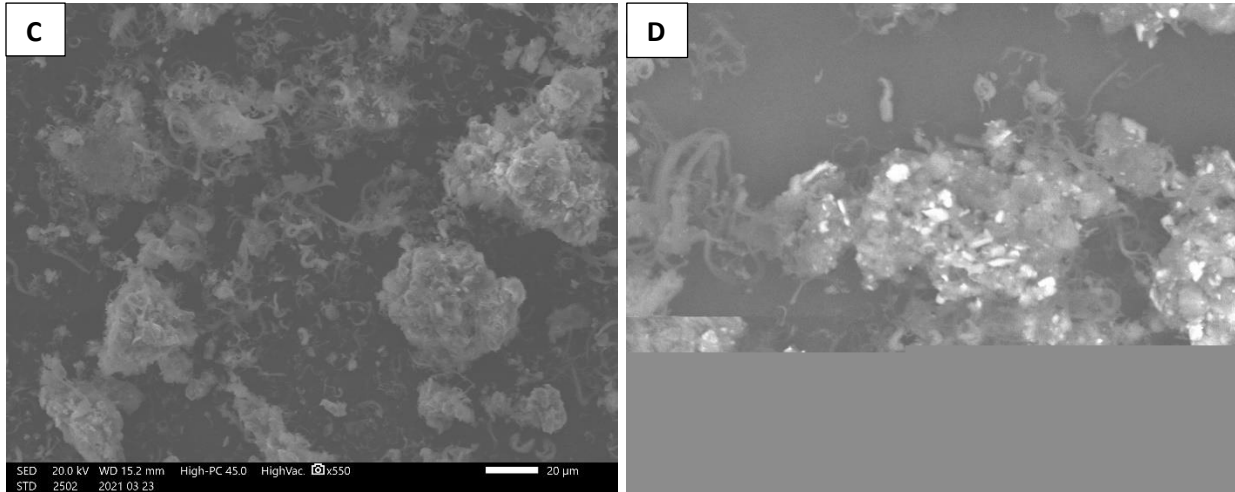


Fig. 4.19 SEM image of wet-milled alloy powder (24hrs) (C) x550 and (D) x900

The wet-milled $\text{Al}_{20}\text{Be}_{20}\text{Fe}_{10}\text{Si}_{15}\text{Ti}_{35}$ alloy sample shows watery amorphous and round micron particles with fiber structure.

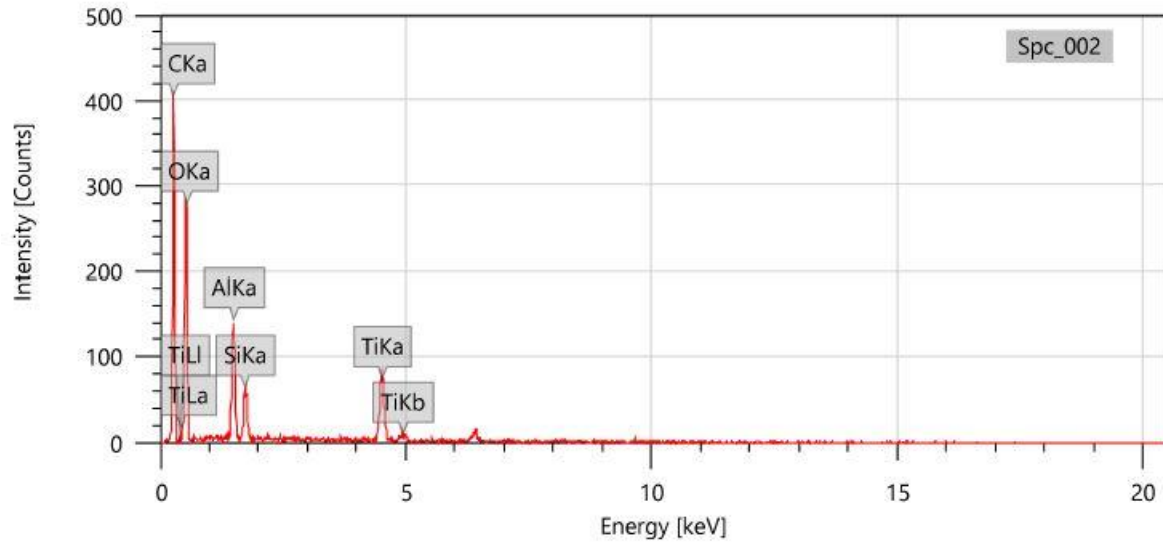


Fig. 4.20 EDS image analysis of the wet-milled alloy powder

The table below shows the analysis of the individual component element present in the wet-milled alloy powder according to the above EDS image analysis.

Table 4.3 Percentage by mass and atom of the individual component element in the wet-milled alloy powder.

Element	Line	Mass%	Atom%
C	K	41.65±0.39	51.55±0.48
O	K	46.91±0.92	43.58±0.85
Al	K	3.95±0.15	2.18±0.08
Si	K	1.69±0.10	0.89±0.05
Ti	K	5.80±0.21	1.80±0.07
Total		100.00	100.00
Spc_002		Fitting ratio 0.0799	

The C content seems to be high as well as O content in the wet-milled alloy, possibly due to contamination. Be is also absent in the alloy mix according to the analysis possibly due to formation of binary or ternary intermetallic pairs with Fe from Be precipitates. EDS mapping of the individual element was also carried out on the wet-milled sample and shows no traces of Be and Fe as shown in the figure below. Hence, the presence of high C and O contents was confirmed.

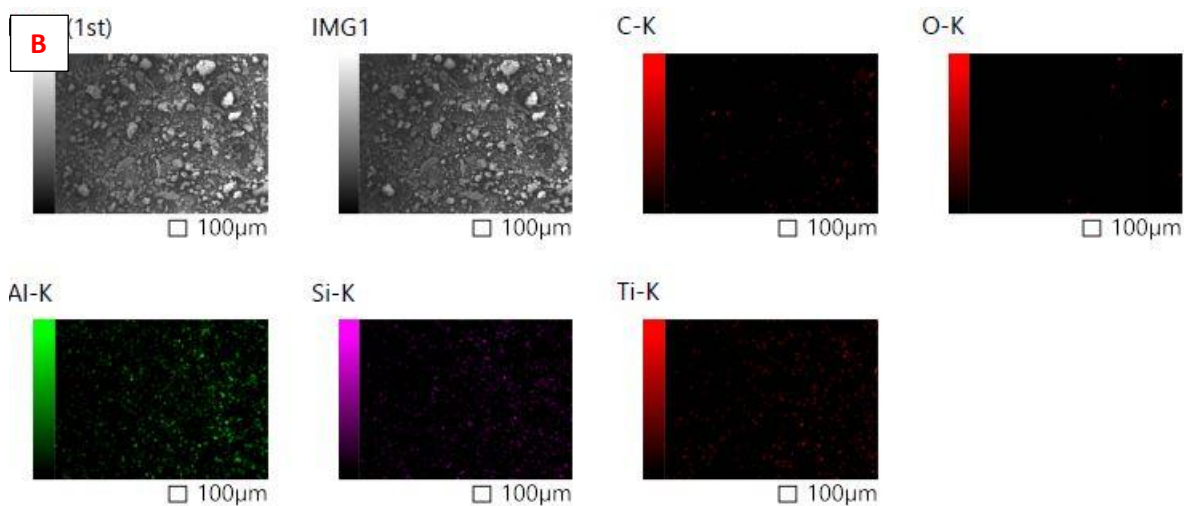
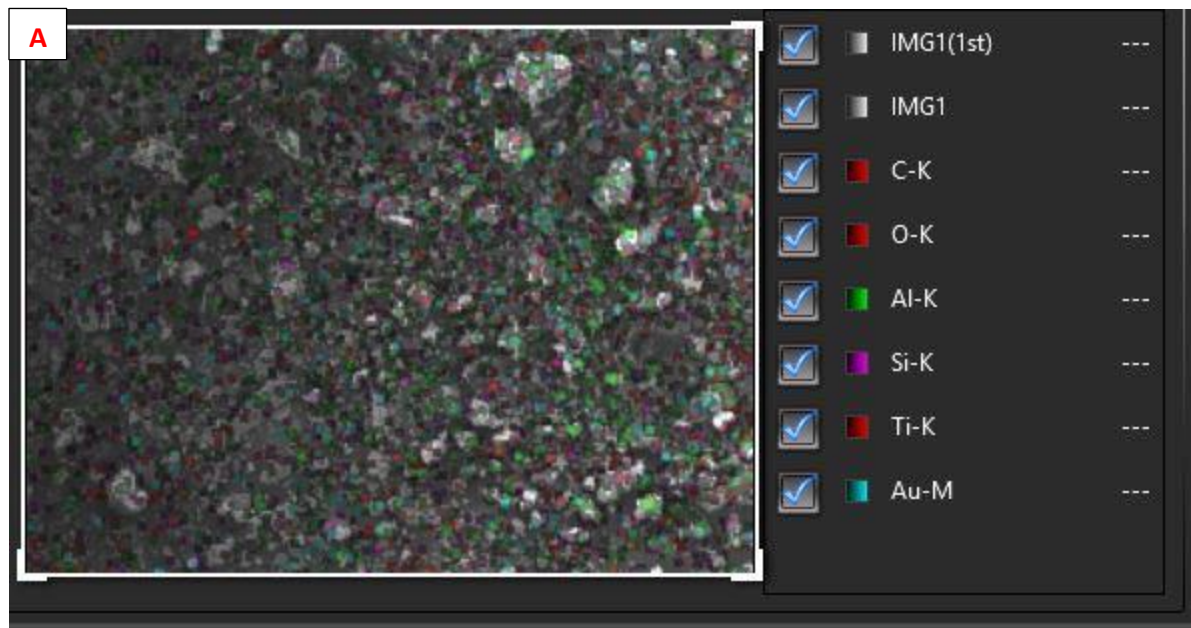


Fig. 4.21 (A) and (B) are the EDS mapping of the individual element in a wet-milled alloy sample

Absence of Be and Fe in the wet-milled alloy as shown in the EDS's results in table 4.3 and Fig. 4.21 above might be confirming formation of Be-Fe pair from precipitates. This is possible because, most impurity concentrations in commercial beryllium do exceeds the solubility limit and produce precipitates. The precipitates that form generally are present as both binary and ternary intermetallic phases with Be. Beryllium forms intermetallic compounds with a series of metals like Fe, Al or Ti. Therefore, Be is

suspected to have form binary intermetallic phase with Fe present in $\text{Al}_{20}\text{Be}_{20}\text{Fe}_{10}\text{Si}_{15}\text{Ti}_{35}$ alloy powder. The primary crystals of Be–Fe compounds are formed at the liquidus temperature. A large amount of Ti is likely to be found in the core of the block Be–Fe phase. It is suggested that Be–Fe phases were formed by a peritectic reaction with Al_3Ti or another titanium-rich particle according to Wang and Xiong (2000). Be–Fe particles might have acted as the nuclei of $\alpha\text{-Al}$, therefore most of the Be–Fe phases might be located inside the $\alpha\text{-Al}$ (Wang and Xiong, 2000).

Perhaps, the presence of Al in the EDS's results of both wet and dry-milled could be associated with presence of a disordered Al bearing phase, where Al substitutes for Fe in FeBe_5 , producing $(\text{Al,Fe})\text{Be}_5$ as reported by Rooksby (1962). Al could also substitute for Fe in FeBe_2 , forming $(\text{Al,Fe})\text{Be}_2$ (Rooksby, 1962). In both cases, the ternary compounds retain the lattice symmetry of their parent structures. Hence, this might account for the absence of Be and Fe in the result. The XRD below is expected to clarify this.

4.5 XRD of Milled $\text{Al}_{20}\text{Be}_{20}\text{Fe}_{10}\text{Si}_{15}\text{Ti}_{35}$ Alloy Powder

Below is the XRD image analysis of both dry-milled and wet-milled alloy powder.

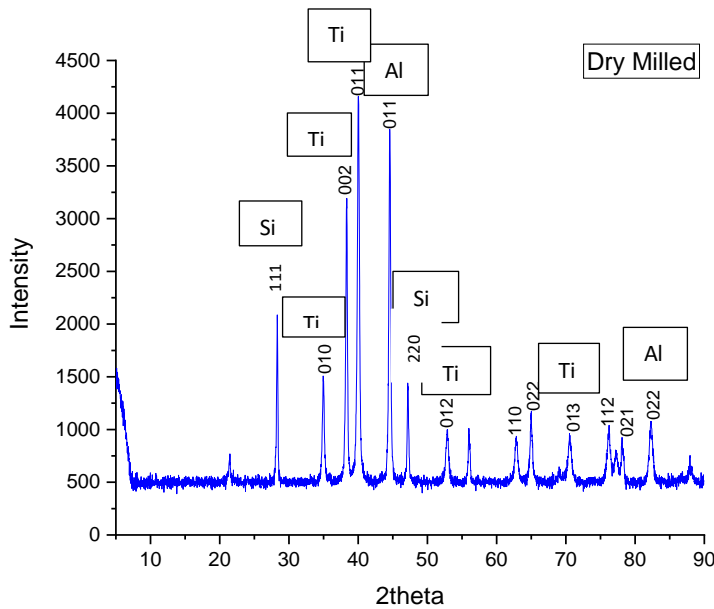


Fig. 4.22 XRD of dry-milled alloy powder

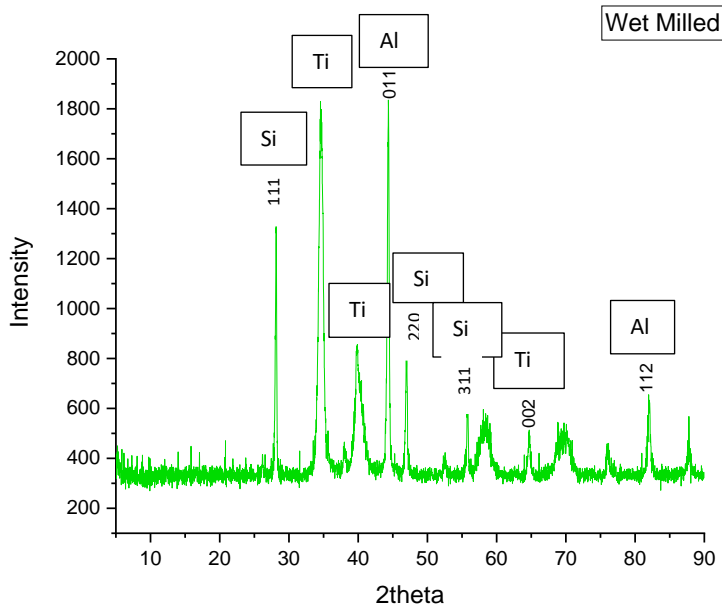


Fig. 4.23 XRD of wet-milled alloy powder

XRD images of dry and wet milled alloy as represented in Fig. 4.22 and Fig. 4.23 respectively does not reveal presence of Be and Fe which is in line with the EDS's result of both wet and dry milled alloy. This shows that Be–Fe particles might have acted as the nuclei of α -Al, therefore most of the Be–Fe phases might be located inside the α -Al. Hence, this confirmed presence of binary Be-Fe intermetallic phase in both wet and dry milled alloy mix. Considering the presence of binary Be-Fe intermetallic in the alloy mix, there is need to calculate the enthalpy of formation from a standard state of suspected phase under consideration in order to analyze the stability of the phase formed. This can be calculated as $\text{Fe} + x\text{Be} \rightarrow \text{FeBe}_x$. Equation (5) represents the solution enthalpy of Fe into Be metal, for comparison.





In the equations above, it should be noted that all phases exhibit favourable (negative) formation enthalpies, and these are lower than the enthalpy of solution in all cases. To further clarify the relative intermetallics stability, the normalized formation enthalpies are plotted against composition to form a convex hull diagram as represented in Fig. 4.24 below.

The below figure will be a guide in determining the phases that are expected to form with increasing Fe content.

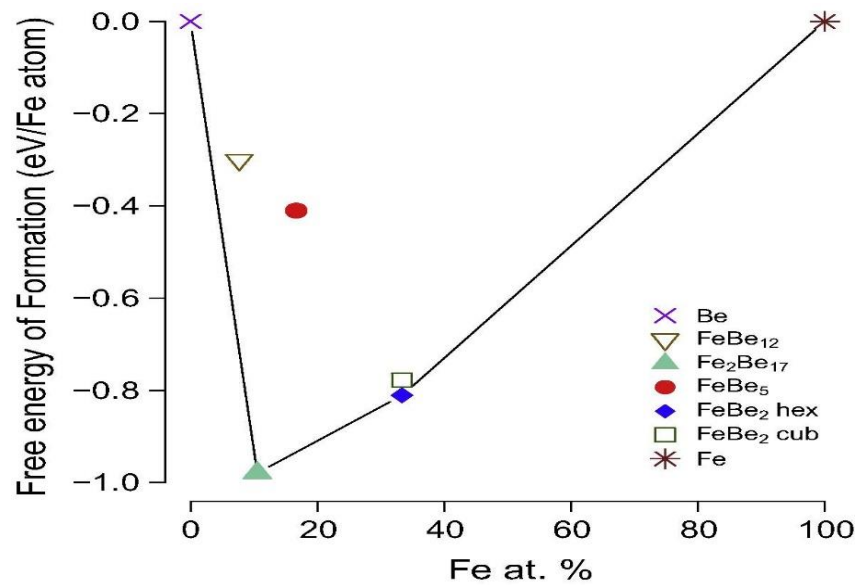


Fig. 4.24 change in formation enthalpy with increasing Fe content. The convex hull is represented by the line and determines phases that could form.

From Fig. 4.24 above, the points lying on the hull identify the phases that are observed at that particular composition. Hence, the distance from the convex hull indicates the degree of instability of the phase. Although, if excess Fe is present in the alloy, FeBe₂ will be the predominant intermetallic phase observed according to Kadyrzhanov et al. (2013). But the EDS mapping results in Fig. 4.18 (dry milled alloy sample) and Fig. 4.21 (wet milled alloy sample) revealed presence of little or no Fe. The results of XRD conducted as shown in Fig. 4.22 and 4.23 also indicated presence of little or no Fe content. In support

of this, the possibility of presence of excess Fe is unlikely in the framework of Be alloys according to literatures. However, the atomic % of Fe in the milled $\text{Al}_{20}\text{Be}_{20}\text{Fe}_{10}\text{Si}_{15}\text{Ti}_{35}$ alloy is '10' which shows that $\text{Fe}_2\text{Be}_{17}$ might have formed. Hence, $\text{Fe}_2\text{Be}_{17}$ does not spontaneously decompose into FeBe_2 in dilute Fe-Be alloys because $\text{Fe}_2\text{Be}_{17}$ lies on the convex hull.

4.6 Sintering of $\text{Al}_{20}\text{Be}_{20}\text{Fe}_{10}\text{Si}_{15}\text{Ti}_{35}$ Alloy powder

4.6.1 Sintering of Wet-milled $\text{Al}_{20}\text{Be}_{20}\text{Fe}_{10}\text{Si}_{15}\text{Ti}_{35}$ Alloy powder

The cold compaction method was also employed in compacting the alloy powder to be subjected to sintering at a lower temperature afterward. All these attempts proved abortive. The figures below were the images taken after the sintering took place.

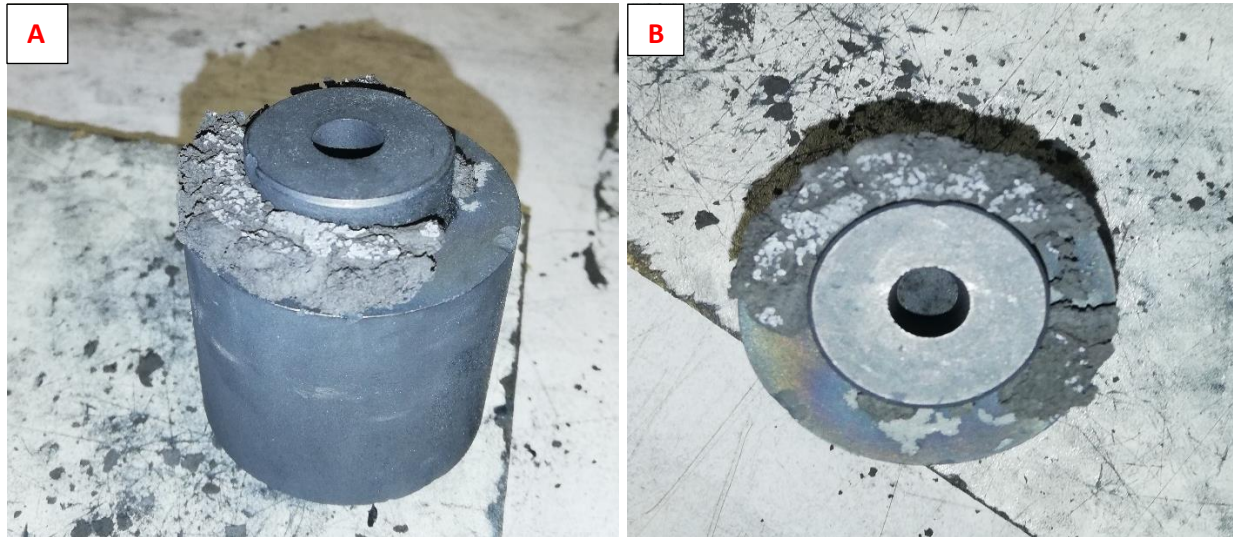


Fig. 4.25 (A) and (B) is the wet-milled alloy powder sublimating out of the punch and die during the sintering process

More reasons why wet-milled alloy powder mix sublimated out of the die completely as shown in Fig. 4.25 above could be presence of ethanol being volatile liquid in addition to volatility properties of Fe present in the alloy mix. According to literatures, BeO could be said to have manifested in appearance in form of whitish foam on the sublimated powder as shown in Fig. 4.25 above. However, BeO is influenced by the temperature at which

the oxide are fired (Makarenko, 2017). Hence, exact control of Be stoichiometry is difficult as it tends to evaporate.

4.6.2 Sintering of Dry-milled $\text{Al}_{20}\text{Be}_{20}\text{Fe}_{10}\text{Si}_{15}\text{Ti}_{35}$ Alloy powder

The figure below shows the image of compacted alloy powder and the sublimated powder that escaped out of the punch and die during the sintering of dry-milled alloy.

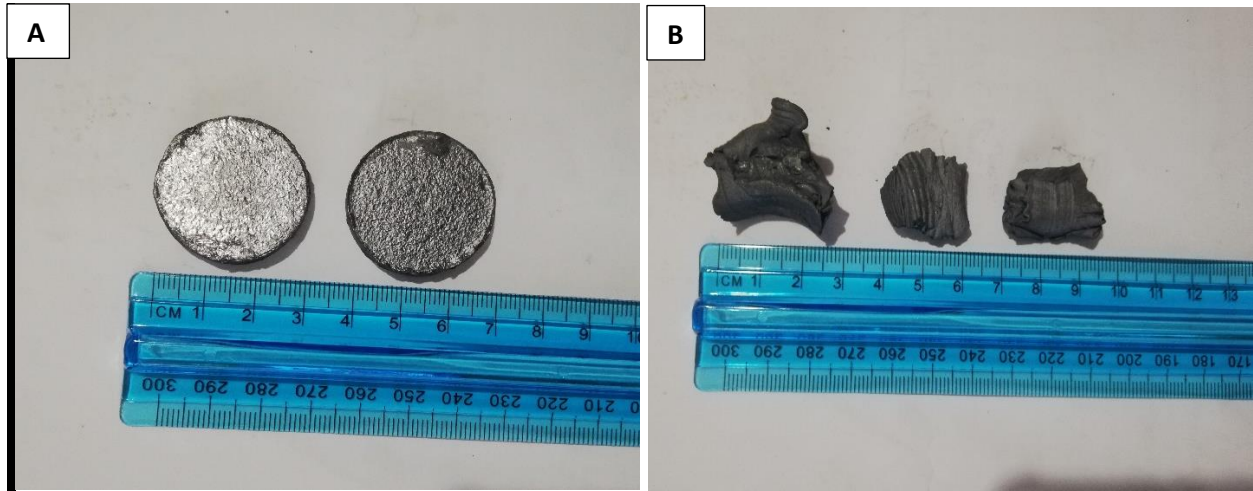


Fig. 4.26 (A) Compacted dry-milled $\text{Al}_{20}\text{Be}_{20}\text{Fe}_{10}\text{Si}_{15}\text{Ti}_{35}$ alloy powder heated up to $\sim 200^\circ\text{C}$, (B) escaped alloy powder from the punch and die during compaction.

The wet-milled alloy powder sublimated out of the punch and die at $\sim 200^\circ\text{C}$ as shown in Fig. 4.25 A and B above, possibly due to low melting point of the alloy mixture. Dry-milled alloy powder was able to be compacted upto $\sim 200^\circ\text{C}$ and could not go any further. The compaction was able to take place in dry milled alloy powder due to absence of ethanol being a volatile liquid. Hence, this reduces the volatility properties of the dry milled alloy mix as compared to the wet milled alloy having ethanol solution. The compacted dry milled alloy powder mix is shown in Fig. 4.26 A above. While Fig. 4.26 B shows the solid sample that sublimated out of the punch and die. In order to understand the possible cause, there is need to ascertain which of the Fe-Be intermetallic phase was formed in the $\text{Al}_{20}\text{Be}_{20}\text{Fe}_{10}\text{Si}_{15}\text{Ti}_{35}$ alloy between $\text{Fe}_2\text{Be}_{17}$ and $\text{Fe}_2\text{Be}_{17}$. Hence, this is crucial in order to examine and establish the effect of the formed Fe-Be intermetallic phases on premature

sublimation of the alloy mixture. To understand this, there is need to know the effect of temperature-dependent thermodynamic properties within the harmonic approximation and including configuration entropy. It is necessary to calculate Helmholtz's free energy of formation following reactions (1) – (5) above and present the results for the temperature range of 0 – 1600 K.

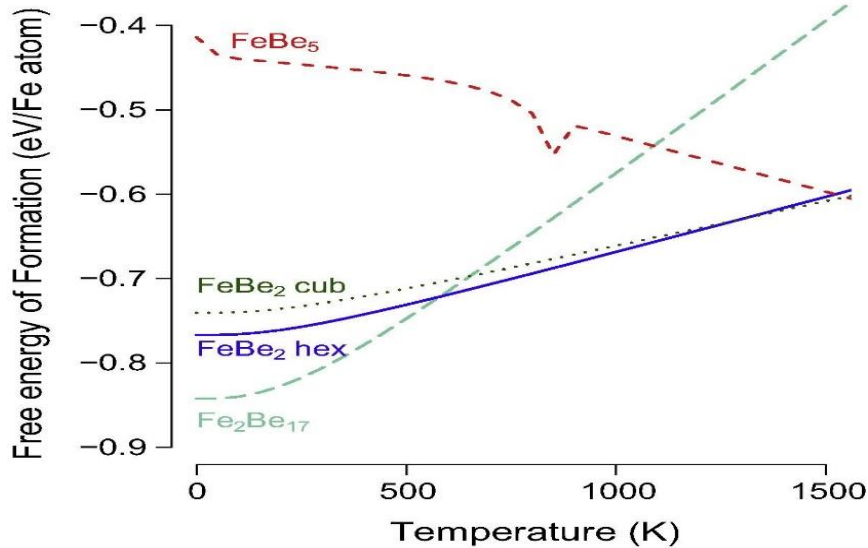


Fig. 4.27 Free energy formation vs temperature for Fe-Be binary intermetallic (Values are normalized per Fe atom.)

It can be deduced from the graph above that with increasing temperature, the stability of Fe₂Be₁₇ phase decreases. At ~1200 K (926.85°C), it can be seen that FeBe₅ curve crosses the Fe₂Be₁₇ curve, hence, 926.85°C may be considered as the lower bound or minimum temperature at which FeBe₅ is formed in Be-rich compounds such as Al₂₀Be₂₀Fe₁₀Si₁₅Ti₃₅. However, 926.85°C temperature was not reached during sintering of both wet and dry-milled Al₂₀Be₂₀Fe₁₀Si₁₅Ti₃₅ alloy before sublimation of the alloy mix took place. Since the sublimation of the powder occurred ~ 200°C, FeBe₅ did not survive any of the used sintering temperatures (500°C, 937.41°C, and 1071.328°C). Therefore, this decomposition condition is associated with low melting phase of the alloy mix due to formation of Fe₂Be₁₇ phase. Since all attempts in conducting the sintering process on both dry and wet-milled Al₂₀Be₂₀Fe₁₀Si₁₅Ti₃₅ alloy failed, therefore, there was a need to

conduct a thermo-analytical examination on both milled alloy powder using thermogravimetric analysis and differential scanning calorimetric (TGA/DSC) equipment. This is necessary in order to ascertain the main cause of premature sublimation of the milled alloy powder using TGA/DSC analysis.

4.7 Thermogravimetric Analysis and Differential Scanning Calorimetric (TGA/DSC) of $\text{Al}_{20}\text{Be}_{20}\text{Fe}_{10}\text{Si}_{15}\text{Ti}_{35}$ Alloy Powder

TGA/DSC analysis was conducted on dry and wet-milled $\text{Al}_{20}\text{Be}_{20}\text{Fe}_{10}\text{Si}_{15}\text{Ti}_{35}$ alloy powder to understand the chemistry behind premature sublimation of the alloy powders around the temperature of $\sim 200^\circ\text{C}$. Hence, this helped to predict what was responsible for sintering failure.

The graphs below show the behavior of dry-milled alloy powder when subjected to TGA/DSC analysis.

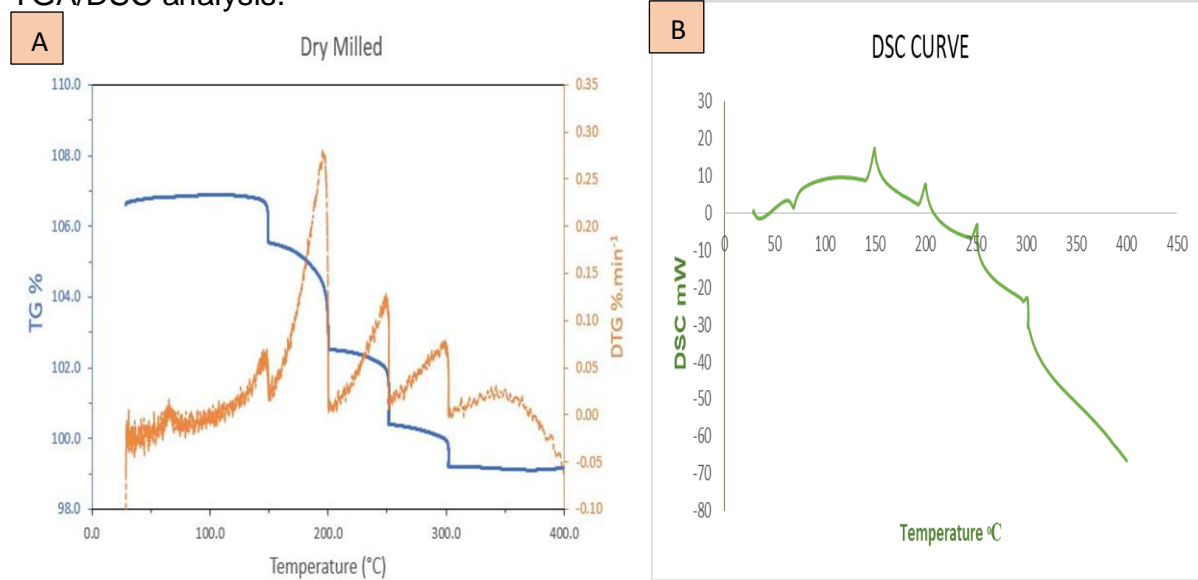


Fig. 4.28 Dry-milled alloy (A) TG curve and (B) DSC curve

According to the TGA/DSC graph in figure 4.28 above, the dry milled alloy powder started to decompose and increase in size at a slow rate with increase in temperature from room temperature. Dry-milled $\text{Al}_{20}\text{Be}_{20}\text{Fe}_{10}\text{Si}_{15}\text{Ti}_{35}$ alloy could be said to have gained by 6% (w/w). But at exactly 150°C , a sudden rate of decomposition took place from 150°C to

200°C which triggers rapid expansion of the alloy powder. Hence, this led to continuous decrease in mass of the alloy powder from the temperature of 150°C. Here at this temperature, the alloy powder started to sublime out of the punch and die during sintering process. The sintering machine tripped off around 200°C and could not proceed any further, so the proposed temperature of 500°C could not be reached. This is where sublimated solid alloy powder from the punch and die during compaction was formed as shown in figure 4.26 B above. The $\text{Al}_{20}\text{Be}_{20}\text{Fe}_{10}\text{Si}_{15}\text{Ti}_{35}$ dry milled alloy powder is found to be a little thermally stable from room temperature to 150°C and became thermally unstable from then upward. So, the compaction of the alloy powder up to ~ 200°C as shown in figure 4.26 A was as a result of the powders considerable thermal stability up to ~ 200°C according to the TGA results. Therefore, it can be said that there is presence of Be–Fe particles that acted as the nuclei of $\alpha\text{-Al}$ in $\text{Al}_{20}\text{Be}_{20}\text{Fe}_{10}\text{Si}_{15}\text{Ti}_{35}$ alloy. This caused the formation of $\text{Fe}_2\text{Be}_{17}$ intermetallic phase in the dry milled alloy at around 150°C according to the XRD conducted. This resulted in low melting phase in the alloy which is responsible for the sublimation of the alloy powder.

The graphs below show the behavior of wet-milled alloy powder when subjected to TGA/DSC analysis.

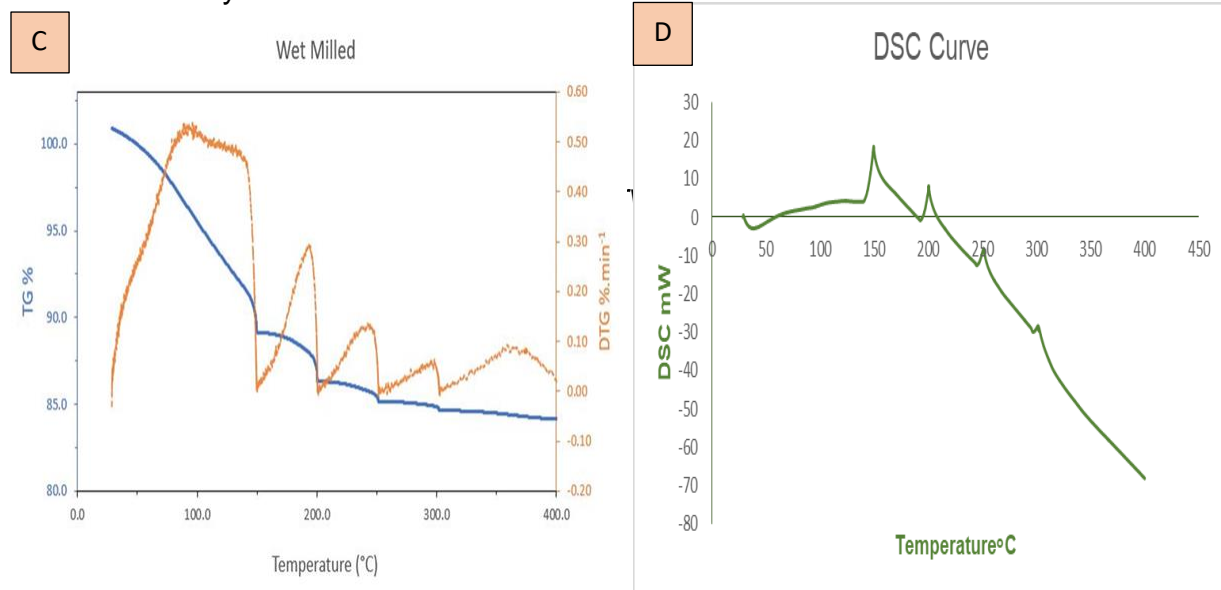


Fig. 4.29 Wet-milled alloy (A) TG curve and (B) DSC curve

According to the TGA/DSC graph in figure 4.29 above, the wet milled alloy powder started to decompose and increase in size and thereby caused expansion in the alloy powder at a very rapid rate from room temperature to $\sim 100^{\circ}\text{C}$. About 25% of 10.660mg initial mass weight gain could be seen on the wet-milled $\text{Al}_{20}\text{Be}_{20}\text{Fe}_{10}\text{Si}_{15}\text{Ti}_{35}$ alloy. The presence of ethanol being a volatile liquid and Fe in the alloy powder mix must have aided the quick volatility properties of the alloy powder. At this point, continuous and rapid weight and mass loss in the alloy powder is noticed starting as the temperature increases. There is a sudden decomposition that took place at temperature of 150°C which triggers decrease in weight of wet milled alloy powder. Then the alloy powder continues to decompose and loose mass and weight at irregular rate as temperature increases. The sintering machine tripped off around 150°C and could not proceed any further, so the proposed temperatures of 500°C , $937,41^{\circ}\text{C}$, 1071.328°C could not be reached. Hence, sublimation of wet milled alloy powder must have started to take place from room temperature as the temperature increases. The leftovers of wet milled alloy must have sublimated out of the punch and die at temperature of 150°C and thereby left the die empty as shown in figure 4.25 A and B above. Therefore, it can be said that there is presence of Be–Fe particles that acted as the nuclei of $\alpha\text{-Al}$ in $\text{Al}_{20}\text{Be}_{20}\text{Fe}_{10}\text{Si}_{15}\text{Ti}_{35}$ alloy. This caused the formation of $\text{Fe}_2\text{Be}_{17}$ intermetallic phase in the wet milled alloy at around 150°C according to the XRD conducted. This resulted in low melting phase in the alloy which is responsible for the total sublimation of the alloy powder. Hence, the $\text{Al}_{20}\text{Be}_{20}\text{Fe}_{10}\text{Si}_{15}\text{Ti}_{35}$ wet milled alloy powder is thermally unstable even from room temperature.

5.0 CONCLUSION AND RECOMMENDATIONS

5.1 CONCLUSION

Continuous efforts by researchers to replace high-density metals and alloys such as steel with aluminum, silicon, titanium, and composite-based materials without compromising on structural properties remains a top priority. This led to the synthesis of lightweight high-entropy alloy initiatives via a conventional method such as melting and casting so far. Research shows that it is almost impossible to achieve the required properties in LWHEA alloys through the traditional design methods such as the addition of refractory elements or casting. The powder metallurgy processing route is chosen to fabricate $\text{Al}_{20}\text{Be}_{20}\text{Fe}_{10}\text{Si}_{15}\text{Ti}_{35}$ alloy because of the possibility of achieving better quality and homogeneous samples according to the literature. Previous research on synthesizing this alloy using MA and SPS is so limited. Hence a full study on the challenges associated with synthesizing $\text{Al}_{20}\text{Be}_{20}\text{Fe}_{10}\text{Si}_{15}\text{Ti}_{35}$ LWHEAs alloy using MA and SPS has been properly harnessed for better understanding and analysis.

Al, Be, Fe, Si, and Ti starting particle size was determined and later characterized using XRD and SEM. The individual element was weighed according to their weight percent and milled under argon controlled environment in wet and dry condition. The dry-milled $\text{Al}_{20}\text{Be}_{20}\text{Fe}_{10}\text{Si}_{15}\text{Ti}_{35}$ alloy sample revealed irregular shape of microns. EDS mapping reveals the high content of C and O which may be due to contamination and Be, Fe, as well as Si, was nowhere to be found in the result. Be might be too light to be picked up by EDS result. All attempts to subject both wet and dry milled powder to the sintering process failed as the powder kept sublimating out of the die at a temperature around 150°C . The sublimated alloy powder seems volatile after being subjected to the sintering process possibly due to presence of volatile materials such as ethanol and Fe in addition to evaporation tendency of Be powder.

It can be concluded that the presence of Fe and Al which are mostly regarded as impurities in Be alloys were suspected to have formed an unstable phase in the alloy under consideration. Perhaps forms Be-rich intermetallic. Hence, if the impurity elements

are not retained in solution within the Be phase, they tend to form second phase particles embedded within the grains or form at grain boundaries and surfaces. Although, literature shows that influence of Al and Fe on the performance of Be will depend upon which phases are manifest. There is conflicting experimental data across literatures. However, their presence has been seen to have a negative effect on the chemical properties of the $\text{Al}_{20}\text{Be}_{20}\text{Fe}_{10}\text{Si}_{15}\text{Ti}_{35}$ milled alloy powder. Although the possibility of the effect of O contamination cannot be ruled out during the experiment as its' almost unavoidable. Hence, sublimation of the milled powders out of the die during sintering cannot be totally attributed to contamination of the alloy powder. It can also be attributed to $\text{Fe}_2\text{Be}_{17}$ phase formed which becomes unstable with an increase in temperature. Also, a decomposition leading to thermal expansion in both dry and wet milled alloy powder at a rapid rate from room temperature to $\sim 150^\circ\text{C}$. Hence, both dry and wet milled $\text{Al}_{20}\text{Be}_{20}\text{Fe}_{10}\text{Si}_{15}\text{Ti}_{35}$ milled powder were thermally unstable. These are possible cause of premature sublimation that occurred in the $\text{Al}_{20}\text{Be}_{20}\text{Fe}_{10}\text{Si}_{15}\text{Ti}_{35}$ milled powder during the sintering process. It can be said that all the proposed objectives in this study were met.

5.2 RECOMMENDATIONS

It is well established that Be rich intermetallic is formed in the presence of Fe and Al, there is still conflicting experimental data across scientific journals towards the understanding of the effect of possible phases formed. There is still a gap in knowledge towards identifying the likely extent of deviations from stoichiometric compositions, stoichiometry, and structure of the commonly observed intermetallic ϵ phase are not well established. Therefore, information gathered here provides the foundation for a combined technique involving thermodynamically experiment and modeling of the effect of possible phases formed on Be-rich alloy in the presence of Al and Fe. These will give more vivid insight into the chemistry behind the reason why both wet and dry-milled $\text{Al}_{20}\text{Be}_{20}\text{Fe}_{10}\text{Si}_{15}\text{Ti}_{35}$ fail to sinter even from low temperatures. Hence, provide researchers with better ways to maneuver synthesizing $\text{Al}_{20}\text{Be}_{20}\text{Fe}_{10}\text{Si}_{15}\text{Ti}_{35}$ and other LWHEAs via powder metallurgy route successfully.

6.0 LIMITATION

Previous research on synthesizing $\text{Al}_{20}\text{Be}_{20}\text{Fe}_{10}\text{Si}_{15}\text{Ti}_{35}$ LWHEAs using MA and SPS is so limited hence, there are limited information regarding the alloy synthesis.

Reference

- AKASH, M. S. H. & REHMAN, K. 2020. Differential scanning calorimetry. *Essentials of Pharmaceutical Analysis*. Springer.
- ALVES, N., MANO, J. F., BALAGUER, E., DUEÑAS, J. M. & RIBELLES, J. G. 2002. Glass transition and structural relaxation in semi-crystalline poly (ethylene terephthalate): a DSC study. *Polymer*, 43, 4111-4122.
- BOUSAHLA, A. A., BENYOUCEF, S., TOUNSI, A. & MAHMOUD, S. 2016. On thermal stability of plates with functionally graded coefficient of thermal expansion. *Structural engineering and mechanics: An international journal*, 60, 313-335.
- BROWN, M. E. 2001. *Introduction to thermal analysis: techniques and applications*, Springer Science & Business Media.
- BURR, P. A., MIDDLEBURGH, S. C. & GRIMES, R. W. 2016. Solubility and partitioning of impurities in Be alloys. *Journal of Alloys and Compounds*, 688, 382-385.
- CHAKRABORTY, S., DAS, P. K. & GHOSH, D. 2016. SPARK PLASMA SINTERING AND STRUCTURAL PROPERTIES OF ZrB₂ BASED CERAMICS: A REVIEW. *Reviews on Advanced Materials Science*, 44, 182-193.
- CHAWAKE, N., KOUNDINYA, N. T. B. N., KASHYAP, S., SRIVASTAV, A. K., YADAV, D., MONDAL, R. A. & KOTTADA, R. S. 2016. Formation of amorphous alumina during sintering of nanocrystalline B₂ aluminides. *Materials Characterization*, 119, 186-194.
- CHEN, W., FU, Z., FANG, S., XIAO, H. & ZHU, D. 2013. Alloying behavior, microstructure and mechanical properties in a FeNiCrCo_{0.3}Al_{0.7} high entropy alloy. *Materials & Design*, 51, 854-860.
- DĄBROWA, J., KUCZA, W., CIEŚLAK, G., KULIK, T., DANIELEWSKI, M. & YEH, J.-W. 2016. Interdiffusion in the FCC-structured Al-Co-Cr-Fe-Ni high entropy alloys: experimental studies and numerical simulations. *Journal of Alloys and Compounds*, 674, 455-462.
- DIN, S. U., HUGHES, H., O'REILLY, N. J., CATHCART, H., O'CEALLAIGH, T., NDZIE, E. & MCLOUGHLIN, P. 2020. Investigation into the stability, crystallization kinetics, and heating rate dependent crystallization of amorphous posaconazole. *Crystal Growth & Design*, 20, 5129-5142.
- DOŁĘGA, A., JUSZYŃSKA-GAŁĄZKA, E., OSIECKA-DREWNIAK, N., NATKAŃSKI, P., KUŚTROWSKI, P., KRUPA, A. & ZIELIŃSKI, P. M. 2021. Study on the thermal performance of carbamazepine at different temperatures, pressures and atmosphere conditions. *Thermochimica Acta*, 703, 178990.
- FEIST, M. 2015. Thermal analysis: basics, applications, and benefit. *ChemTexts*, 1, 8.
- FERNANDES, F., MANARI, S., AGUAYO, M., SANTOS, K., OEY, T., WEI, Z., FALZONE, G., NEITHALATH, N. & SANT, G. 2014. On the feasibility of using phase change

- materials (PCMs) to mitigate thermal cracking in cementitious materials. *Cement and Concrete Composites*, 51, 14-26.
- FERRER, G., BARRENECHE, C., SOLÉ, A., MARTORELL, I. & CABEZA, L. F. 2017. New proposed methodology for specific heat capacity determination of materials for thermal energy storage (TES) by DSC. *Journal of Energy Storage*, 11, 1-6.
- FU, Z., CHEN, W., XIAO, H., ZHOU, L., ZHU, D. & YANG, S. 2013. Fabrication and properties of nanocrystalline Co_{0.5}FeNiCrTi_{0.5} high entropy alloy by MA–SPS technique. *Materials & Design*, 44, 535-539.
- GAISFORD, S., KETT, V. & HAINES, P. 2019. *Principles of thermal analysis and calorimetry*, Royal society of chemistry.
- GLUDOVATZ, B., HOHENWARTER, A., CATOOR, D., H. CHANG, E., P. GEORGE, E. & RITCHIE, R. 2014. *A Fracture-Resistant High-Entropy Alloy for Cryogenic Applications*.
- GUPTA, M. 2017. *An Insight into the Development of Light Weight High Entropy Alloys*.
- GWALANI, B., AYYAGARI, A. V., CHOUDHURI, D., SCHARF, T., MUKHERJEE, S., GIBSON, M. & BANERJEE, R. 2018. Microstructure and wear resistance of an intermetallic-based Al_{0.25}Ti_{0.75}CoCrFeNi high entropy alloy. *Materials Chemistry and Physics*, 210, 197-206.
- HAN, Z. D., CHEN, N., ZHAO, S. F., FAN, L. W., YANG, G. N., SHAO, Y. & YAO, K. F. 2017. Effect of Ti additions on mechanical properties of NbMoTaW and VNbMoTaW refractory high entropy alloys. *Intermetallics*, 84, 153-157.
- HÖTZER, J., SEIZ, M., KELLNER, M., RHEINHEIMER, W. & NESTLER, B. 2019. Phase-field simulation of solid state sintering. *Acta Materialia*, 164, 184-195.
- HOUSKA, C. 1988. Beryllium in aluminium and magnesium alloys. *Metals and Materials*, 4, 100-104.
- JI, W., WANG, W., WANG, H., ZHANG, J., WANG, Y., ZHANG, F. & FU, Z. 2015. Alloying behavior and novel properties of CoCrFeNiMn high-entropy alloy fabricated by mechanical alloying and spark plasma sintering. *Intermetallics*, 56, 24-27.
- JOSEPH, J., HODGSON, P., JARVIS, T., WU, X., STANFORD, N. & FABIJANIC, D. M. 2018. Effect of hot isostatic pressing on the microstructure and mechanical properties of additive manufactured Al_xCoCrFeNi high entropy alloys. *Materials Science and Engineering: A*, 733, 59-70.
- KADYRZHANOV, K., VERESHCHAK, M., MANAKOVA, I., OZERNOY, A. & RUSAKOV, V. 2013. Structure-phase transformations in the Be–Fe–Be layered system subjected to irradiation and thermal treatment. *Journal of Physics and Chemistry of Solids*, 74, 1078-1085.
- KANG, B., LEE, J., RYU, H. J. & HONG, S. H. 2018. Microstructure, mechanical property and Hall-Petch relationship of a light-weight refractory Al_{0.1}CrNbVMo high entropy

- alloy fabricated by powder metallurgical process. *Journal of Alloys and Compounds*, 767, 1012-1021.
- KAO, Y.-F., CHEN, T.-J., LEE, P.-H. & YEH, J.-W. 2009. *Microstructure and mechanical property of as-cast, homogenized, and -deformed Al x CoCrFeNi (0 ≤ x ≤ 2) high-entropy alloys*.
- KNOPP, M. M., LÖBMANN, K., ELDER, D. P., RADES, T. & HOLM, R. 2016. Recent advances and potential applications of modulated differential scanning calorimetry (mDSC) in drug development. *European Journal of Pharmaceutical Sciences*, 87, 164-173.
- KUCZA, W., DAŁBROWA, J., CIEŚLAK, G., BERENT, K., KULIK, T. & DANIELEWSKI, M. 2018. Studies of “sluggish diffusion” effect in Co-Cr-Fe-Mn-Ni, Co-Cr-Fe-Ni and Co-Fe-Mn-Ni high entropy alloys; determination of tracer diffusivities by combinatorial approach. *Journal of Alloys and Compounds*, 731, 920-928.
- KULKARNI, K. & CHAUHAN, G. P. S. 2015. Investigations of quaternary interdiffusion in a constituent system of high entropy alloys. *AIP Advances*, 5, 097162-097162.7.
- KUMAR, A. & GUPTA, M. 2016. An Insight into Evolution of Light Weight High Entropy Alloys: A Review. *Metals*, 6.
- L. COBLE, R. 1961. *Sintering crystalline solids: I. Intermediate and final stage models; II. Experimental test of diffusion models in powder compacts*.
- LAYE, P. 2002. Differential thermal analysis and differential scanning calorimetry. *Principles of thermal analysis and calorimetry*, 52.
- LEE, H. 2020. *The Role of Grain Boundaries in the Tensile Deformation Behavior of CoCrFeMnNi High Entropy Alloys*. Clemson University.
- LI, C., LI, J. C., ZHAO, M. & JIANG, Q. 2009. Effect of alloying elements on microstructure and properties of multiprincipal elements high-entropy alloys. *Journal of Alloys and Compounds*, 475, 752-757.
- LI, X., DU, D., GAGNOUD, A., REN, Z., FAUTRELLE, Y. & MOREAU, R. 2014. Effect of Multi-Scale Thermoelectric Magnetic Convection on Solidification Microstructure in Directionally Solidified Al-Si Alloys Under a Transverse Magnetic Field. *Metallurgical and Materials Transactions A*, 45.
- LI, X. X., YANG, C., CHEN, T., ZHANG, L. C., HAYAT, M. D. & CAO, P. 2019a. Influence of powder shape on atomic diffusivity and resultant densification mechanisms during spark plasma sintering. *Journal of Alloys and Compounds*.
- LI, Z., ZHAO, S., RITCHIE, R. O. & MEYERS, M. A. 2019b. Mechanical properties of high-entropy alloys with emphasis on face-centered cubic alloys. *Progress in Materials Science*, 102, 296-345.
- MACDONALD, B. E., FU, Z., ZHENG, B., CHEN, W., LIN, Y., CHEN, F., ZHANG, L., IVANISENKO, J., ZHOU, Y., HAHN, H. & LAVERNIA, E. J. 2017. Recent Progress in High Entropy Alloy Research. *JOM*, 69, 2024-2031.

- MAKARENKO, D. 2017. Investigation of the response surfaces describing the mathematical model of the influence of temperature and BeO content in the composite materials on the yield and ultimate strength. *Технологический аудит и резервы производства*, 3, 13-17.
- MATIZAMHUKA, W. 2016. Spark plasma sintering (SPS)-an advanced sintering technique for structural nanocomposite materials. *Journal of the Southern African Institute of Mining and Metallurgy*, 116, 1171-1180.
- MIRACLE, D. B. 2017. High-Entropy Alloys: A Current Evaluation of Founding Ideas and Core Effects and Exploring “Nonlinear Alloys”. *JOM*, 69, 2130-2136.
- MIRACLE, D. B. & SENKOV, O. N. 2017. A critical review of high entropy alloys and related concepts. *Acta Materialia*, 122, 448-511.
- MORAVCIK, I., CIZEK, J., GAVENDOVA, P., SHEIKH, S., GUO, S. & DLOUHY, I. 2016. Effect of heat treatment on microstructure and mechanical properties of spark plasma sintered AlCoCrFeNiTi_{0.5} high entropy alloy. *Materials Letters*, 174, 53-56.
- MORAVCIK, I., CIZEK, J., ZAPLETAL, J., KOVACOVA, Z., VESELY, J., MINARIK, P., KITZMANTEL, M., NEUBAUER, E. & DLOUHY, I. 2017. Microstructure and mechanical properties of Ni_{1.5}Co_{1.5}CrFeTi_{0.5} high entropy alloy fabricated by mechanical alloying and spark plasma sintering. *Materials & Design*, 119, 141-150.
- MÜLLER, A. J. & MICHELL, R. M. 2016. Differential scanning calorimetry of polymers. *Polymer Morphology: Principles, Characterization, and Processing*. John Wiley and Sons New Jersey.
- MÜLLER, C. 2015. On the glass transition of polymer semiconductors and its impact on polymer solar cell stability. *Chemistry of Materials*, 27, 2740-2754.
- MURTY, B. S., YEH, J. W., RANGANATHAN, S. & BHATTACHARJEE, P. P. 2019. 1 - A brief history of alloys and the birth of high-entropy alloys. In: MURTY, B. S., YEH, J. W., RANGANATHAN, S. & BHATTACHARJEE, P. P. (eds.) *High-Entropy Alloys (Second Edition)*. Elsevier.
- OBADELE, B. A., IGE, O. O. & OLUBAMBI, P. A. 2017. Fabrication and characterization of titanium-nickel-zirconia matrix composites prepared by spark plasma sintering. *Journal of Alloys and Compounds*, 710, 825-830.
- ONAWALE, O. T., COBBINAH, P. V., NZEUKOU, R. A. & MATIZAMHUKA, W. R. 2021. Synthesis Route, Microstructural Evolution, and Mechanical Property Relationship of High-Entropy Alloys (HEAs): A Review. *Materials*, 14, 3065.
- OTTO, F., DLOUHÝ, A., SOMSEN, C., BEI, H., EGGELER, G. & GEORGE, E. P. 2013. The influences of temperature and microstructure on the tensile properties of a CoCrFeMnNi high-entropy alloy. *Acta Materialia*, 61, 5743-5755.

- OWEN, L. R., PICKERING, E. J., PLAYFORD, H. Y., STONE, H. J., TUCKER, M. G. & JONES, N. G. 2017. An assessment of the lattice strain in the CrMnFeCoNi high-entropy alloy. *Acta Materialia*, 122, 11-18.
- PEREIRA DA SILVA, J. G., BRAM, M., LAPTEV, A. M., GONZALEZ-JULIAN, J., MA, Q., TIETZ, F. & GUILLON, O. 2019. Sintering of a sodium-based NASICON electrolyte: A comparative study between cold, field assisted and conventional sintering methods. *Journal of the European Ceramic Society*, 39, 2697-2702.
- POLINI, A. & YANG, F. 2017. Physicochemical characterization of nanofiber composites. *Nanofiber composites for biomedical applications*. Elsevier.
- QIU, Y., HU, Y. J., TAYLOR, A., STYLES, M. J., MARCEAU, R. K. W., CEGUERRA, A. V., GIBSON, M. A., LIU, Z. K., FRASER, H. L. & BIRBILIS, N. 2017. A lightweight single-phase AlTiVCr compositionally complex alloy. *Acta Materialia*, 123, 115-124.
- RIQUET, G., MARINEL, S., BRÉARD, Y. & HARNOIS, C. 2019. Sintering mechanism and grain growth in CaCu₃Ti₄O₁₂ ceramics. *Ceramics International*, 45, 9185-9191.
- ROOKSBY, H. 1962. Intermetallic phases in commercial beryllium. *Journal of Nuclear Materials*, 7, 205-211.
- S. BENJAMIN, J. & E. VOLIN, T. 1974. *The Mechanism of Mechanical Alloying*.
- SAHEB, N., IQBAL, Z., KHALIL, A., HAKEEM, A. S., AL AQEELI, N., LAOUI, T., AL-QUTUB, A. & KIRCHNER, R. 2012. Spark plasma sintering of metals and metal matrix nanocomposites: a review. *Journal of Nanomaterials*, 2012, 18.
- SANCHEZ, J. M., VICARIO, I., ALBIZURI, J., GURAYA, T. & GARCIA, J. C. 2019. Phase prediction, microstructure and high hardness of novel light-weight high entropy alloys. *Journal of Materials Research and Technology*, 8, 795-803.
- SANTOS, A. C. & RIBEIRO, S. 2018. Liquid phase sintering and characterization of SiC ceramics. *Ceramics International*, 44, 11048-11059.
- SARGE, S., HEMMINGER, W., GMELIN, E., HÖHNE, G., CAMMENGA, H. & EYSEL, W. 1997. Metrologically based procedures for the temperature, heat and heat flow rate calibration of DSC. *Journal of Thermal Analysis and Calorimetry*, 49, 1125-1134.
- SENKOV, N. O., ISHEIM, D., SEIDMAN, N. D. & PILCHAK, L. A. 2016. Development of a Refractory High Entropy Superalloy. *Entropy*, 18.
- SHEWMON, P. 2016. *Diffusion in solids*, Springer.
- SHONGWE, M. B., RAMAKOKOVHU, M. M., LETHABANE, M. L. & OLUBAMBI, P. A. Comparison of spark plasma sintering and hybrid spark plasma sintering of Ni-Fe alloys. Proceedings of the World Congress on Engineering, 2017.
- SINGH, S., WANDERKA, N., MURTY, B. S., GLATZEL, U. & BANHART, J. 2011. Decomposition in multi-component AlCoCrCuFeNi high-entropy alloy. *Acta Materialia*, 59, 182-190.

- SULLIVAN, K. T., PIEKIEL, N. W., WU, C., CHOWDHURY, S., KELLY, S. T., HUFNAGEL, T. C., FEZZAA, K. & ZACHARIAH, M. R. 2012. Reactive sintering: An important component in the combustion of nanocomposite thermites. *Combustion and Flame*, 159, 2-15.
- SUN, X., LEE, K. O., MEDINA, M. A., CHU, Y. & LI, C. 2018. Melting temperature and enthalpy variations of phase change materials (PCMs): a differential scanning calorimetry (DSC) analysis. *Phase Transitions*, 91, 667-680.
- SURYANARAYANA, C. 2001. Mechanical alloying and milling. *Progress in Materials Science*, 46, 1-184.
- TANG, Z., YUAN, T., TSAI, C.-W., YEH, J.-W., LUNDIN, C. D. & LIAW, P. K. 2015. Fatigue behavior of a wrought Al_{0.5}CoCrCuFeNi two-phase high-entropy alloy. *Acta Materialia*, 99, 247-258.
- TIAN, F., VARGA, L. K., CHEN, N., SHEN, J. & VITOS, L. 2015. Empirical design of single phase high-entropy alloys with high hardness. *Intermetallics*, 58, 1-6.
- TIAN, Q., ZHANG, G., YIN, K., WANG, W., CHENG, W. & WANG, Y. 2019. The strengthening effects of relatively lightweight AlCoCrFeNi high entropy alloy. *Materials Characterization*, 151, 302-309.
- TODA-CARABALLO, I. & RIVERA-DÍAZ-DEL-CASTILLO, P. E. J. 2016. A criterion for the formation of high entropy alloys based on lattice distortion. *Intermetallics*, 71, 76-87.
- TODA, A. 2016. Heating rate dependence of melting peak temperature examined by DSC of heat flux type. *Journal of Thermal Analysis and Calorimetry*, 123, 1795-1808.
- TONG, C.-J., CHEN, M.-R., YEH, J.-W., LIN, S.-J., CHEN, S.-K., SHUN, T.-T. & CHANG, S.-Y. 2005a. Mechanical performance of the Al_xCoCrCuFeNi high-entropy alloy system with multiprincipal elements. *Metallurgical and Materials Transactions A*, 36, 1263-1271.
- TONG, C.-J., CHEN, M.-R., YEH, J.-W., LIN, S.-J., LEE, P.-H., SHUN, T.-T. & CHANG, S.-Y. 2005b. *Mechanical performance of the Al_xCoCrCuFeNi high-entropy alloy system with multiprincipal elements.*
- TORRALBA, J. M., ALVAREDO, P. & GARCÍA-JUNCEDA, A. 2019. High-entropy alloys fabricated via powder metallurgy. A critical review. *Powder Metallurgy*, 62, 84-114.
- TSAI, K. Y., TSAI, M. H. & YEH, J. W. 2013. Sluggish diffusion in Co–Cr–Fe–Mn–Ni high-entropy alloys. *Acta Materialia*, 61, 4887-4897.
- TSENG, K., YANG, Y., JUAN, C., CHIN, T., TSAI, C. & YEH, J. 2018. A light-weight high-entropy alloy Al₂₀Be₂₀Fe₁₀Si₁₅Ti₃₅. *Science China Technological Sciences*, 61, 184-188.
- USKOKOVIĆ, V., MARKOVIĆ, S., VESELINOVIĆ, L., ŠKAPIN, S., IGNJATOVIĆ, N. & USKOKOVIĆ, D. P. 2018. Insights into the kinetics of thermally induced

- crystallization of amorphous calcium phosphate. *Physical Chemistry Chemical Physics*, 20, 29221-29235.
- W CHEAH, L. 2010. *Cars on a Diet: The Material and Energy Impacts of Passenger Vehicle Weight Reduction in the US*.
- WANG, Y. & XIONG, Y. 2000. Effects of beryllium in Al–Si–Mg–Ti cast alloy. *Materials Science and Engineering: A*, 280, 124-127.
- WIELGOSZ, E. & KARGUL, T. 2015. Differential scanning calorimetry study of peritectic steel grades. *Journal of Thermal Analysis and Calorimetry*, 119, 1547-1553.
- XIAO, Y., KOZAK, R., HACHÉ, M. J., STEURER, W., SPOLENAK, R., WHEELER, J. M. & ZOU, Y. 2020. Micro-compression studies of face-centered cubic and body-centered cubic high-entropy alloys: Size-dependent strength, strain rate sensitivity, and activation volumes. *Materials Science and Engineering: A*, 790, 139429.
- YEH, J.-W. 2006a. Recent progress in high-entropy alloys. *Annales de Chimie. Science des Matériaux (Paris)*, 31, 633-648.
- YEH, J.-W. 2013. Alloy Design Strategies and Future Trends in High-Entropy Alloys. *JOM*, 65.
- YEH, J.-W., CHEN, S. K., J. LIN, S. U., GAN, J.-Y., CHIN, T.-S., SHUN, T., TSAU, C. H. & CHANG, S. Y. 2004a. *Nanostructured High-Entropy Alloys with Multiple Principal Elements: Novel Alloy Design Concepts and Outcomes*.
- YEH, J.-W., CHEN, S. K., J. LIN, S. U., GAN, J.-Y., CHIN, T.-S., SHUN, T. T., TSAU, C. H. & CHANG, S. Y. 2004b. *Nanostructured High-Entropy Alloys with Multiple Principal Elements: Novel Alloy Design Concepts and Outcomes*.
- YEH, J. W. 2006b. Recent progress in high-entropy alloys. *Annales de Chimie Science des Matériaux (Paris)*, 31, 633-648.
- ZHANG, K. & WANG, H. 2012. *Effects of annealing treatment on phase composition and microstructure of CoCrFeNiTiAl_x high-entropy alloys*.
- ZHANG, Y., ZHOU, Y. J., LIN, J. P., CHEN, G. L. & LIAW, P. K. 2008. Solid-Solution Phase Formation Rules for Multi-component Alloys. *Advanced Engineering Materials*, 10, 534-538.
- ZHANG, Y., ZUO, T., CHENG, Y. & LIAW, P. K. 2013. High-entropy Alloys with High Saturation Magnetization, Electrical Resistivity and Malleability. *Scientific Reports*, 3, 1455.
- ZHENG, S., CAI, Z., PU, J., ZENG, C., CHEN, S., CHEN, R. & WANG, L. 2019. A feasible method for the fabrication of VAlTiCrSi amorphous high entropy alloy film with outstanding anti-corrosion property. *Applied Surface Science*, 483, 870-874.
- ZOU, Y., MAITI, S., STEURER, W. & SPOLENAK, R. 2014. Size-dependent plasticity in an Nb₂₅Mo₂₅Ta₂₅W₂₅ refractory high-entropy alloy. *Acta Materialia*, 65, 85-97.